

2015

Zero Gravity Dynamics Of Two-Phase Flow In A Circular Cylinder

H. Hallaby Ghazi

North Carolina Agricultural and Technical State University

Follow this and additional works at: <https://digital.library.ncat.edu/theses>

Recommended Citation

Ghazi, H. Hallaby, "Zero Gravity Dynamics Of Two-Phase Flow In A Circular Cylinder" (2015). *Theses*. 280.
<https://digital.library.ncat.edu/theses/280>

This Thesis is brought to you for free and open access by the Electronic Theses and Dissertations at Aggie Digital Collections and Scholarship. It has been accepted for inclusion in Theses by an authorized administrator of Aggie Digital Collections and Scholarship. For more information, please contact iyanna@ncat.edu.

Zero Gravity Dynamics of Two-Phase Flow In a Circular Cylinder

Ghazi H. Hallaby

North Carolina A&T State University

A thesis submitted to the graduate faculty
in partial fulfillment of the requirements for the degree of

MASTER OF SCIENCE

Department: Mechanical Engineering

Major: Mechanical Engineering

Major Professor: Dr. John P. Kizito

Greensboro, North Carolina

2015

The Graduate School
North Carolina Agricultural and Technical State University

This is to certify that the Master's Thesis of

Ghazi H. Hallaby

has met the thesis requirements of
North Carolina Agricultural and Technical State University

Greensboro, North Carolina
2015

Approved by:

Dr. John P. Kizito
Major Professor

Dr. Cynthia K. Waters
Committee Member

Dr. Mannur Sundaresan
Committee Member

Dr. Samuel P. Owusu-Ofori
Department Chair

Dr. Sanjiv Sarin
Dean, The Graduate School

© Copyright by
Ghazi H. Hallaby
2015

Biographical Sketch

Ghazi H. Hallaby earned his Bachelor of Science degree (Honors) in Aerospace Engineering in 2010 from Kwame Nkrumah University of Science and Technology at Kumasi, Ghana. He graduated at the top 5% of his batch. After graduation, he was offered a position as an assistant engineer in the transport department at Logs and Lumber Limited, a free-zone enterprise in Ghana. In 2012, Hallaby was offered a teaching assistantship position as well as an opportunity to pursue a Master of Science degree in Mechanical Engineering at North Carolina Agricultural and Technical State University. Ghazi H. Hallaby plans to pursue a doctoral degree in aerospace engineering while serving in the U.S Army Reserve.

Dedication

I dedicate my thesis to my family, friends and colleagues. A special feeling of gratitude ,first and foremost, to my mother, Iftikhar (Gifty) Akoum ,whose words of encouragement and push for tenacity ring in my ears. My sister Suzy and father Hilal have never left my side and are very special. I am grateful to my uncles and aunts who have always believed in me.

I also dedicate my work to my friends from all walks of life. My friends in Ghana have been a pillar for me. I also appreciate the support of my colleagues and friends in Greensboro, especially Edmund Gyasi, who has always been there for me throughout this process.

Acknowledgments

First, I cannot express enough thanks to my advisor, committee chair and mentor, Dr. John P. Kizito, for his unrelenting support funding and guiding me for the entirety of this project. I could not have made it without him providing me with this learning opportunity.

My completion of this thesis could not have been accomplished without the support of Dr. Samuel P. Owusu-Ofori. I would like to gratefully and sincerely thank Dr. Owusu-Ofori for his guidance, understanding, most importantly his friendship during my graduate studies at North Carolina Agricultural and Technical State University.

I would also like to thank my committee members, Dr. Mannur Sundaresan and Dr. Cynthia K. Waters, for their input, valuable discussions and accessibility.

Table of Contents

List of Figures	ix
List of Tables	xiii
Nomenclature.....	xiv
Abstract	1
CHAPTER 1 Introduction	2
1.1 Goal and Specific Objectives.....	3
CHAPTER 2 Literature Review	5
2.1 Basic concepts.....	5
2.2 Surface Evolver and OpenFOAM for Studying the Shape and Stability of Capillary Surfaces	13
2.3 Numerical Modelling of Multiphase Flows in CFD with VOF.....	16
CHAPTER 3 Problem Formulation and Methodology.....	20
3.1 Fundamental Questions of Investigation	20
3.1.1 Problem Setup	20
3.2 Basic Equations	21
3.3 OpenFOAM: Introduction	27
3.3.1 OpenFOAM Features.....	28
3.3.2 Components of a Case	29
3.3.3 Steps Outline	30
3.4 Surface Evolver Methodology	39
3.5 Grid Independence Study	41
3.6 Experimental Technique.....	45
3.6.1 Experimental Apparatus and Setup.....	46

CHAPTER 4 Results.....	50
4.1 Experimental Results.....	50
4.2 Numerical Results	59
4.2.1 Comparison of Numerical Results with Experimental Results.....	67
4.2.2 Description of Transition Mechanism	68
4.2.3 Surface Evolver Results.....	82
4.2.4 Comparison of Static and Dynamics Solutions.....	90
CHAPTER 5 Discussion and Future Research.....	95
References	98

List of Figures

Figure 1 Stable and unstable annulus solutions[1]	7
Figure 2 Two possible solutions of plug[1].....	8
Figure 3. Minimum energy solution map in $V - \theta$ space.....	10
Figure 4 Heil's elastic tube used for liquid bridge plug stability studies [11].....	11
Figure 5 Terms of Aspect Ratio.....	11
Figure 6 Possible topologies for lateral compression[10]	12
Figure 7. Minimum energy topology maps for laterally compressed tubes of different aspect ratios[10].....	13
Figure 8. Representation of Artificial Velocity Method approach [7].....	14
Figure 9 Wicking of silicone oil along edges under low gravity.....	15
Figure 10 Interfacial pressure distribution in OpenFOAM and surface Evolver	16
Figure 11 Comparison of analytical, PROST, CLSVOF, and K8 solutions	18
Figure 12. Comparison of VOF and experiment. A. Comparison of bubble volume B. Comparison of bubble diameter. C Comparison of relative bubble velocity. D Comparison of interfacial Area	19
Figure 13 Schematic of Circular Cylinder Model	20
Figure 14 Cross-section of modeled T-section.....	22
Figure 15 Flow chart of PIMPLE algorithm	27
Figure 16 Three- dimensional Computational Domain	31
Figure 17. Energy minimization outcome	40
Figure 18. Graph of the maximum velocity at a cross-section 1mm from the inlet against number of grid nodes.	42

Figure 19. Minimum to maximum pressure ration at cross-section	43
Figure 20 Minimum and maximum pressure at cross-section.....	44
Figure 21 Grid volume size range.....	44
Figure 22. Grid independence (Surface Evolver)	45
Figure 23. Resulting views of the two experiments, (a) Side view, (b) Top view	46
Figure 24. Schematic showing the apparatus and setup of two phase experiment	46
Figure 25. Experimental apparatus and setup.....	47
Figure 26. Schematic drawing of acrylic block showing location and orientation of T-section, and direction of gravitational force	48
Figure 27. Acrylic block with machined T-section (finished product).....	49
Figure 28. Neck of Annulus-Plug Topology	52
Figure 29. Plot of progression of silicone oil interface with time	53
Figure 30. Linear model of injection velocity	54
Figure 31. Plot of progression of silicone oil interface with time	56
Figure 32. Linear model of injection velocity	57
Figure 33. Plot of volume versus time for experiment 1 (side) and experiment 2 (up)	58
Figure 34. Plot of dimensionless volume versus dimensionless time for experiments 1(side) and 2(up).....	58
Figure 35. Plot of time-dependent flow rate and volume for different pressure differences:	69
Figure 36. Comparison of flow rates for different pressure differences	71
Figure 37. Plot of time-dependent flow rate and volume for different pressure differences indicating where plug is formed: A. 0 Pa; B. 30 Pa; C. 60 Pa; D. 90 Pa; and E. 120 Pa.....	72
Figure 38. Comparison of time-dependent volume plot for different applied pressures.	75

Figure 39. Volume versus Time for a pressure difference of 60 Pa for Bond number of 0.47 and 0 (i.e. $Bo = 0$ and $Bo = 0.47$).....	76
Figure 40. Flow rate versus time for a pressure difference of 60 Pa for a Bond number of 0 and 0.47. (i.e. $Bo = 0$ and $Bo = 0.47$)	76
Figure 41. Dimensionless Flow Rate versus Dimensionless Time.....	78
Figure 42. Non-dimensional volume versus non-dimensional time	79
Figure 43. Plot of average system kinetic energy versus time	79
Figure 44. Plot of non-dimensional system kinetic energy versus time	80
Figure 45. Relationship between Plug solution and applied Pressure Difference	81
Figure 46. Plot of plug non-dimensional time versus pressure difference showing the existence of a plug characteristic time.....	82
Figure 47. Annulus solution for a non-dimensional volume of 2.....	83
Figure 48. Annulus solution for a non-dimensional volume of 3.....	84
Figure 49. Annulus solution for a non-dimensional volume of 4.....	85
Figure 50. Minimum annular solution for non-dimensional volume of 4.5.....	86
Figure 51. Minimum annular solution for non-dimensional volume of 4.6.....	87
Figure 52. Minimum plug solution for a non-dimensional volume of 4.7.....	88
Figure 53. Minimum plug solution for a non-dimensional volume of 5.....	89
Figure 54. Comparison of OpenFOAM and Surface Evolver solutions for non-dimensional volume of 4.7. OpenFOAM result is a cross section along the axis of the cylinder. The liquid is designated the color red and air is assigned the color blue. Surface Evolver result is a side view of interfaces of the stable plug solution.	90

Figure 55. Plot of interfacial position using OpenFOAM and Surface Evolver for a non-dimensional volume of 4.7. The plot is non-dimensionalized using the cylinder diameter.....	91
Figure 56. Comparison of stable static and dynamic solutions	92
Figure 57. Comparison of dynamic solutions for annulus and plug showing transition regimes .	93
Figure 58. Comparison of OpenFOAM results with Surface Evolver plug solutions for circular cylinders with varying aspect ratios (AR) (from literature[1, 10]) for 10° contact angle.....	94

List of Tables

Table 1 Model Properties	23
Table 2 Initial conditions	24
Table 3 Summary of Grid Independence Results	41
Table 4 Side views of evolving silicone oil interface	50
Table 5 Top views of evolving silicone oil interface	55
Table 6 Numerical results for 0 Pa at the inlet	60
Table 7 Numerical results for 30 Pa at the inlet	61
Table 8 Numerical results for 60 Pa at the inlet	62
Table 9 Numerical results for 90 Pa at the inle	63
Table 10 Numerical results for 120 Pa at the inlet.....	65
Table 11 Comparison of numerical (0 Pa) and experimental results	67
Table 12 Summary of topological transition points.....	68
Table 13 Summary of Flow rate jump and duration of annulus to plug transition.....	73
Table 14 Maximum inlet velocities for non-dimensionalization.....	77

Nomenclature

σ	=	interfacial tension
ρ_1	=	liquid density
ρ_2	=	air density
θ	=	static contact (wetting) angle
ρ_1	=	liquid density
g	=	gravitaional acceleration
ρ_1	=	liquid density
Δp	=	pressure difference
L	=	characteristic length
\bar{U}	=	fluid velocity
B_o	=	bond number ($\rho g L^2 / \sigma$)
R_T	=	cylinder radius
\bar{E}	=	total surface energy
\bar{A}_{FS}	=	free surface energy (area)
\bar{A}_{wet}	=	wetted surface energy (area)
AR	=	aspect ratio
VOF	=	Volume of Fluid
α	=	fluid fraction
F	=	volume fraction
C_o	=	courant number
$E_{kinetic}$	=	kinetic energy
We	=	weber number

Abstract

The current study investigates the dynamics of a two phase flow in a circular cylinder under zero gravity conditions. Zero gravity fluid mechanics is applicable in both spaceflight and terrestrial applications. Plug formation obstruct lung passages and is the cause of asthma and pulmonary disease. In spaceflight applications, the helium bubbles occlude fuel lines of hydrazine arc-jet thrusters on satellites which cause operational problems. The process of plug formation is not fully understood. Previous studies have been limited to static solutions in cylinders. The goal of the current study is to investigate the dynamics of two phase flow under zero gravity conditions and low bond numbers. The specific objectives of this study are to model a two-phase flow into a circular cylinder via a side tube in zero gravity and confirm the existence of droplet, annulus, and plug topologies through experiment and simulation. Interim stages between topologies and steps of transition are analyzed in terms of flow quantities such as flow rate and kinetic energy. The effect of varying inlet pressure on topology formation is also determined and investigated. An experiment was conducted to determine the dynamics of silicone oil-air interface in a cylinder under low bond number conditions using a high speed camera to capture the fluid. Numerical simulations were carried out for both static and dynamic conditions. Results confirmed the existence of droplet, annulus and plug for the dynamic system. A characteristic time where plug is formed is identified and has a value of approximately 13. An instability regime between the annulus and plug was identified which gets narrower for higher pressure differences. Stable plug solutions are delayed for lower pressure differences. Stable plug solutions in dynamic systems were found to be higher than those in static systems under the same conditions.

CHAPTER 1

Introduction

Zero-gravity fluid mechanics involves the study of the kinetics and kinematics of fluid under reduced gravity conditions. Diverse fields share an interest in multiphase statics and dynamics problems in low gravity environments. Experimental studies pertaining to zero-gravity fluid mechanics have included low orbit capillary fluids experiments as well as terrestrial, controlled laboratory tests. Liquid droplets in lung passages and air bubbles in blood vessels are of interest in the biological sciences. Similarly, in the physical sciences, helium bubbles in hydrazine fuel lines where satellites employ hydrazine arc-jet thrusters for space related operations cause operational problems.

As lungs are inflated and deflated, fluid plugs or menisci form across airway lamina. This obstruction by the plug has been argued to play a major role on illnesses such as asthma and chronic obstructive pulmonary disease. Nonetheless, the conditions leading to the formation of these obstructions are still not completely understood. Likewise, spacecraft fuel tanks rely on auxiliary reservoirs to prevent the intake of gas into engines which obstruct the flow of fuel, and, as mentioned above, helium bubbles in hydrazine fuel lines constitute a major issue in station-keeping operations.

Consequentially, researchers are interested in answering questions of interest among which are: How small or large of a liquid volume (seal-off volume) is sufficient to block an air passage? What are the equilibrium solutions for volumes less than the seal-off volume and how stable are these solutions? What is the relationship between contact angle and the solution at the equilibrium states? Significant research has been carried out to answer these questions but have

been limited to static stability solutions [1, 2]. This thesis attempts to study the dynamic effects of the macroscopic fluid flow in a circular cylinder under reduced gravity conditions.

1.1 Goal and Specific Objectives

The main goal of this research is to study the dynamics of two phase flow under zero gravity conditions. Process of plug formulation is not fully understood under low bond number conditions and neither is the topology transition mechanism. Previous studies have been limited to static solutions; hence, the need for a dynamic study[1].

The specific objectives of the current study are to:

- Model a two-phase flow into a circular cylinder via a side tube in zero gravity and confirm the existence of droplet, annulus, and plug topologies through experiment and simulation
- Analyze the interim stages between topologies and describe the steps of transition in terms of flow quantities such as flow rate and kinetic energy
- Determine the effect of varying inlet pressure on topology formation.

This thesis is organized as follows: Chapter 2 presents a review of previous studies carried out on the interface of two-phase fluid statics and interface capturing schemes of dynamic bubbles. Chapter 3 presents the materials and methods used in this study to investigate the dynamics of a two-phase fluid. The problem is presented, and the basic equations of the fluid and interface capturing scheme Volume-of-Fluid (VOF) are described. A grid independence study is carried out to validate numerical results. Also, the experiment to be conducted is described. In chapter 4 interface topology results are presented as a function of time and applied pressure difference. The flow quantities, time-dependent volume, flow rate and kinetic energy are

provided and analyzed. In Chapter 5, the conclusions of the current study and recommendation for additional studies are presented. Finally, the last section provides a list of reference

CHAPTER 2

Literature Review

2.1 Basic concepts

Surface tension σ , an interface property which has units of N/m, plays a significant role in multiphase flows under low gravity conditions. It is important in determining interface characteristics and, in the case of negligible gravitational forces, can affect bulk flow. The complexities associated with intermolecular interactions renders the phenomena of surface tension and corresponding interface properties difficult to define in explicit terms. Nonetheless, many engineering analysis have resulted in two-dimensional relationships that help, to some extent, describe the interface[3].

Capillary phenomena are a consequence of surface tension which is a property dependent on the materials on either side of the interface and is sensitive to temperature. The gas-liquid interface interacts with a solid wall that forms the contact line at a measurable angle, referred to as the contact angle. The contact line, a geometric idealization, is either static or dynamic depending on if the contact line moves. A microchannel is a capillary scale system within which surface tension forces are dominant. Micro-channels have dimensions less than the characteristic length, capillary length, defined as $L_c = \sqrt{\frac{\sigma}{\rho g}}$, where ρ is the density of the liquid and g is the acceleration due to gravity. This condition corresponds to a bond number $B_o \ll 1$, where $B_o = \rho g L^2 / \sigma$.

The interface free surface has a tendency to minimize its energy to acquire an equilibrium state as surface tension is a direct measure of this energy loss per unit area of surface. The tendency of a free surface to move from a high energy to the more favorable less energy state consequently leads to a reduction in surface area. The fluid is considered to be in an equilibrium

state when following hydrostatic conditions are satisfied: (a) Euler condition; (b) Laplace's condition; (3) Dupré-Young condition [3-5]

The free surface is considered to be in an equilibrium state at each instant of time if the system parameters change gradually. Due to dissipation of energy, the effects of inertial forces remain less than that of surface tension. Therefore, a static configuration of liquid in the flow field can provide useful information on liquid behavior in capillary systems. Colosqui et al. [6] proposed an analytical method to determine plug volume under uniform wetting conditions in square acrylic channels. Based on their observations, the plug volume depended very little on fluid flow rates; suggesting that static computations of plug volume is appropriate. Surface Evolver (SE), experimental mathematics program, has been established as an efficient program for studying capillary surfaces based on a static equilibrium model[7].

SE [8] has been a valuable research tool for applications such as predicting the location of fluid in zero gravity, computing the rheology of foams, modelling cell membranes and classifying minimal surface singularities. Surface Evolver minimizes the total energy. The minimization is carried out on an initially defined surface using the gradient descent method.

A cursory investigation conducted by Chen et al. [7] comparing the abilities of OpenFoam and SE to study capillary surface properties conveys the SE niche. Although OpenFoam, a CFD toolbox which comprises an object-oriented C++ open source library supplied with a complete set of pre-configured solvers and utilities.

The primary motivation for this study is the research carried out by Collicott, Lindsey and Frazer [1] where the existence and stability of topologies are discovered and mapped for bubbles and droplets in a circular cylinder; which was built on the analytical study conducted by Slobozhanin [9].

Slobozhanin analytically determined the minimum energy solutions for axisymmetric plug and annulus topologies. On the other hand, Collicott et al. [1] incorporated the use of Surface Evolver to compute the energies of axisymmetric plugs and annulus as well as non-axisymmetric wall-bound droplet minimum energy solutions. The map of the solutions determined by Collicott et al.[1] presented in a Volume-Contact angle space represent the stable solutions and the dominant corresponding topologies. Each possible topology that exists is either stable or unstable. Possible transitions and dynamics of the local flow are not considered in study conducted by Collicott et al. [1], although by solving for minimized surface energies stable solutions were found. Figure 1 shows that only one of three possible annulus solutions is stable.

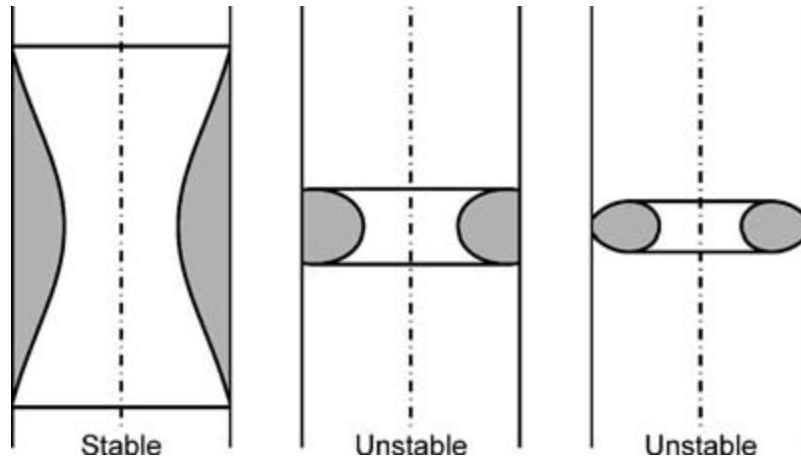


Figure 1 Stable and unstable annulus solutions[1]

Collicott, Lindsey and Frazer [1] showed that stable solutions for plug exist for all contact angles with volume being a function of only contact angle, θ , and cylinder radius, R_T . The plug free surfaces are regarded as identical spherical caps whose radius of curvature, R , is related to the contact angle, θ , through the cylinder radius, R_T , by the expression:

$$R = \frac{R_T}{\cos \theta} \quad (2.1)$$

Where $R_T = 1$ and θ is a variable.

The plug is formed at a minimum volume in the cylinder when the two free surfaces meet at the center or at the perimeter of the tube

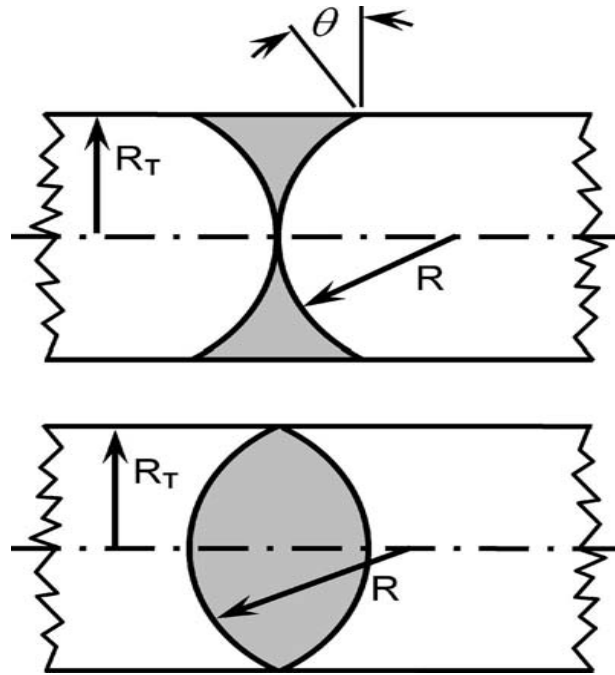


Figure 2 Two possible solutions of plug[1]

When the plug volume is formed by the spherical caps meeting at the perimeter for a cylinder radius of unity the expression used is:

$$V_{min,P} = -\frac{2\pi}{3} \left(\frac{2-3\sin\theta+\sin^3\theta}{\cos^3\theta} \right) \quad (2.2)$$

For case where the of spherical caps meet at the center, the minimum volume is:

$$V_{min,C} = 2\pi \left(\frac{1-\sin\theta}{\cos\theta} \right) - \frac{2\pi}{3} \left(\frac{2-3\sin\theta+\sin^3\theta}{\cos^3\theta} \right) \quad (2.3)$$

For the case where the cylinder radius is not unity,

$$V_{min,P} = -\frac{2\pi}{3} \left(\frac{2-3\sin\theta+\sin^3\theta}{\cos^3\theta} \right) \quad (\theta^\circ \leq \theta \leq 90^\circ) \quad (2.4)$$

$$V_{min,C} = 2\pi \left(\frac{1-\sin\theta}{\cos\theta} \right) - \frac{2\pi}{3} \left(\frac{2-3\sin\theta+\sin^3\theta}{\cos^3\theta} \right) \quad (90^\circ \leq \theta \leq 180^\circ) \quad (2.5)$$

The above expressions are used for the liquid plugs in gaseous filled tube under negligible gravity conditions. The solution for the case where the plug is gaseous and the tube is filled with liquid is determined by substituting $(\pi - \theta)$ for θ . Droplet topology, unlike plug and annulus, is non axisymmetric. The droplet wicks around the circumference to form the annulus as volume increases for wetting liquids. For non-wetting liquids, the plug expands or inflates faster than it wicks around the circumference until it fully blocks the tube which forms the plug. The method used to compute the surface energies in Surface Evolver for the plug makes use of the equation:

$$\bar{E} = \bar{A}_{FS} - \cos\theta\bar{A}_{wet} \quad (2.6)$$

, which is the weighted sum of the non-dimensional free and wetted surface energies. \bar{E} is the total surface energy, \bar{A}_{FS} is the free surface energy (area), \bar{A}_{wet} is the wetted surface energy (area) and θ is the contact angle. The energy and surface areas are non-dimensionalized using the product σR_T^2 where σ is the surface tension and R_T is the cylinder radius. The variable θ plays an important role in the minimization of energy process and determines the degree of wetting.

The areas \bar{A}_{FS} and \bar{A}_{wet} are evaluated using the following expressions:

$$A_{FS} = \frac{4\pi R_T^2}{1+\sin\theta}, \quad (2.7)$$

$$A_{WS} = \begin{cases} \frac{4\pi R_T^2(1-\sin\theta)}{\cos\theta} & \text{for } (0^\circ \leq \theta \leq 90^\circ) \\ 0 & \text{for } (90^\circ \leq \theta \leq 180^\circ) \end{cases} \quad (2.8)$$

The computed energies in Surface Evolver are compared to determine which solution or topology is the minimum energy solution for each volume and contact angle. Figure 3 shows the map of the minimum energy solutions in a two-dimensional Volume-Contact Angle space for a straight tube or circular cylinder.

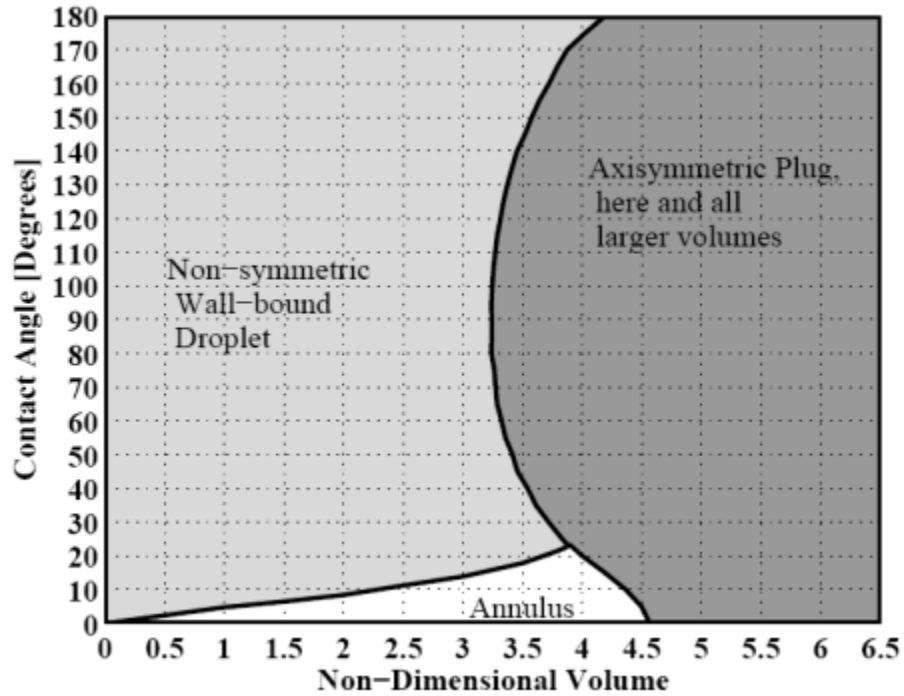


Figure 3.. Minimum energy solution map in $V - \theta$ space.

For large volumes ($V \geq \sim 4.5$), the plug is the stable solution for all contact angles. The droplet is the solution for all smaller volumes except the white region which is dominated by the annular solution for contact angles below roughly 20° .

In a manner similar to the case of a circular cylinder, Jaron computed the minimum energy solutions for laterally compressed tubes. Jaron [10] expanded on research involving lung airways by Heil [11, 12] where the existence and stability of static liquid bridges in non-asymmetrically buckled elastic tubes was analytically studied.

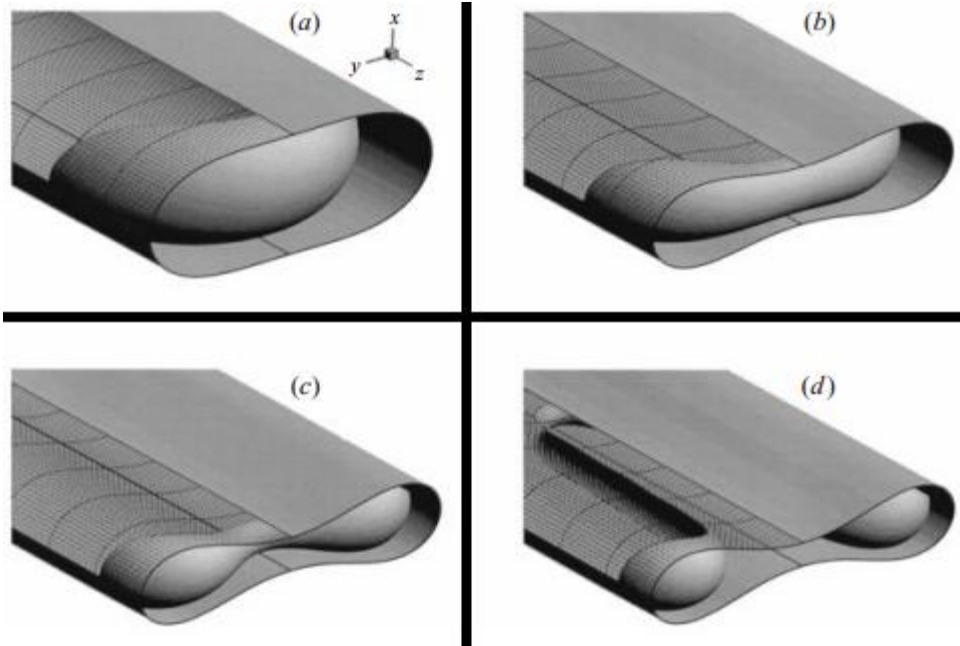


Figure 4. Heil's elastic tube used for liquid bridge plug stability studies [11].

Jaron defined lateral compression in terms of an aspect ratio (AR) between the height and width of the tube cross section ($AR = \frac{Height}{Width}$) (Figure 5).

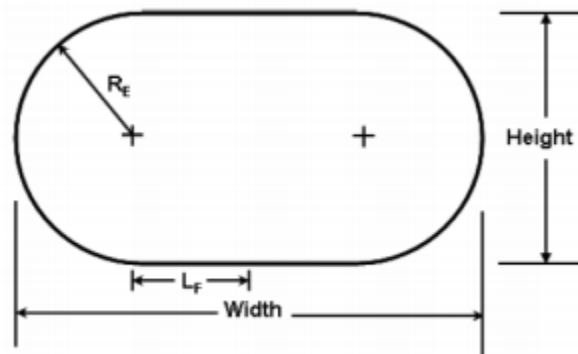


Figure 5. Terms of Aspect Ratio

Six possible equilibrium solutions are possible in this tube: plug, annulus, liquid bridge and droplets (three configurations) (figure 6.)

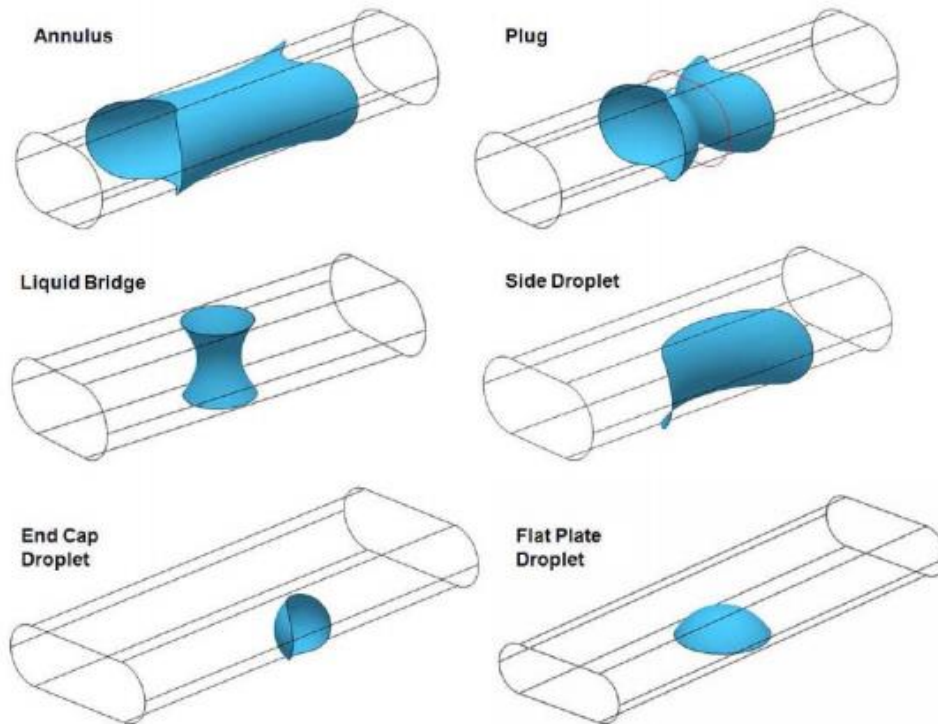


Figure 6. Possible topologies for lateral compression[10]

Jaron's research showed that the slight deviations from the circular cylinder cause significant changes to the stability map. For an aspect ratio of 1.1, the plug solution is much more dominant than in the case of unity aspect ratio. The plug is the stable solution for volumes above approximately 2 for contact angles below 20° and 4 for all contact angles. For higher aspect ratios above 1.5, the minimum plug solution boundary shifts towards the right of the volume axis while the droplet solution region is expanded. The annulus region is also eliminated. (figure 7)

The breakdown of symmetry leads to an elimination of the stable annulus solution in laterally compressed tubes. These results suggest that highly compressed tubes reduce gas occlusions in liquid filled tubes as well as liquid plugs in gas filled tubes as the plug formation is delayed for all contact angles at high aspect ratios.

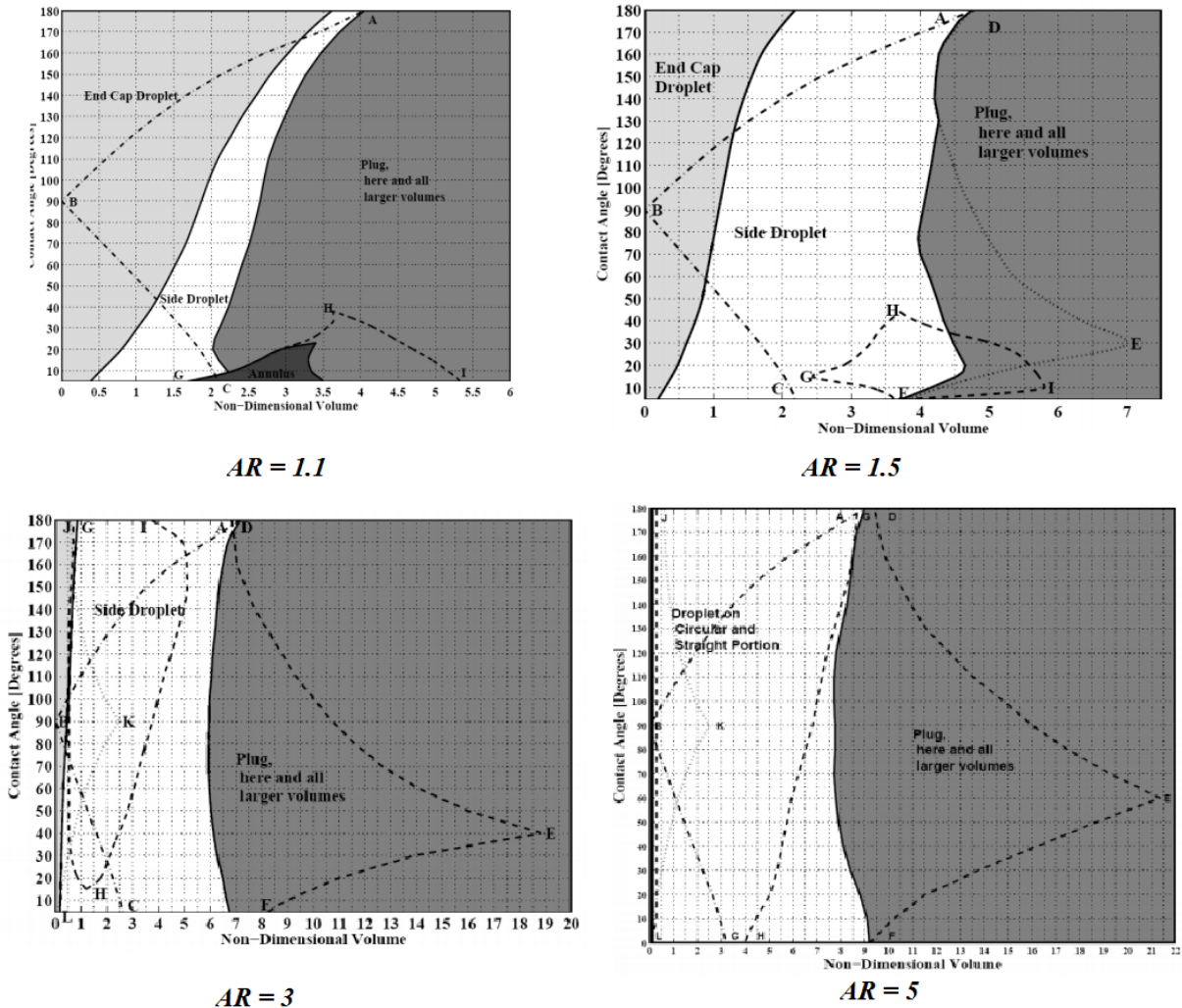


Figure 7. Minimum energy topology maps for laterally compressed tubes of different aspect ratios[10].

2.2 Surface Evolver and OpenFOAM for Studying the Shape and Stability of Capillary Surfaces

Mathematical solutions of the topology and stability of equilibrium capillary surfaces is challenging. Current theory on capillary surfaces remain limited to certain classes [5]. As a consequence, numerical methods are employed to find solutions. One of the valuable numerical tools used to study interface phenomena, for the past couple decades, has been Surface Evolver

(SE) - an open-source software. Compared to existing Computational Fluid Dynamics (CFD) programs, SE computes shape and stability solutions of equilibrium capillary surface more efficiently –at least an order of magnitude greater.

In SE the free surface is initialized and constrained by the geometry. In common CFD programs the geometry, comprising the solid walls and internal volumes, is meshed and the governing equations are solved for the entire domain. However, in SE only the initialized free surface is minimized using a gradient descent method [8, 13]. Once the geometry is imported (STL or STEP file), the free surface is initialized and the potential energies are for the free surface are specified. For perfect wetting cases (zero contact angle between the walls and the fluid), the free surface is created using a closed surface.

For partial wetting, the contact line between the solid walls and the fluid is facilitated with integrals along edges – *Contact Line Integral Method* (CLIM) - or with the *Artificial Velocity Method* (AVM) where all the vertices of the free surface are categorized into layers based on their proximal relationship to the contact line. These two methods eliminate the problem of near zero velocity of the surfaces constrained at the walls [7]

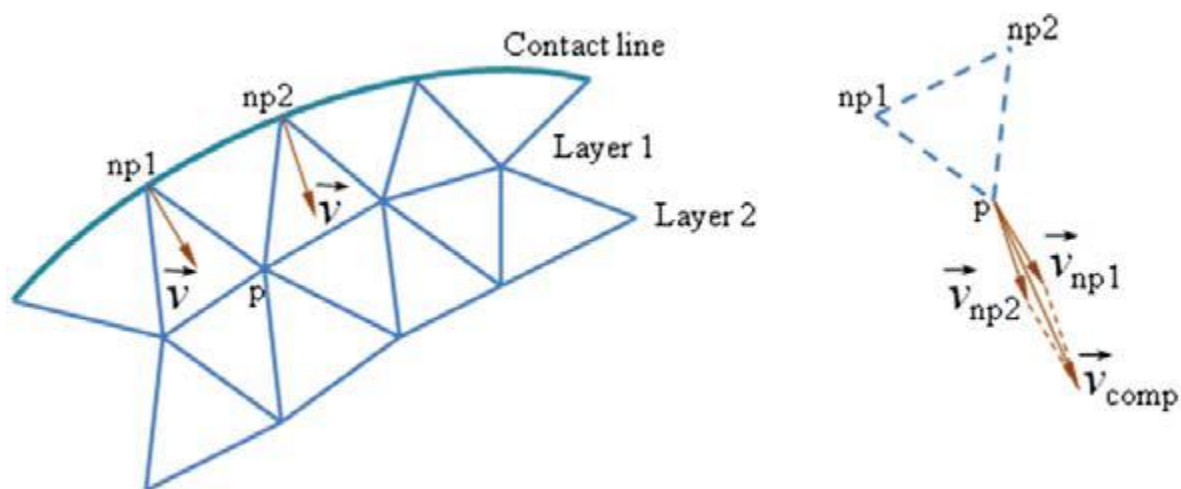


Figure 8. Representation of Artificial Velocity Method approach [7]

In AVM, the velocity of an inner vertex, p , is computed as the weighted average of the magnitudes of the velocities of two neighboring vertices in the upper layer.

In FE, no fluid dynamics equations are solved. The gradient descent method minimizes the energy of the free surface which has zero thickness, without being too concerned with the bulk fluid; although mass is conserved in the computations. In OpenFOAM, fluid mechanics equations are solved for the entire fluid bulk and the free surface has a finite thickness.

Chen et al. [7] computed the capillary behavior of silicone oil in a cubic container of a 1 cm side. The container is filled to 30% and allowed to wick, in zero gravity, along the edges until the fluid meets at the opposite side. The method used to capture the interface flow in OpenFOAM was the Volume-of-fluid (VOF) method.

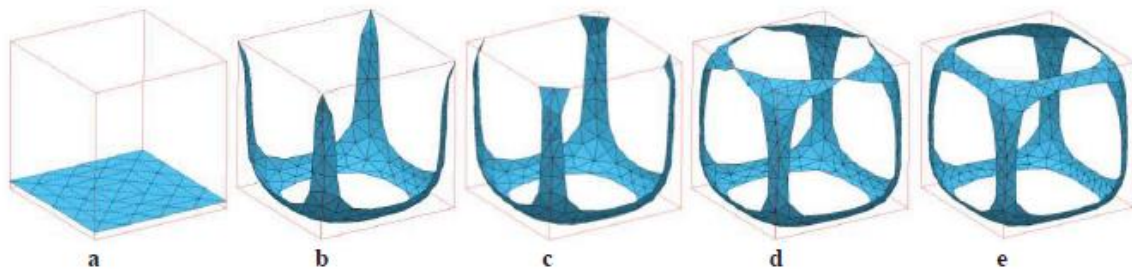


Figure 9. Wicking of silicone oil along edges under low gravity

It was noticed that after 3seconds (a computation time of 3288 seconds) of computations the pressure difference across the interface converges to a finite value but the absolute pressures of the air and the oil continue to change. For the same resolution and set up, the computation time for SE was 20 times less – 155 seconds. Both methods conserve volume to a high degree (< 1%). The interface for FE covers 32% more area than that for OpenFOAM and the mean curvature of the interface in OpenFOAM was found to be 18% lower than that for SE-FIT.

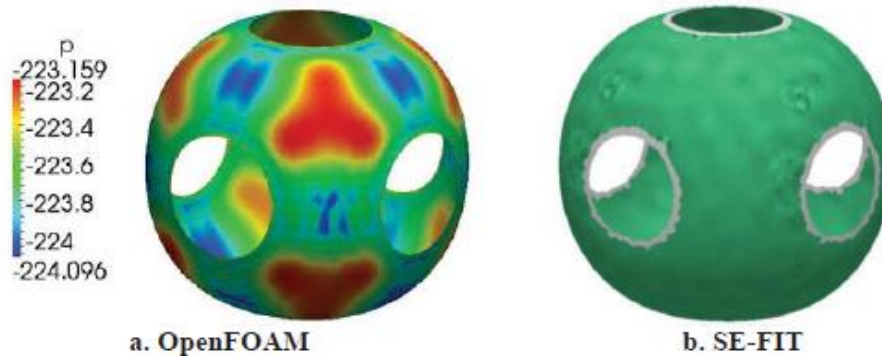


Figure 10. Interfacial pressure distribution in OpenFOAM and surface Evolver

2.3 Numerical Modelling of Multiphase Flows in CFD with VOF

Numerical methods for computing fluid flows with interfaces can be divided into two types: Moving and fixed grid based computations. The moving grid method (Lagrangian) treats the interface as sharp boundary whose motion is tracked thereby dividing the computation domain into more than one domain. The fixed grid method (Eulerian) assumes the grid cells are filled either completely or partially with a fluid. The interface position is calculated within the partially filled cell grids at each time step. The fixed-grid methods have the advantage that they can resolve topological changes and deformations of the interface, however they fail to accurately represent surface tension forces accurately [14]

Among the most important techniques used in fixed-grid methods are the *volume-of-fluid* and the *level-set* approaches [15, 16]. The level-set method makes use of a level-set function ϕ which is initialized as a signed distance function from the interface – designated as positive on one side of the interface, zero at the interface and negative on the other side [15, 17]. The interface evolves as a solution of the transport equation for ϕ which introduces a problem. ϕ does not remain a distance function at later times of the computation which manifests itself in interface smearing and problems with conserving mass. Sussman et al. [18] introduced re-initialization techniques to address this problem. One of the intrinsic strengths of the level-set

method is that ϕ varies smoothly across the interface which leads to convenient expressions for the curvature and the interface normal vector. [17]

In the Volume-of-fluid (VOF) method, the volume of each fluid, and not the interface itself, is tracked in each cell. A volume fraction, F , is defined for each fluid ranging from zero (for a cell void of liquid) and unity (for a cell completely filled with a liquid). The interface is located in the multi-fluid cells with a liquid fraction in the range $0 < F < 1$.

VOF algorithms consist of three main parts: *interface reconstruction*, *F advection algorithm* and the *surface tension model*. Early interface reconstruction employed the Simple line interface calculation (SLIC) [19] and the Piece-wise Linear interface calculation (PLIC) [20]. The PLIC method of Youngs[20] displayed high efficiency and robustness although it was of first order accuracy. Puckett et al. [21] devised an improved version of phase interface representation of second order accuracy – Least squares VOF interface reconstruction algorithm (LVIRA) - which was successfully implemented by Welch and Rachidi [22] to study bubble formation in film boiling.

Gerlach et al. [14] compared three interface reconstruction methods incorporating different surface tension models to predict flow properties. The accuracy, the convergence behavior and the influence of “parasitic currents” (a result of inaccurate calculations of the surface tension force[23]) was studied in detail for the following groups of algorithms:

- LVIRA [21] for interface reconstruction and K8 kernel for surface tension model
- PROST[24] for both interface reconstruction and surface tension model.
- CLSVOF [16, 18, 25] for both interface reconstruction and surface tension model.

Results show that PROST was superior to the K8 kernel and CLSVOF methods in terms of accuracy and reduction of the parasitic currents. However, in terms of computational cost,

PROST was more expensive as it entailed optimizing the least-square function. K8 kernel demonstrated significant weakness in its ability to predict surface tension forces. CLSVOF showed relatively accurate results and was the least computationally expensive.

The figure below shows the solution to a damped oscillation of an interface between two viscous fluids without external forces. The analytical solution of Prosperetti [26] was used as a measure against which PROST, CLSVOF and K8 numerical solutions were compared. The solutions of PROST and CLSVOF methods were indistinguishable from the analytical solution whereas K8 performed poorly.

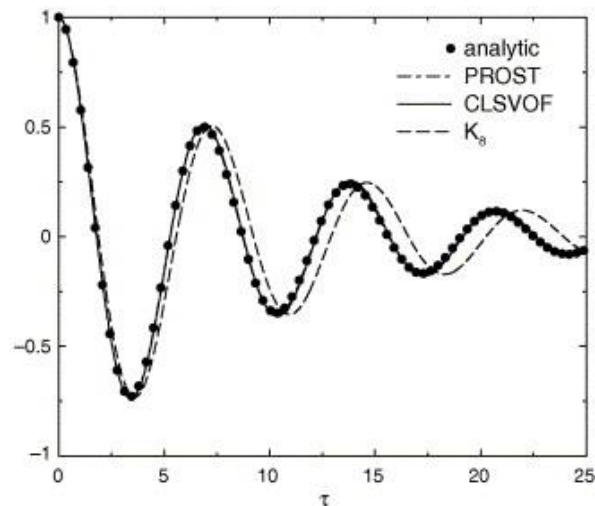


Figure 11 Comparison of analytical, PROST, CLSVOF, and K8 solutions

VOF has also been used to study the behavior of bubbles. In the analysis of subcooled boiling flows for the optimization of design and safety of nuclear systems, the characteristics of bubbles are studied. Vapor bubble- water interface interactions affect the heat transfer characteristics of subcooled boiling flows due to phenomena such as condensation, break-up and coalescence of bubbles. The dynamic behavior of rising bubbles has been studied by simulating bubble size, shape, rising trajectory and velocity using the VOF method [27-30].

Seong-Su Jeon et al [31] evaluated the performance of the VOF method to model the amount of condensation using interfacial heat transfer coefficient obtained from the velocity, liquid temperature and diameter of rising bubbles. The study found the VOF method to be a useful in predicting the behavior of the condensing bubble in a wide range of subcooled boiling flow.

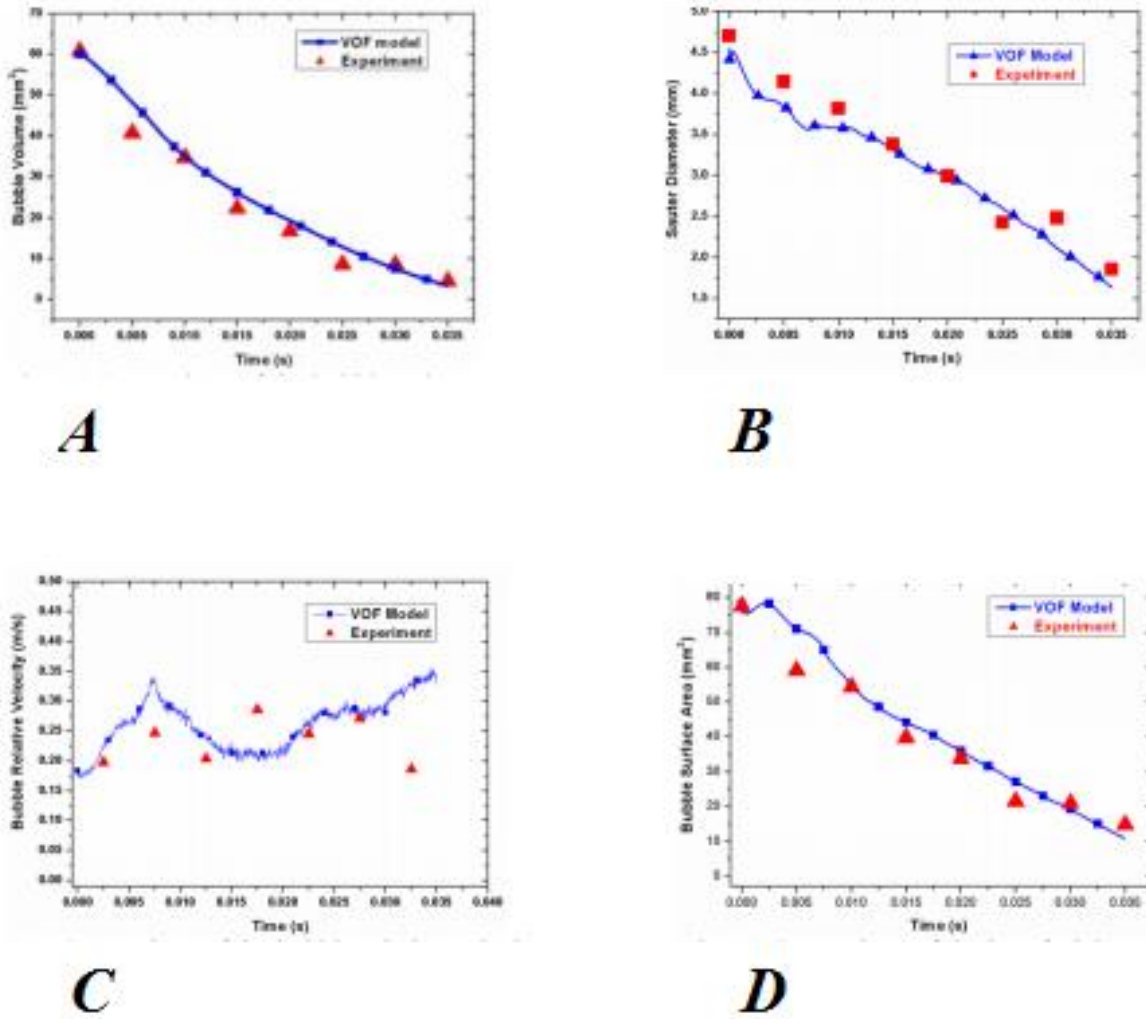


Figure 12. Comparison of VOF and experiment. A. Comparison of bubble volume B. Comparison of bubble diameter. C Comparison of relative bubble velocity. D Comparison of interfacial Area

Figure 7 shows the agreement of VOF quantities with experiment in [31]

CHAPTER 3

Problem Formulation and Methodology

3.1 Fundamental Questions of Investigation

According to Collicott et al. [1], the static topological solution map is a function of contact angle and injected volume – two-dimensional solution map. Assuming there is no phase change, the amount of liquid present in the circular cylinder coupled with the predominant contact angle between the walls of the container and the liquid determine the topology of the free surface. The fundamental questions this thesis attempts to investigate and answer are: Is the static solution map applicable under dynamic conditions? In other words, what other factors can affect the topology of the free surface in circular cylinders under zero gravity conditions. If the formation of annulus and plug depend on initial and boundary conditions, can their inception and dynamic behaviors be predicted? Will different boundary conditions result in the same solutions?

3.1.1 Problem Setup

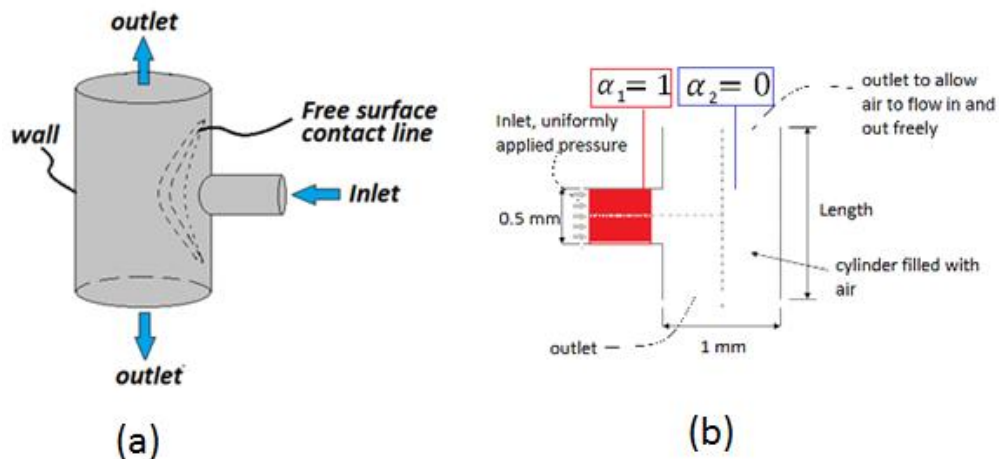


Figure 13 Schematic of Circular Cylinder Model

The dynamic interface problem investigates the motion of fluid 1 (silicone oil) injected via a side tube into a main cylinder filled with fluid 2 (air) (figure 13(b)). As illustrated in figure

above (a), the liquid is continuously injected through the inlet into the air-filled circular cylinder until the cylinder is completely filled with liquid. The cylinder is open to the ambient at the two outlets, through which fluid mass is allowed to pass unhindered. The driving force is the pressure difference between the inlet and outlet (s). The dynamic shape (s) of the interface as the process progresses with time is monitored and the volume of liquid along with the integral kinetic energy and the flow rate at the inlet at each time step is computed.

3.2 Basic Equations

The region containing liquid is initialized in the computation domain (shown in red (figure 13 (b))). The flow quantities are then determined by solving the transient Navier-Stokes equations coupled with the Volume-Of-Fluid (VOF) interface capturing scheme. The system of equations – Navier-Stokes and VOF – was simultaneously solved using modified OpenFOAM 2.3 solvers. The geometry was created and meshed using Salome-Meca. All CFD packages used for this thesis were open-source software.

To track the two-phase flow, the VOF method of Hirt and Nicholas [32] is adopted. Here a volume fraction , α , is used to mark fluid 1 defined as (equation (3.1)):

$$\alpha_i = \begin{cases} 1 & i = 1 \text{ for liquid} \\ 0 & i = 2 \text{ for air} \\ 0 < \alpha < 1 & \text{at the interface} \end{cases} \quad (3.1)$$

The solved sets of equations describing the fluid flow are as follows: laminar and incompressible continuity equations (3.2); unsteady, laminar and incompressible Navier Stokes (3.3); and the VOF equations ((3.4-3.5)).

$$\nabla \cdot \bar{U} = 0 \quad (3.2)$$

$$\frac{\partial(\rho\bar{U})}{\partial t} + \nabla \cdot (\rho\bar{U}\bar{U}) = -\nabla p + 2\nabla \cdot [\mu\vec{D}] + \rho\bar{g} + \sigma\kappa\nabla\alpha_i \quad (3.3)$$

Here, \bar{U} is the velocity, p is the pressure and \bar{g} is the acceleration due to gravity. The fluid properties are weighted by the volume fractions of the respective fluids

$$\rho = \alpha_1 \rho_1 + (1 - \alpha_1) \rho_2, \quad \mu = \alpha_1 \mu_1 + (1 - \alpha_1) \mu_2 \quad (3.4)$$

The rate of strain is defined as

$$\vec{D} = \frac{1}{2} (\nabla \bar{U} + (\nabla \bar{U})^T) \quad (3.5)$$

The transport equation of each volume fraction α_1 and α_2 in the incompressible two-fluid system is given by

$$\frac{\partial \alpha_i}{\partial t} + \nabla \cdot (\bar{U}_i \alpha_i) = 0, i = 1, 2 \quad (3.6)$$

At the inlet, a Dirichlet pressure boundary condition is specified for the different pressures: 0 Pa, 30Pa, 60Pa, 90Pa and 120 Pa. The boundary conditions at the outlets take a Neumann form with zero gradients to allow outflow. At the walls, the no-slip condition is implemented throughout the domain except at the interface. The contact angle is assumed static and specified a value of 10° at the wall.

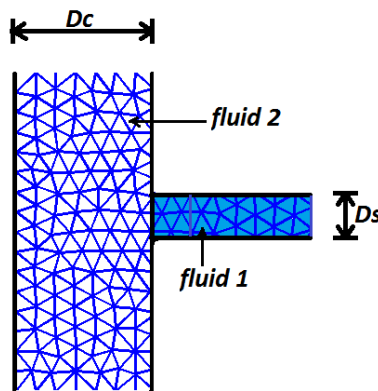


Figure 14. Cross-section of modeled T-section

Due to the complexity of the computations, the size of the computation domain was reduced such that there was just enough space for the different topologies to form freely. This was done by running preliminary computations on an initial mesh and truncating superfluous sections. The mesh was unstructured and comprised tetrahedral volumes to account for the non-axisymmetric nature of the solutions from the initial computations. Furthermore, initial computations revealed a susceptibility to contact line breakage. This problem could have been due to numerical diffusion. To rectify this problem, further computations were run for various volume cell sizes until the contact line displayed a continuous nature and localized pressures and velocity distributions were contained. Table 1 lists the input parameters that describe initial conditions based on the schematic in figure 14

Table 1

Model Properties

Property	Description	Value/Type/Nature
Fluid 1	Injected liquid	Silicon oil
Fluid 2	Fluid in the circular cylinder	Air
Circular cylinder Diameter, Dc	Constrained by bond number and machinability	0.001m
Injection tube/Side tube Diameter	Constrained by bond number and machinability	0.0005m
Model Type	Non-symmetrical nature of the solution to be considered. Hence, unstructured grid.	Three-Dimensional

Table 1

Cont.

Bond number	Has to be less than one i.e. $Bo < 1$	Numerical: Bond number = 0 Experiment: Bond number = 0.47
Inlet condition	Simulation: Pressure is specified. Experiment: Pressure is difficult to be specified. Inlet velocity is derived from experiment.	Pressure difference for each case, $\Delta p = 0,30,60,90, \text{ and } 120.$
Outlet conditions	Initial pressure gradients across the outlets are zero.	Pressure = 0

Table 2

Initial conditions

Initial conditions/Properties	value
Silicon oil density, ρ_s [kg/m³]	860
Air density, ρ_a [kg/m³]	1.00

Table 2

Cont.

Silicon oil kinematic viscosity, γ_s [mm²/s]	1.0
Air kinematic viscosity, γ_a [mm²/s]	0.148
Acceleration due to gravity, g [m/s²]	9.81
Surface tension of silicone oil, σ [N/m]	0.0175
Ambient Pressure [Pa]	0
Ambient Temperature [K]	273

As mentioned above, the Volume-of-Fluid (VOF) method was used to track the fractions of air and silicone oil. The computation domain was initialized by setting the boundary conditions and discretely defining the regions that contain that fluid. The time-dependent Navier-Stokes was solved using the PIMPLE algorithm.

In order to ensure convergence of the solutions, the courant number was limited to a maximum value of 0.2. The injection weber number was chosen to be less than 1.5 for this thesis to prevent the formation of geysers [33]. The courant condition for a three-dimensional case can be defined as:

$$C_o = 3\delta t \frac{|U|}{\delta x} \quad (3.7)$$

$$W_e = \frac{E_{kinetic}}{E_{surface}} \quad (3.8)$$

Where

$$E_{kinetic} = \frac{\pi \rho l^3 U^2}{12} \quad (3.9)$$

And

$$E_{surface} = \pi l^2 \sigma \quad (3.10)$$

Where δt is the temporal length, $|U|$ is the magnitude of the maximum velocity (from weber number); δx is the spatial size; ρ is the density of silicon oil $860\text{kg}/\text{m}^3$, l is the characteristic length (0.0005m). The velocity corresponding to a weber number, W_e , of 1.5 and based on the equation (3.8) is 0.9 m/s. Using 0.9 m/s for maximum velocity, 0.2 for maximum courant number and cell dimension of $1 \times 10^{-5}\text{m}$, the maximum time-step, Δt_{max} , (calculated from equation 3.7) is $2.5 \times 10^{-5}\text{sec}$. Consequentially, the time-step used for computations was $1 \times 10^{-9}\text{ seconds}$, which is less than Δt_{max} , to avoid non-convergence problems.

Initial calculations using PIMPLE with one pressure correction term gave rise to unstable results and interface breakup. This suggests that SIMPLE is not very stable for this problem – setting the pressure correction term from one to two or above switches PIMPLE mode from SIMPLE to PISO. It is advantageous to use PISO mode, instead of SIMPLE, to solve this time sensitive problem, however, although PISO is more computationally expensive than the latter. It should be noted that SIMPLE does not resolve time as accurately - it uses relaxation factors - ; and expectedly would perform poorly for the current transient problem. SIMPLE performs efficiently for steady-state cases with relatively larger time-steps. The pressure term was corrected 3 times for this thesis. The PIMPLE algorithm is implemented as follows (simplified): Pressure is guessed and set as boundary conditions.

1. The momentum equations are solved for the velocities.
2. The continuity equation is solved and if mass is not conserved the pressure is corrected.
3. The pressure equation is solved for new pressure field.

4. The momentum equations are solved using the new pressure field to get new velocities
5. Boundary conditions are updated.
6. The steps 3 through 6 are repeated for the number of corrector steps

The PIMPLE algorithm is an iterative process that utilizes one predictor step and multiple (specified) corrector steps. Three corrector steps were used for this thesis.

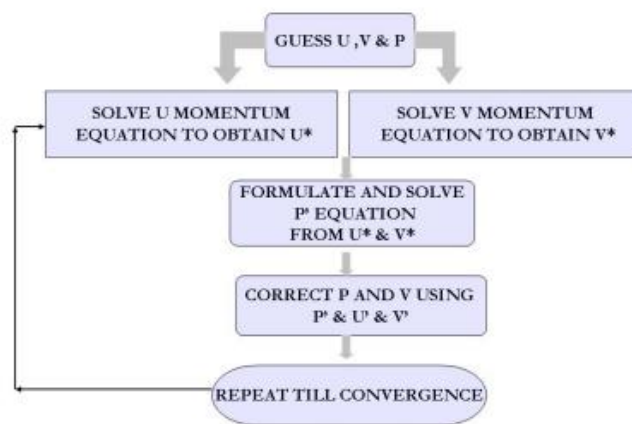


Figure 15 Flow chart of PIMPLE algorithm

3.3 OpenFOAM: Introduction

OpenFOAM is an acronym that stands for the “Open Source Field Operation and Manipulation.” It comprises a number of applications that utilize a C++ library that perform calculations, especially pertaining to computational fluid mechanics, and provide a range of pre- and post-processing functionalities. Information about OpenFOAM can be obtained from a number of sources, including but not limited to [34-36]. According to the OpenFOAM website, the CFD package is used by R&D teams in large companies such as Audi, Shell and Mitsubishi as well as universities worldwide among them Imperial College, Chalmers University, Tokyo Institute of Technology and Ohio State University.

3.3.1 OpenFOAM Features

OpenFOAM consists of a set of reusable applications that perform computations and simulations using a C++ library. The applications are categorized into two sections: Solvers that perform the calculations and Utilities that support the simulation process by performing pre- and post-processing operations. The impressive range of solvers include: simple potential flow solver (potentialFoam), transient laminar solver (icoFoam), turbulence flow solver (turboFoam), electromagnetics solver (mhdFoam), trans- and supersonic turbulent solvers (sonic-TurbFoam), multiphase flow solvers (interFoam) among others. This thesis utilizes the multiphase solver interFoam which is based on the VOF scheme.

Among the preprocessing utilities used often in this thesis are: ideasUnvToFoam which converts UNV mesh files to an OpenFOAM friendly format for processing; blockMesh that generates the mesh files for the case, checkMesh which inspects the mesh for inconsistencies and errors, setFields which is used to set initial conditions for different volume fields. Furthermore, the most common post-processing utilities used in this thesis include: sample used to collect arbitrary quantities at specified locations and foamLog which extracts data such as residuals, iterations and Courant number from a log file over a period of time.

To view and post-process simulations graphically, OpenFOAM provides a reader module for the open source visualization application paraview (paraFoam). A third-party application Swak4FOAM, which contains a versatile C++ library to augment OpenFOAM's, was also used for calculating quantities such as flow rate, kinetic energy and volume and postprocessing purposes.

3.3.2 Components of a Case

Depending on the type of solver used cases may vary in a few subtleties, however, all cases share similar basic structure. The interFoam-solver case **damBreak** was modified for the simulation presented in this thesis. The structure of the case directory is organized as follows:

- system
 - controlDict
 - fvSchemes
 - fvSolution
 - setFields
 - decomposeParDict

- constant
 - polyMesh - points; cells; faces; boundary
 - transportProperties
 - g

- 0
 - alpha.oil
 - p_rgh
 - U

The system directory contains the files that simulation control parameters such as time-step, and maximum courant number (**controlDict**) and parallel computing specifications (**decomposeParDict**); selected discretization schemes and numerical methods (**fvSchemes** and **fvSolution**); and volume field initialization information (**setFields**). The constant directory contains information about the geometry coordinates and mesh (**polyMesh**); properties of materials (**transportProperties**) and gravitational field (g). Last but not least, the boundary conditions are set in the 0 directory. In **alpha.oil**, the region that contains liquid is specified by

coordinates that intersect the geometry in **polyMesh**. Boundary pressure and velocity fields are specified in **p_rgh** and **U**, respectively.

3.3.3 Steps Outline

This section outlines the basic steps taken to run a case. It is divided into stages: Mesh matters; Setting boundary and initial conditions; Setting control parameters, transport properties and parallel computing parameters; specifying numerical solution schemes and writing scripts; and running simulation.

Mesh matters: Once the geometry was created and meshed in Salome-meca, the resulting UNV file was imported and converted to the openFOAM format using the utility `ideasUnvToFoam`. The utility `blockMesh` was then used to create the mesh which was inspected using `checkMesh`. The mesh comprised an unstructured grid made of tetrahedron volume cells as illustrated in Figures 16 and 21.

The `polyMesh` directory contains the boundary dictionary which specifies the boundary types .e.g. `patch` (generic), `wall`, `symmetryPlane`, `empty` etc. The boundary names, specified before the mesh was exported, must correspond to the boundaries in the `0` directory (where boundary and initial conditions are set).

Setting boundary and initial conditions: In this step, the pressure boundary condition in the `0` directory (`p_rgh`) is modified. The pressure at the outlets is set to zero and at the wall the boundary condition is set as a zero pressure gradient. The inlet pressure is assigned a finite value. A number of cases were run in this thesis for different inlet pressures increments of 15 Pa . The `p_rgh` file with an input pressure of 60 Pa is provided below:

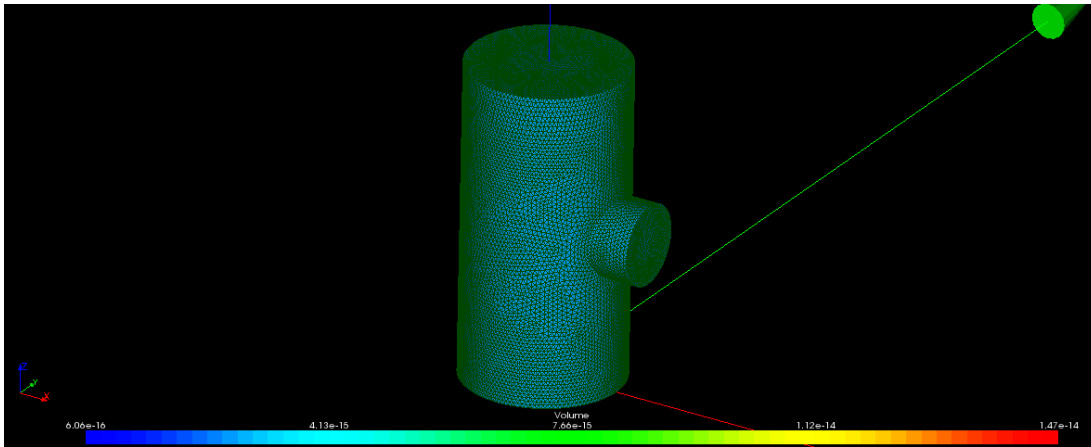


Figure 16. Three- dimensional Computational Domain

```

dimensions      [1 -1 -2 0 0 0 0];

internalField   uniform 0;

boundaryField
{
    inlet
    {
        type          totalPressure;
        p0            uniform 60;
        U             U;
        phi           phi;
        rho           rho;
        psi           none;
        gamma         1;
        value         uniform 0;
    }
    outlet1
    {
        type          totalPressure;
        p0            uniform 0;
        U             U;
        phi           phi;
        rho           rho;
        psi           none;
        gamma         1;
        value         uniform 0;
    }
    outlet2
    {

```

```

        type          totalPressure;
        p0            uniform 0;
        U             U;
        phi           phi;
        rho           rho;
        psi           none;
        gamma         1;
        value         uniform 0;

    }
    walls
    {
        type          fixedFluxPressure;
        value         uniform 0;
    }

}

```

Obviously, the setup has four boundaries designated as inlet, outlet1, outlet2 and walls.

This theme reoccurs in the velocity file U. The boundary conditions in the U file is presented

below:

```

internalField    uniform (0 0 0);

boundaryField
{
    inlet
    {
        type          pressureInletOutletVelocity;
        value         uniform (0 0 0);;
    }
    outlet1
    {
        type          pressureInletOutletVelocity;
        value         uniform (0 0 0);
    }
    outlet2
    {
        type          pressureInletOutletVelocity;
        value         uniform (0 0 0);
    }
}

```

```
walls
{
    type            fixedValue;
    value           uniform (0 0 0);
}
}
```

The velocities at the inlet and outlets are linked to the pressure boundary conditions while the zero-slip condition is specified at the walls. Finally, the region occupied by fluid 1 (silicon oil) is specified in the *setFields* file in the system directory. The fluid 1 (alpha =1) is prescribed as follows:

```
boxToCell
{
    box (0.00051 -0.1 0.0002) (0.1 0.1 0.002);
    fieldValues
    (
        volScalarFieldValue alpha.water 1
    );
}
```

The alpha 1 domain is basically a box defined at two points forming a diagonal across the rectangular box on opposite ends. The regions that intersect the geometry or mesh are assigned the alpha value 1.

Setting control parameters: The time-step and courant number are set in the **controlDict** file in the system directory.

Transport properties and parallel computing parameters: The fluid properties, density, kinematic viscosity and surface tension are specified in the **transportProperties** file in the constant folder. The kinematic viscosity and density are designated nu and rho respectively. One example of how these properties are specified is shown below:


```
oil
{
    transportModel    Newtonian;
    nu                nu [ 0 2 -1 0 0 0 0 ] 1e-06;
    rho               rho [ 1 -3 0 0 0 0 0 ] 860;
}
```

The transport model for silicon oil is assigned Newtonian. The surface tension of the silicon oil is specified at the end of the file under the term `sigma` as follows:

```
sigma                sigma [ 1 0 -2 0 0 0 0 ] 0.0175;
```

Distributing the computation work over a number of processors reduces the computation time of the simulation. OpenFOAM accommodates parallel computing by allowing the grid to be broken down into a specified number of subdomains, usually equal to the number of nodes or processors available. In this thesis, the computation domain was broken down into 16 sub-grids equal to the number of processors available for computation. The number of sub-grids or subdomains is specified in the **decomposeParDict** file in the system folder presented below:

```
numberOfSubdomains 16;

method                simple;

simpleCoeffs
{
    n                  ( 4 4 1 );
    delta              0.001;
}
```

The number of nodes is which is equal to the number of subdomains in this case, which is 16. The domain is broken down into four subdomains the x-direction, four subdomains in the y-direction and one in the z-direction [n (4 4 1) – n(x y z)].

Specifying numerical solution schemes and writing scripts: In this step, the discretization schemes that resolve the components of the constituent equations – time schemes, divergence, Laplacian terms and more - are selected in the fvschemes file. The time scheme is specified as euler and made default. The components are solved at cell centers and interpolated linearly to the cell face centers, specified under interpolationSchemes. The Gaussian finite volume integration is the method used to solve the various terms and designated by the term Gauss. The scheme that handles scalar field under grad operation is specified as Gauss linear under gradSchemes. The schemes dealing with divergence terms operating on vector fields are specified under divSchemes. In this case, no face fluxes are introduced.

```

ddtSchemes
{
    default          Euler;
}

gradSchemes
{
    default          Gauss linear;
}

divSchemes
{
    div(rhoPhi,U)   Gauss linearUpwind grad(U);
    div(phi,alpha)  Gauss vanLeer;
    div(phirb,alpha) Gauss linear;
    div((muEff*dev(T(grad(U)))) Gauss linear;
}

laplacianSchemes
{
    default          Gauss linear corrected;
}

interpolationSchemes
{
    default          linear;
}

```

```

snGradSchemes
{
    default          corrected;
}

fluxRequired
{
    default          no;
    p_rgh;
    pcorr;
    alpha.water;
}

```

The numerical method used to solve for pressure and velocity components of the Navier-Stokes and continuity equations is specified in the `fvSolution` file. The numerical method selected is PIMPLE which is initialism for the PISO-SIMPLE combined algorithm. In this thesis, the number of correctors used for the pressure and velocity field solutions is 3. Consequentially, the PISO mode is activated and the under-relaxation factors become irrelevant. The problem being tackled is not a steady-state one. PIMPLE with no momentum predictor step, one outer corrector and three corrector steps is specified as follows:

```

PIMPLE
{
    momentumPredictor    no;
    nOuterCorrectors     1;
    nCorrectors           3;
    nNonOrthogonalCorrectors 0;
}

```

The solver is the number-crunching technique employed to solve the discretized set of equations. The solver *smoothSolver* uses a smoother, *symGaussSeidal*, for its velocity calculations. *symGaussSeidal* refers to Gauss-Seidal, a reliable method, used to solve the matrix. The tolerance limits the maximum residual allowed. Once the tolerance is specified the

calculation stops and proceeds to the next stage. The relative tolerance *relTol* specifies the ratio of current to initial residual.

```
U
{
    solver          smoothSolver;
    smoother        symGaussSeidel;
    tolerance        1e-06;
    relTol           0.0001;
}
```

The pressure components, specified under *p_rgh*, are calculated by the Preconditioned (bi-) conjugate gradient solver *PCG* using a diagonal incomplete-cholesky DIC matrix preconditioning technique.

```
p_rgh
{
    solver          PCG;
    preconditioner  DIC;
    tolerance        1e-07;
    relTol           0.05;
}
```

In addition to specifying the finite volume schemes used to solve the constituent equations, additional scripts were introduced to compute quantities that OpenFOAM did not offer. A C++ script was written to calculate the volume flow rate at the inlet patch, the kinetic energy of the flow system and volume at each time step.

Running simulation: After the simulation files are edited, the appropriate utilities are called. In the case directory, the liquid region is initiated and set by calling the utility `setFields` which defines the region of the grid that contains the liquid. The liquid region is designated a fluid fraction alpha of 1 – silicone oil. The rest of the grid is automatically designated a fluid fraction of 0 – air. A successful initialization of liquid field will cause changes to the `alpha.oil` file. Before the `setFields` command is run and any changes occur, the file should look like this:

```

dimensions      [0 0 0 0 0 0 0];

internalField   uniform 0;

boundaryField
{
    inlet
    {
        type            inletOutlet;
        value            uniform 0;
        inletValue       uniform 0;
    }
    outlet1
    {
        type            inletOutlet;
        value            uniform 0;
        inletValue       uniform 0;
    }
    outlet2
    {
        type            inletOutlet;
        value            uniform 0;
        inletValue       uniform 0;
    }
    walls
    {
        type            constantAlphaContactAngle;
        theta0          10;
        limit            gradient;
        value            uniform 0;
    }
}

// *****

```

theta0 under the section *walls* sets the contact angle (10° in this thesis). The boundary descriptions must correspond to the mesh files in the constant directory in order to avoid any errors.

Second, the utility *decomposePar* is called to break the computational grid into the specified number of subdomains (16) in the dictionary file *decomposeParDict*. Finally, the command for parallel computing is called as follows:

```
mpirun -np 16 interFoam -parallel > log &
```

3.4 Surface Evolver Methodology

Surface Evolver is a free computational tool developed by Dr. K. A. Brakke which can be used to solve for free surface shapes[8]. A surface grid is generated by vertices, edges and triangular facets which is minimized using the gradient descent or other method. The initial surface annular grid is defined in a source file and the solutions for different volumes are computed until a plug is formed. One of the major benefits of surface evolver is its high fidelity in contact angle, critical in determining the shape and stability of free surfaces. Surface evolver has been used to for numerous studies to compute minimum energy solutions for different geometries [2, 37-39].

The user defines the topologies, geometric constraints, systems energies and volume [40]. The first constraint is the circular cylinder which confines the liquid applied at the both ends of the annulus (contact lines):

```
constraint 1
formula: X^2 + Y^2 = 1^2
```

The second step is to associate line integrals with the edges on constraints to account for energy. At the top end, the constraint as follows:

```
constraint 2
formula: X^2 + Y^2 = 1^2
energy:
```

```
e1: cos(10*pi/180)*1*z/(x^2+y^2)*y
e2: -cos(10*pi/180)*1*z/(x^2+y^2)*x
e3: 0
```

At the bottom edge, the constraint is applied as:

Constraint 1

formula: $X^2 + Y^2 = 1^2$

energy:

```
e1: -cos(10*pi/180)*1*z/(x^2+y^2)*y
e2: cos(10*pi/180)*1*z/(x^2+y^2)*x
e3: 0
```

Vertices are joined to form edges and edges are combined to define the surfaces. The surfaces are then associated to form bodies which allow for target volumes to be implemented at the end of the source file as follows:

body

1 (oriented surfaces) volume (target volume, e.g. 2, 4 etc)

density 0

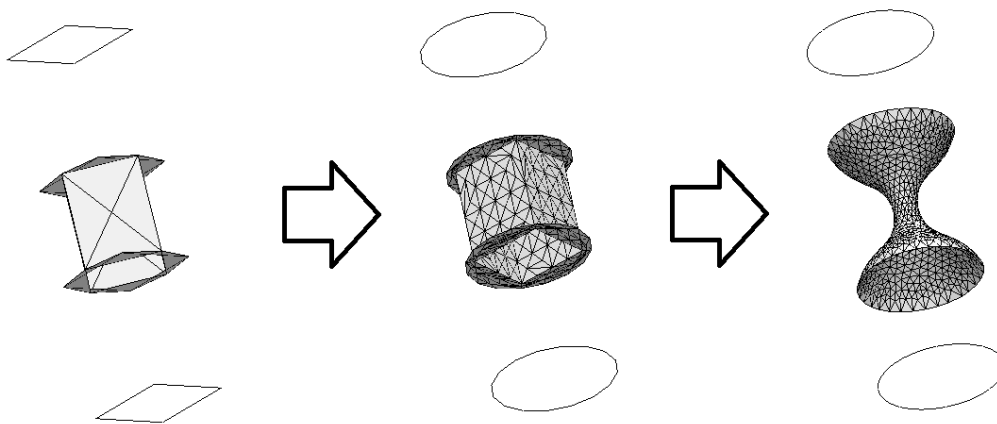


Figure 17. Energy minimization outcome

3.5 Grid Independence Study

Before simulation results can be analyzed and studied further, a grid independence study must be performed to determine optimum grid cell sizes. Course grids can result in large round-off errors and grids that are too fine may render computations prohibitively expensive. Pressure and velocity were used as the varying property to peruse grid dependence. The simulation was then run for various number of grid nodes for the same period of time ($t = 0.01$ sec). The results were collected at the same location for all cases – cross-section 1mm from the inlet. Results of the study are presented in Table 3.

Table 3

Summary of Grid Independence Results

Case number	Number of Nodes	Maximum Velocity (m/s)	Minimum Pressure (Pa)	Maximum Pressure (Pa)	Minimum-to-maximum pressure ratio	Cell Volume Range ($\times 10^{-15} m^3$)
1	12,541	0.40	127,057	128,294	0.9903	
2	43,323	0.36	130,116	131,398	0.9902	
3	60,388	0.33	133,270	134,370	0.9918	
4	93,490	0.31	134,406	135,047	0.9952	
5	122,128	0.31	135,082	135,148	0.9995	0.552-24.1

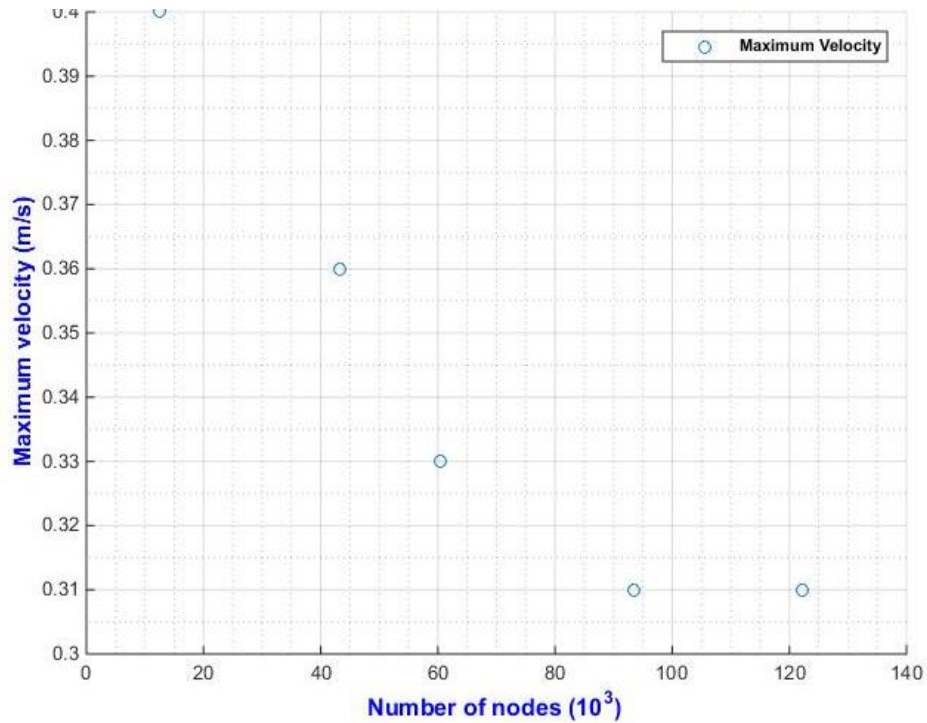


Figure 18. Graph of the maximum velocity at a cross-section 1mm from the inlet against number of grid nodes.

Figure 18 shows the maximum velocity reduces from 0.4 m/s at 12,541 nodes and converges to 0.31 m/s at 93,490 nodes. The maximum velocity not change in any significant manner as the number of nodes is increased beyond that point. This is an indication that any reduction in mesh size after the 93,490 nodes mark, does not affect the maximum velocity solution. The maximum velocity is as important parameter in this thesis, since it is used to normalize computation results. Apart from the maximum velocity, another interesting parameter to be examined in relation to increase in the number of nodes is the pressure field at the same cross-section. Figures 19 and 20 illustrate the behavior of the maximum and minimum pressure as the number of nodes is also increased.

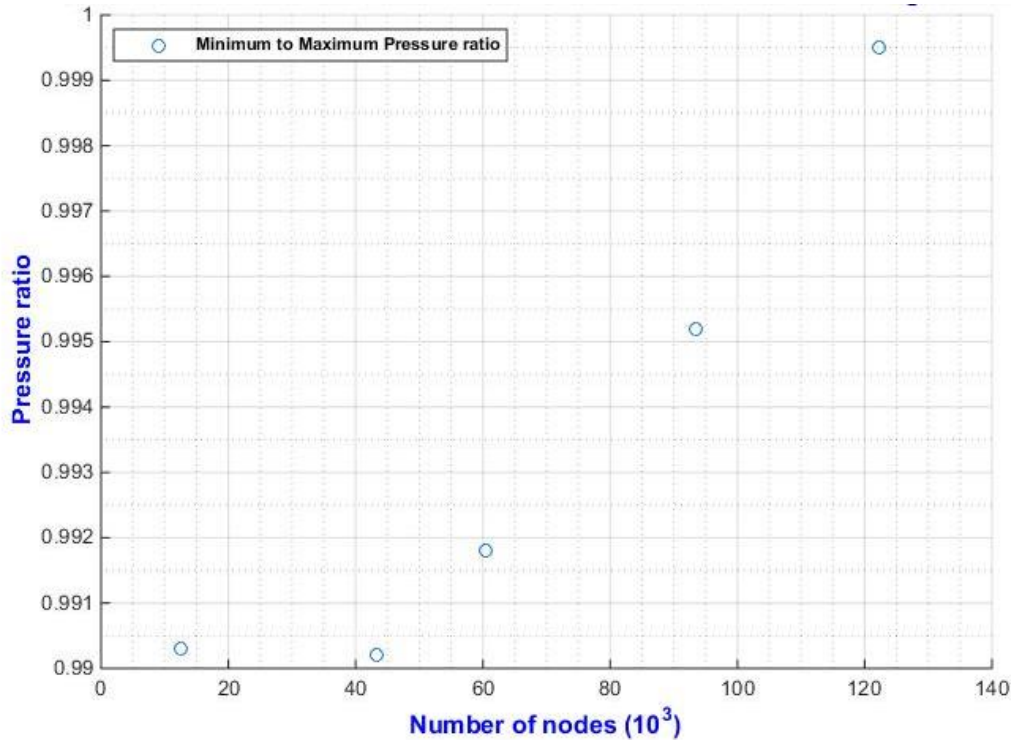


Figure 19. Minimum to maximum pressure ration at cross-section

The maximum and minimum pressures rise exponentially as the number of nodes is increased. Both quantities seem to converge at a value slightly greater than 135 kPa. At this point, the pressure field has approached uniformity across the cross-section. It is expected that the pressure distribution would be close to uniform due to its proximity to the inlet where pressure is applied uniformly. This is an indication that the pressure field solution is grid independent after 122,128 nodes. In figure 19, the values of the maximum and minimum pressure are compared by plotting the ratios of minimum to maximum pressure for the 5 cases presented in table. It is apparent the values are close – minimum pressure is 0.994 the value of the maximum pressure. These results suggest that the volume cell size range corresponding to 122,128 nodes would be the best fit for the simulations. In other words, the solutions are grid independent beyond 122,128 nodes.

In figure 21, the acceptable range of cell volumes corresponding to 122,128 nodes is shown to be between $5.52 \times 10^{-16} \text{ m}^3$ and $2.41 \times 10^{-14} \text{ m}^3$. Using this range as a guide, a new geometry with a smaller number of nodes and comprising cell volumes as above was created to reduce computation cost. The final mesh is shown in figure 4.0.

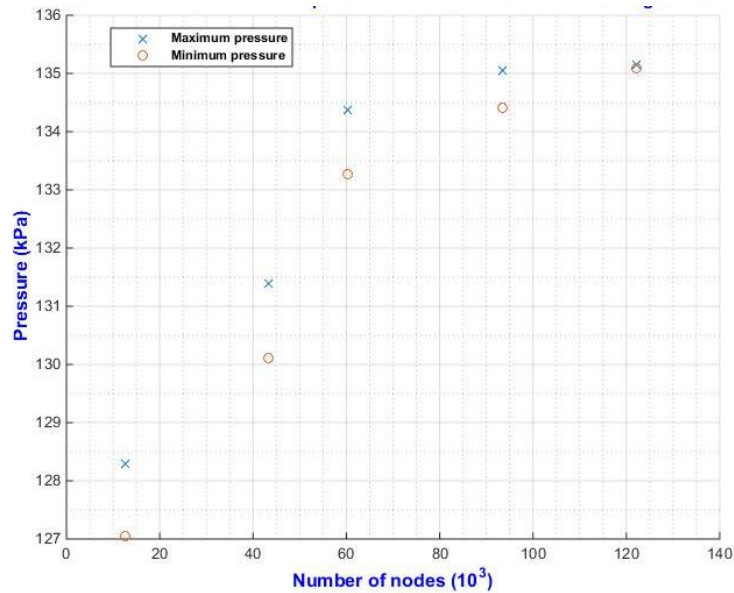


Figure 20. Minimum and maximum pressure at cross-section

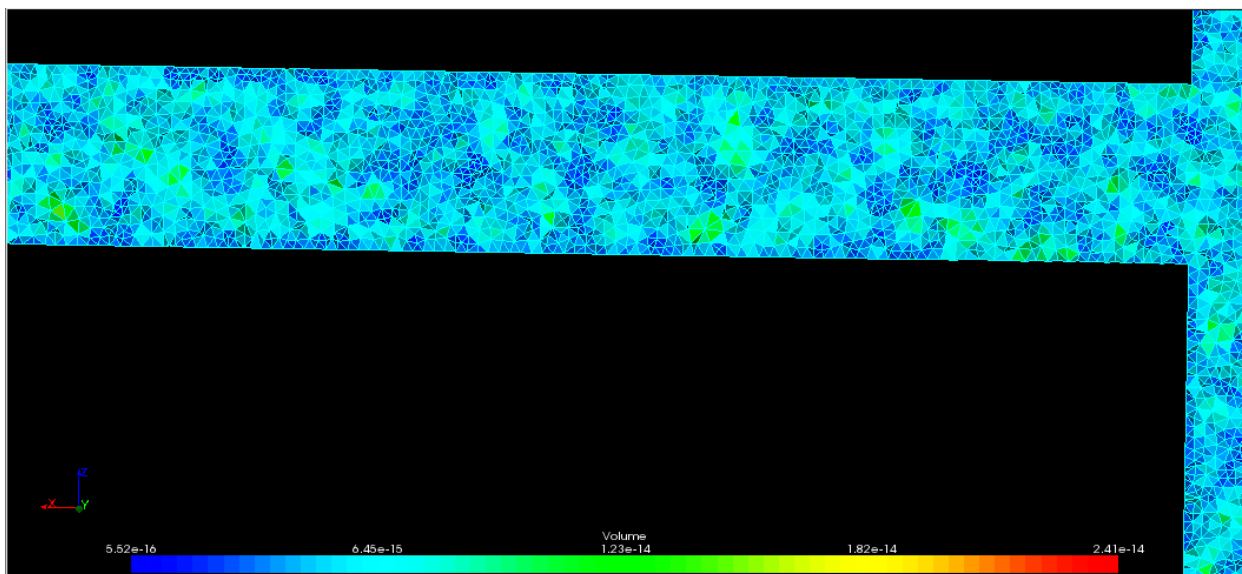


Figure 21. Grid volume size range

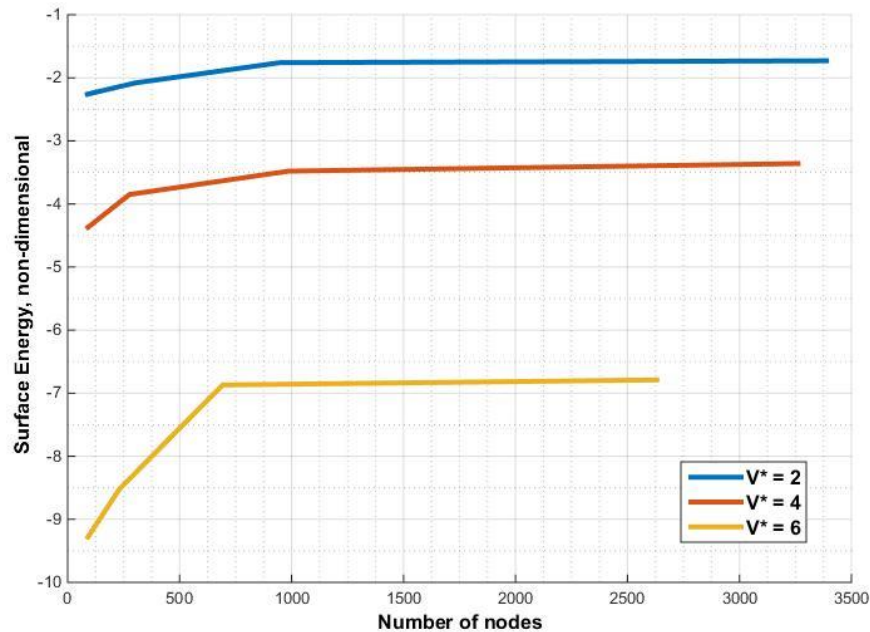


Figure 22. Grid independence (Surface Evolver)

Figure 22 shows that grid independence study. Surface Evolver code is run for three volumes – 2, 4 and 6 – until energy convergence is reached for different number of nodes. Grid independence is reached at above a 1000 nodes. Hence, minimum energy shapes were generated using a grid with 1000 nodes.

3.6 Experimental Technique

To verify the capabilities of OpenFOAM to simulate the topologies of the free surface in the dynamic system, an experiment was carried out to monitor the evolution of the free surface of with time in a circular cylinder. The liquid is injected via a side tube or circular cylinder which forms a T-section with the main circular cylinder filled with air. The liquid is injected until the plug is formed and the free surface assumes an unchanging curvature (until plug formation). The process of free surface evolution is recorded twice using a camera of high resolution – the experiment is repeated for the same conditions. During the first experiment, the camera lens is oriented to view the T-section from the side of the main circular cylinder, parallel

to the main cylinder axis (side view). The second experiment is viewed from the top where the camera lens plane is oriented perpendicular to the main cylinder axis. Figures 23 illustrates the differences in views.

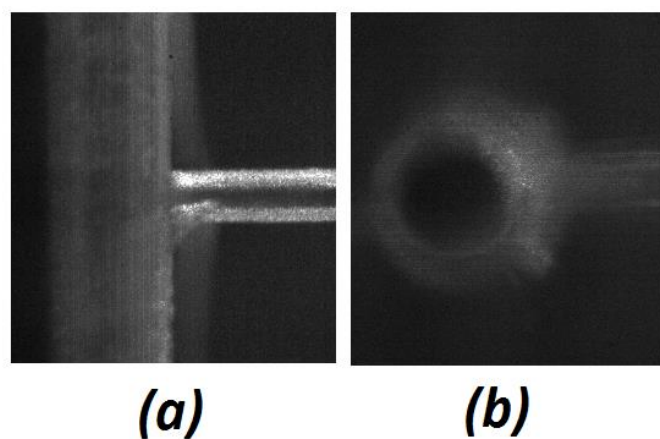


Figure 23. Resulting views of the two experiments, (a) Side view, (b) Top view

3.6.1 Experimental Apparatus and Setup

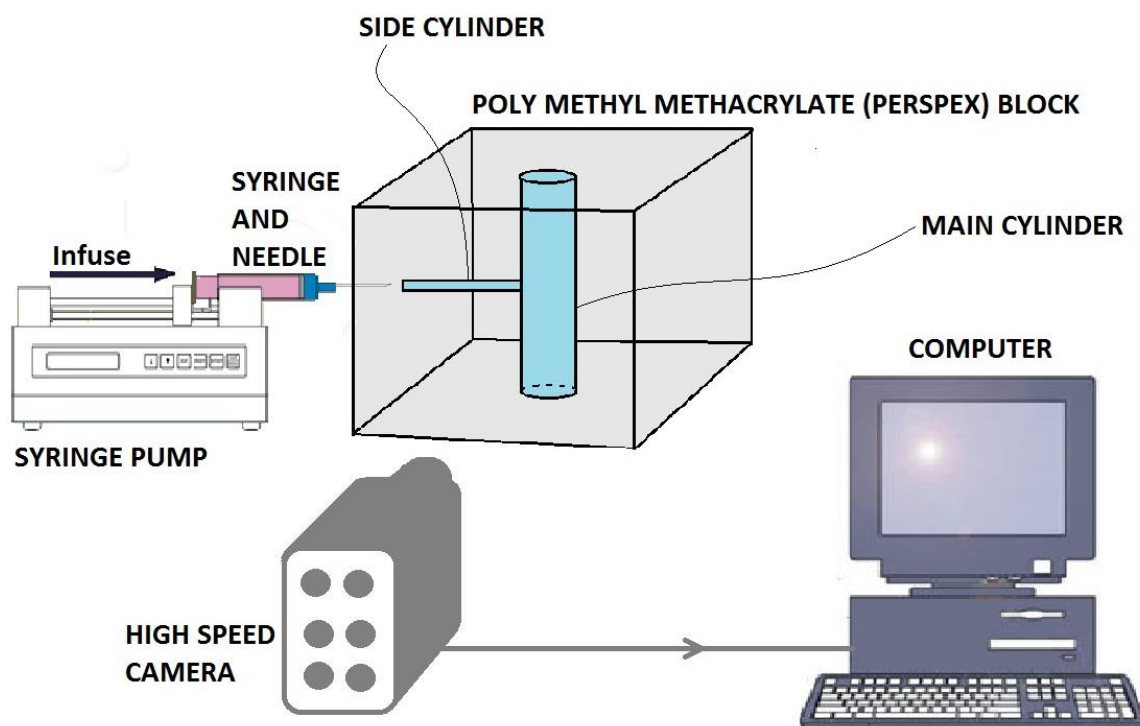


Figure 24. Schematic showing the apparatus and setup of two phase experiment

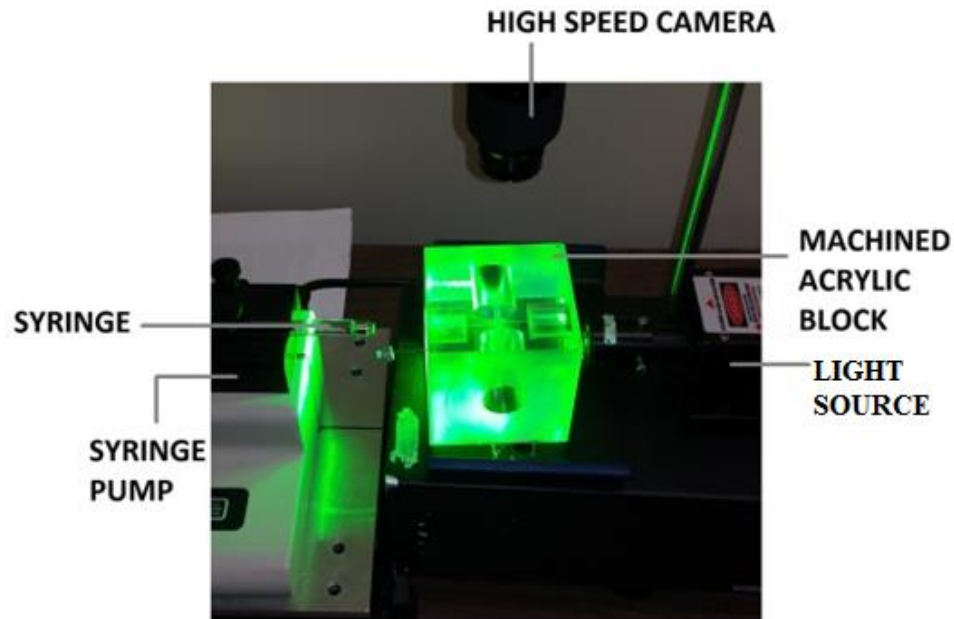


Figure 25. Experimental apparatus and setup

The experimental setup for this test case consists of two circular hollow holes drilled through a 73mm x 73mm acrylic block (shown in figure 27) forming a T-section through which silicon oil is allowed to flow freely (figures 24 and 25). A syringe pump is used to steadily inject the Newtonian liquid in a syringe via the side cylinder into the main cylinder. The high speed camera is connected to a computer which is used for monitoring and recording purposes. Silicone oil was chosen for this test for its numerous desirable characteristics including low thermal conductivity, low chemical reactivity, low toxicity, high wettability, low contact angles and high resistance to contamination [41]. Acrylic glass or Poly (methyl methacrylate) (PMMA) is a shatter-resistant, transparent thermoplastic selected for this experiment for its favorable machinability [42].

The dimensions of the hollow cylinders were restricted by the machining limitations and a low bond number requirement. Under terrestrial conditions the effects of gravity cannot be eliminated but surface tension effects can be made dominant by making the bond number as

smaller than 1 as possible. The smallest drill size capable of machining the acrylic block without breaking was found to be 0.5mm used to create the side cylinder; this translates to an acceptable bond number of 0.12. Using a 1mm diameter drill, the main cylinder was created with an operating bond number of roughly 0.47 (figure 26).

The measurement data consists of time history of interface orientation and shape; and volume of fluid in the main cylinder. The data was stored in the form of TIF image files captured at a rate of 158 images per second and 187 images per second for side and top views, respectively. The images were then analyzed using image J, an image processing tool [43], to determine injection flow velocity as accurately as possible. Using dimensions, the material properties of silicone oil and the measured initial flow velocity, the volume of fluid in the main cylinder was calculated and recorded.

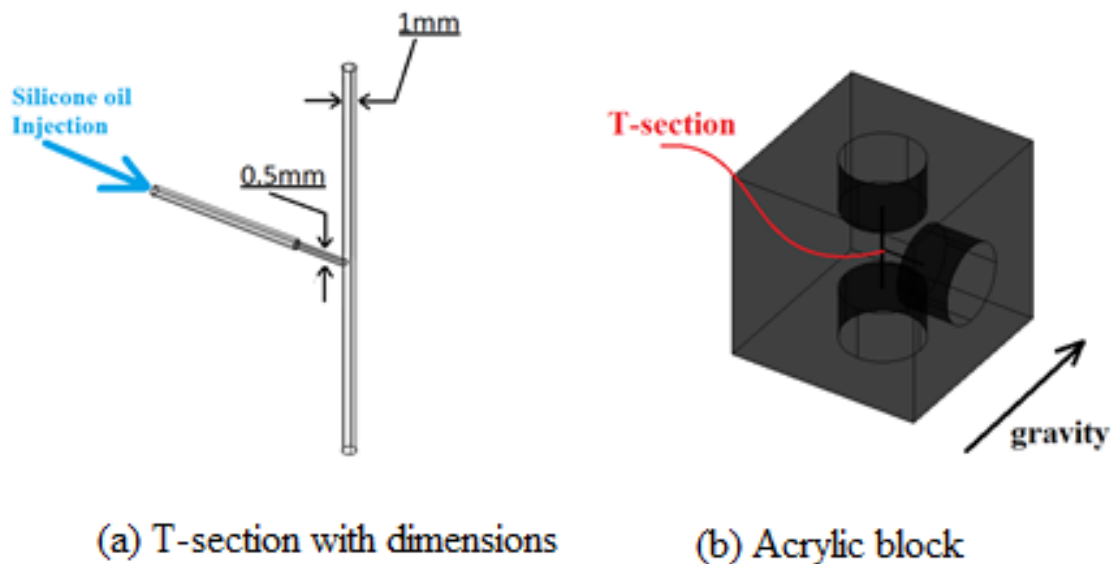


Figure 26. Schematic of acrylic block showing location and orientation of T-section, and direction of gravitational force (a) T-section with dimensions (b) 73mm x 73mm acrylic block

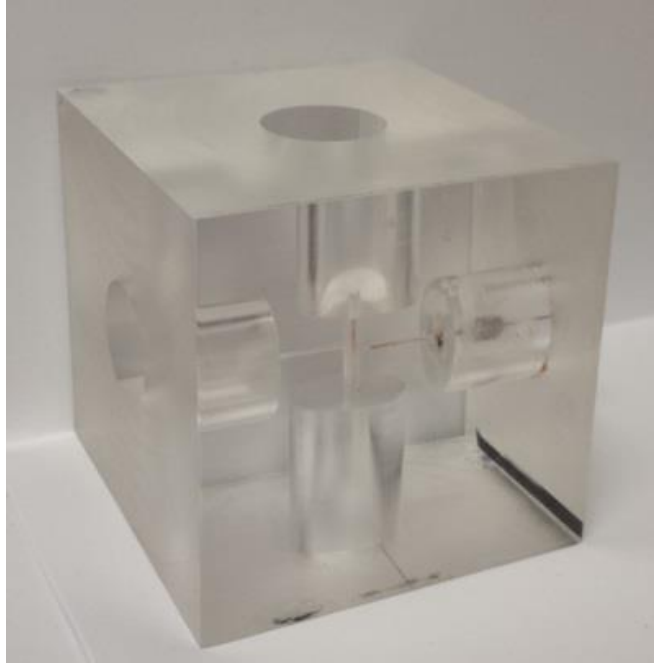


Figure 27. Acrylic block with machined T-section (finished product)

CHAPTER 4

Results

4.1 Experimental Results

Table 4 depicts the time-dependent evolution of the interface of silicone oil injected into an air-filled circular cylinder. Initially, silicone oil fills the cylinder along the circumference forming a droplet until it converges on the other side and forms an annulus. As the volume increases, the annulus curvature increases until, at some point, the interface joins at the center and transforms into a plug (at 2.335 seconds). The plug continues to increase in volume and length in the lateral direction along the axis of the cylinder.

The experiment is carried out in two parts. One is carried out while the oil is monitored from the side (table 4) at a right angle to the T-section and other is carried out while monitoring the silicone interface from the top (table 5) along the axial direction.

Table 4

Side views of evolving silicone oil interface

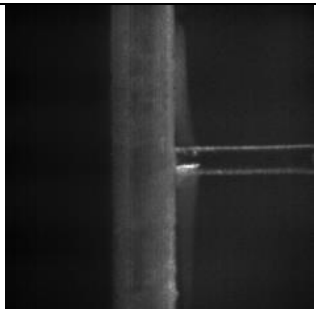
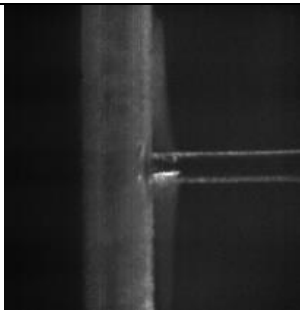
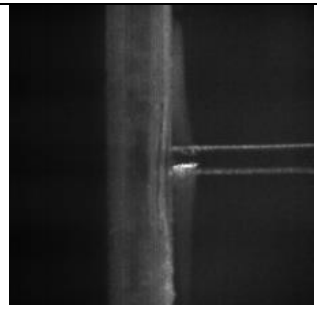
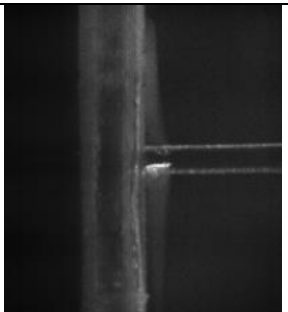
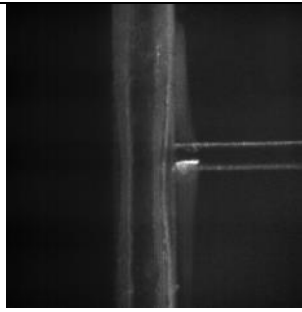
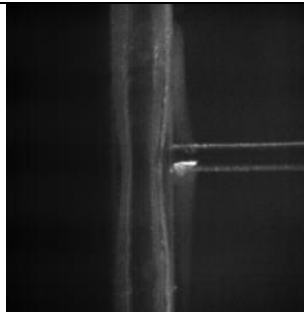
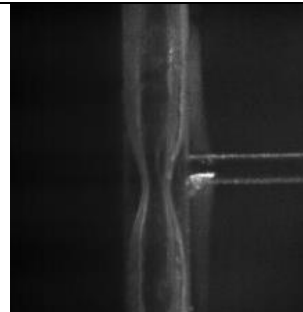
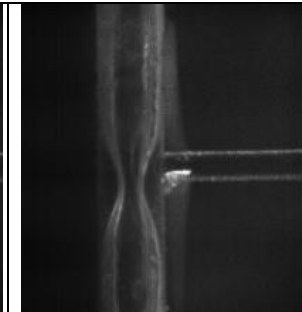
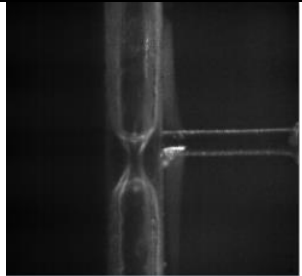
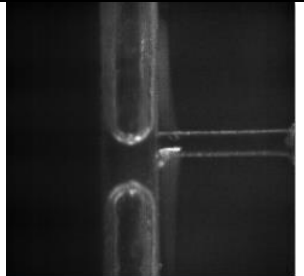
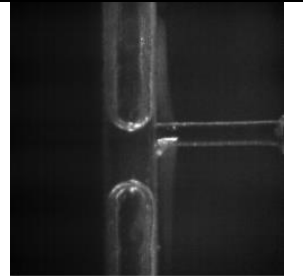
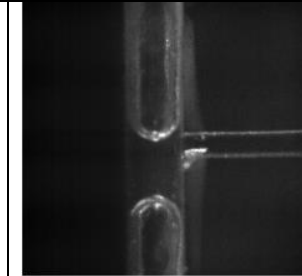
			
Frame 208 Time: 0 sec	Frame 209 Time: 0.0063sec	Frame 254 Time: 0.2911sec	Frame 336 Time: 0.8101sec

Table 4

Cont.

			
Frame 506 Time: 1.8861 sec	Frame 546 Time: 2.1329 sec	Frame 575 Time: 2.3228 sec	Frame 576 Time: 2.3239 sec
			
Frame 577 Time: 2.3354 sec	Frame 578 Time: 2.3418 sec	Frame 618 Time: 2.5949 sec	Frame 622 Time: 2.6203 sec

The change in shape from the annulus to plug occurs at a rapid rate. When the annulus neck is roughly 20% of the cylinder diameter, the plug interface is formed on both ends of the annulus after which form a hollow enclosure which defines the shape of the plug. The hollow enclosure is then filled with silicone oil and a plug is formed. The process results in roughly a 40% reduction in the column length and takes less than 0.006 seconds to transform from annulus to plug.

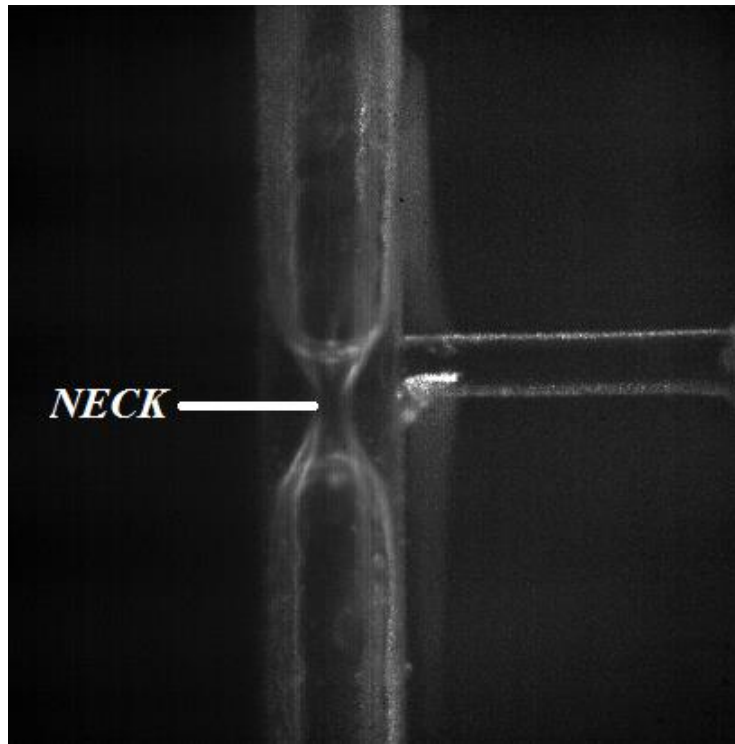


Figure 28. Neck of Annulus-Plug Topology

In order to calculate the volume of silicone oil in the main cylinder, the fluid is injected at a constant rate. Figures 29 to 32 are plots of the interface position with time of silicone oil in the side tube. It shows that silicone oil enters the circular cylinder at approximately a constant rate of 2.9 mm/s.

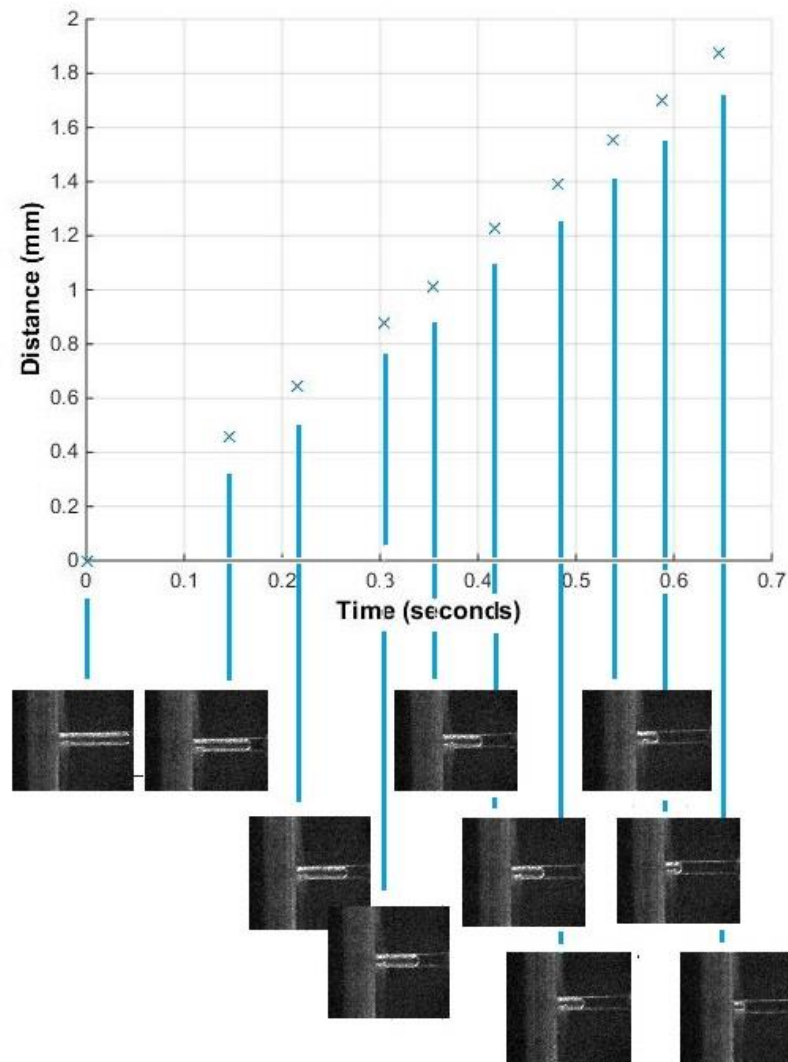


Figure 29. Plot of progression of silicone oil interface with time

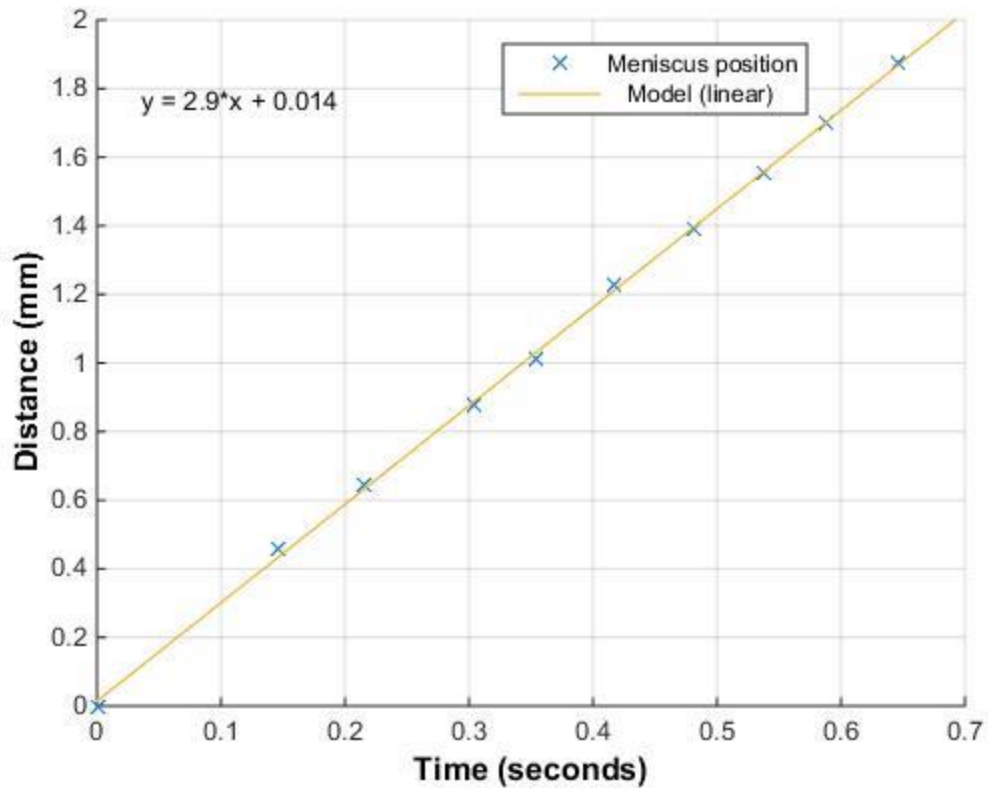







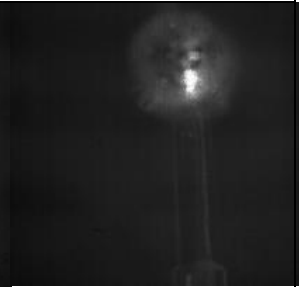


Figure 30. Linear model of injection velocity

Table 5 presents results of the second experiment where the interface is monitored from the top. It is obvious the silicone oil travels along the circumference of the cylinder and forms a ‘doughnut’ shapes. As the volume increases, the interface converges at the center and a plug is formed at approximately 2.29 seconds.

Table 5

Top views of evolving silicone oil interface

			
Frame 269 Time: 1.067 sec	Frame 295 Time: 1.209 sec	Frame 493 Time: 2.267 sec	Frame 497 Time: 2.288 sec
			
Frame 498 Time: 2.294 sec	Frame 499 Time: 2.299 sec	Frame 500 Time: 2.304 sec	Frame 515 Time: 2.385 sec

Silicone oil is injected at a constant rate as was the case with experiment one. Figures 28 and 29 indicate that the injection velocity is roughly 3.2mm/s. The time-dependent volume is then calculated using the velocity and cross-section of the side cylinder.

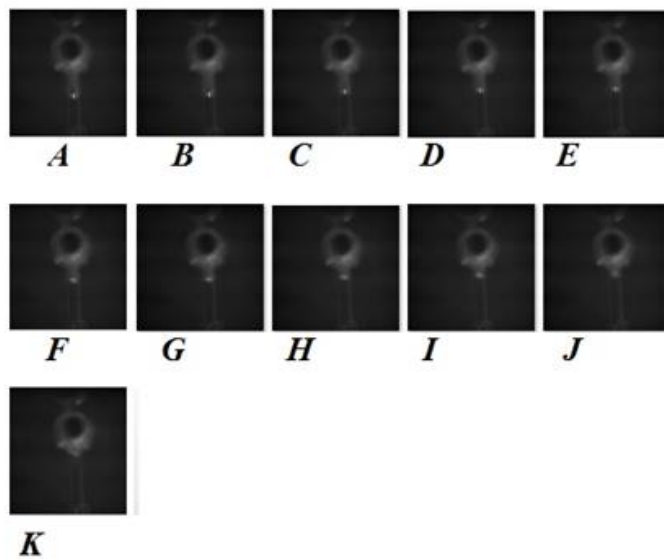
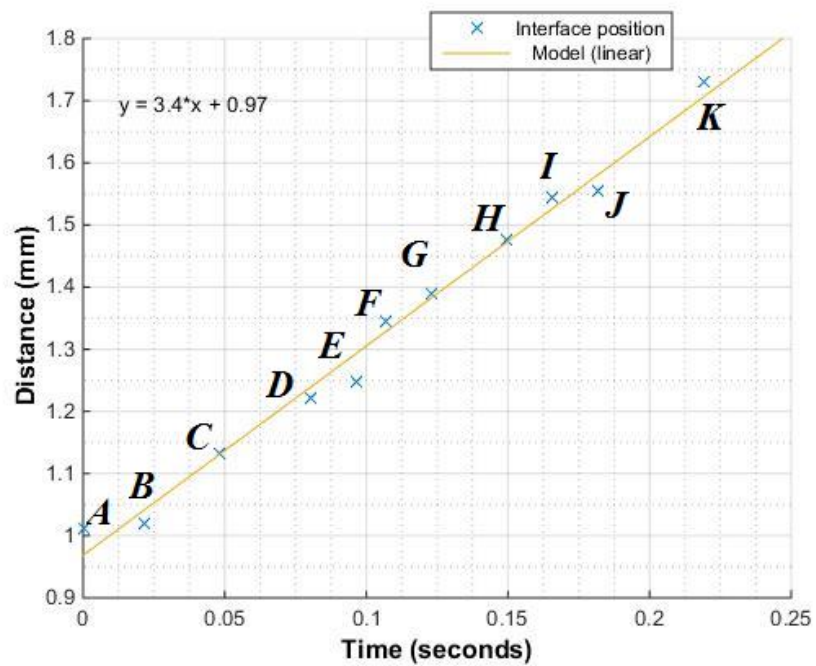


Figure 31. Plot of progression of silicone oil interface with time

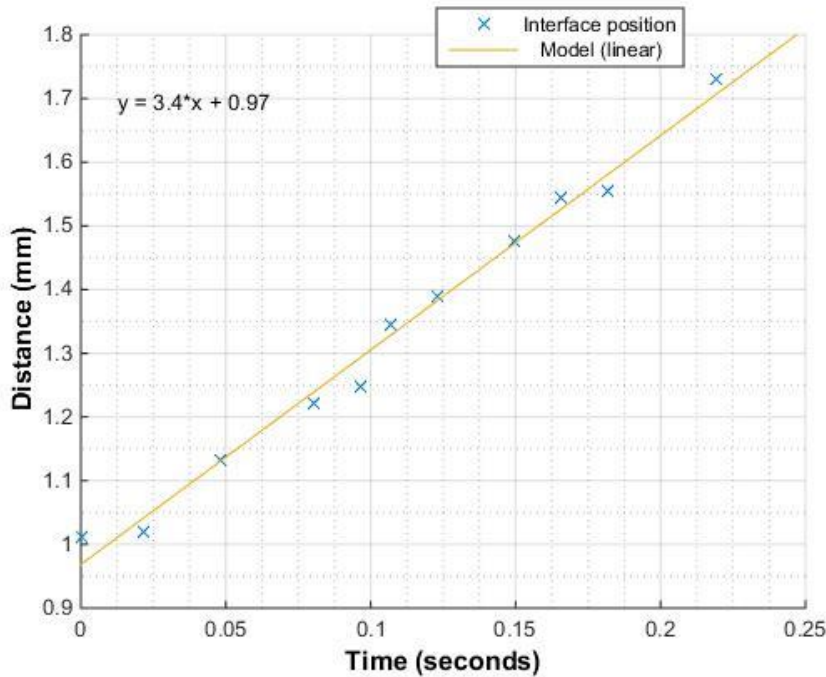


Figure 32. Linear model of injection velocity

Figure 33 is a plot of volume versus time for the two experiments. As expected, the plots have different gradients due to the differences in flow rate. The plug forms at different times, and hence, different volumes. The plug was formed at approximately 1.33 mm^3 and 1.5 mm^3 for experiment 1 and 2, respectively. This suggests that the plug solution is a function of inlet conditions. Non-dimensionalizing the plot reveals the nature of these solutions in relation to the temporal and spatial scales of the system. The volume was non-dimensionalized with the cubic radius of the main circular cylinder and the time was non-dimensionalized using the main circular cylinder radius and the injection velocity. The plug occurs at approximate dimensionless volumes of 7.8 and 8.1 at a non-dimensional time of about 13 for experiments 1 and 2, respectively as seen in figure 34.

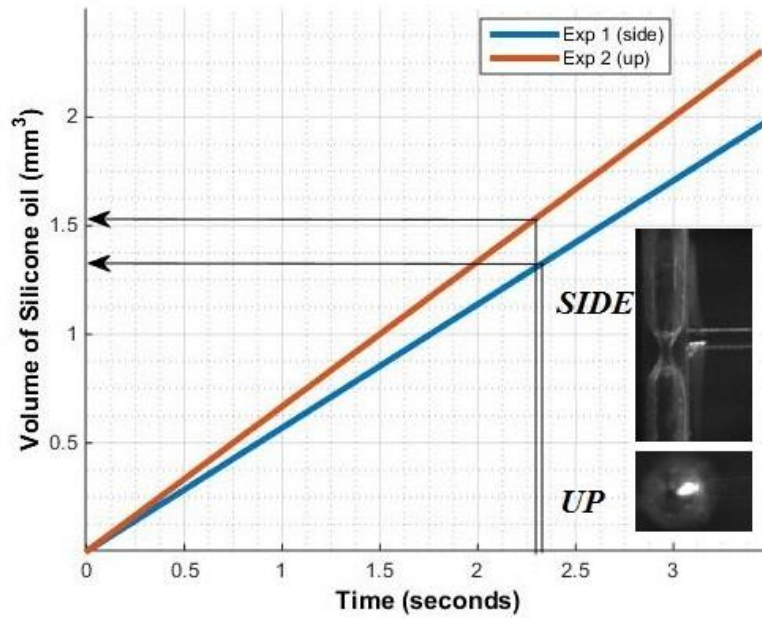


Figure 33. Plot of volume versus time for experiment 1 (side) and experiment 2 (up)

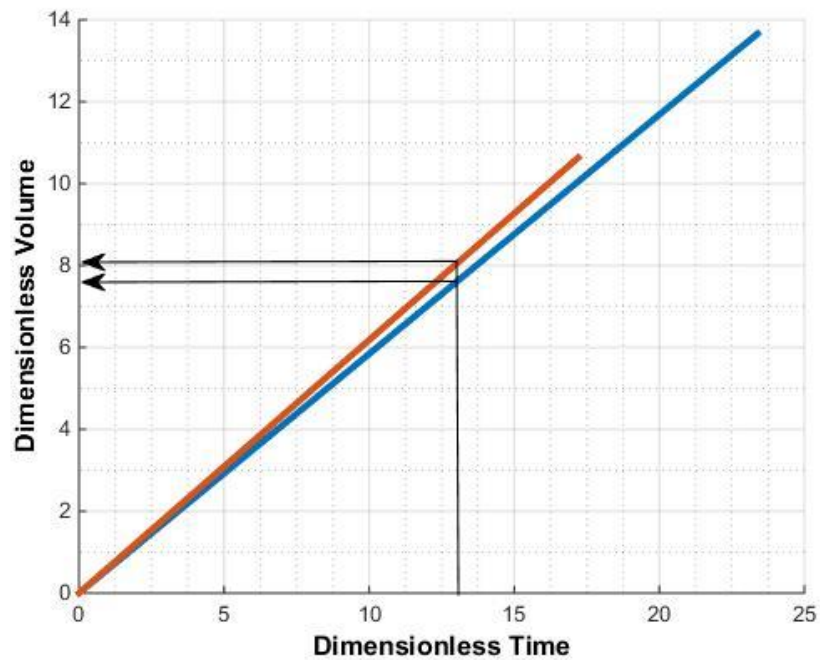


Figure 34. Plot of dimensionless volume versus dimensionless time for experiments 1(side) and 2(up).

The dimensionless flow rate ($\frac{V^*}{t^*}$) derived from figure 34 is approximately 0.58. This experimental value will be compared with the numerical one for validation purposes.

4.2 Numerical Results

The numerical simulation was carried out using a three-dimensional domain in real scale discretized with a non-orthogonal unstructured grid consisting of tetrahedral volume cells with a total of 81,570 nodes. The time step size used during simulation was set to $\Delta t = 1^{-9}s$ to make the maximal cell courant number smaller than 0.2. The constituent equations were solved using the following material properties for $\rho_2 = 1.00 \frac{kg}{m^3}$, $\gamma_1 = 1.48 \times 10^{-5} m^2/s$ air: and for silicone oil: $\rho_2 = 860 \frac{kg}{m^3}$, $\gamma_1 = 1.00 \times 10^{-6} m^2/s$. The gravitational term in the Navier-Stokes equation is neglected.

Tables 6, 7, 8, 9 and 10 present the side and top views of different applied pressures at the inlet in increments of 30 Pa: 0 Pa, 30 Pa, 60 Pa, 90 Pa and 120 Pa. The corresponding time for each shape is also provided. Time-dependent flow rate and volume plots are provided for each set of results for analysis purposes. The color red signifies silicone oil and blue is air.

Table 6

Numerical results for 0 Pa at the inlet

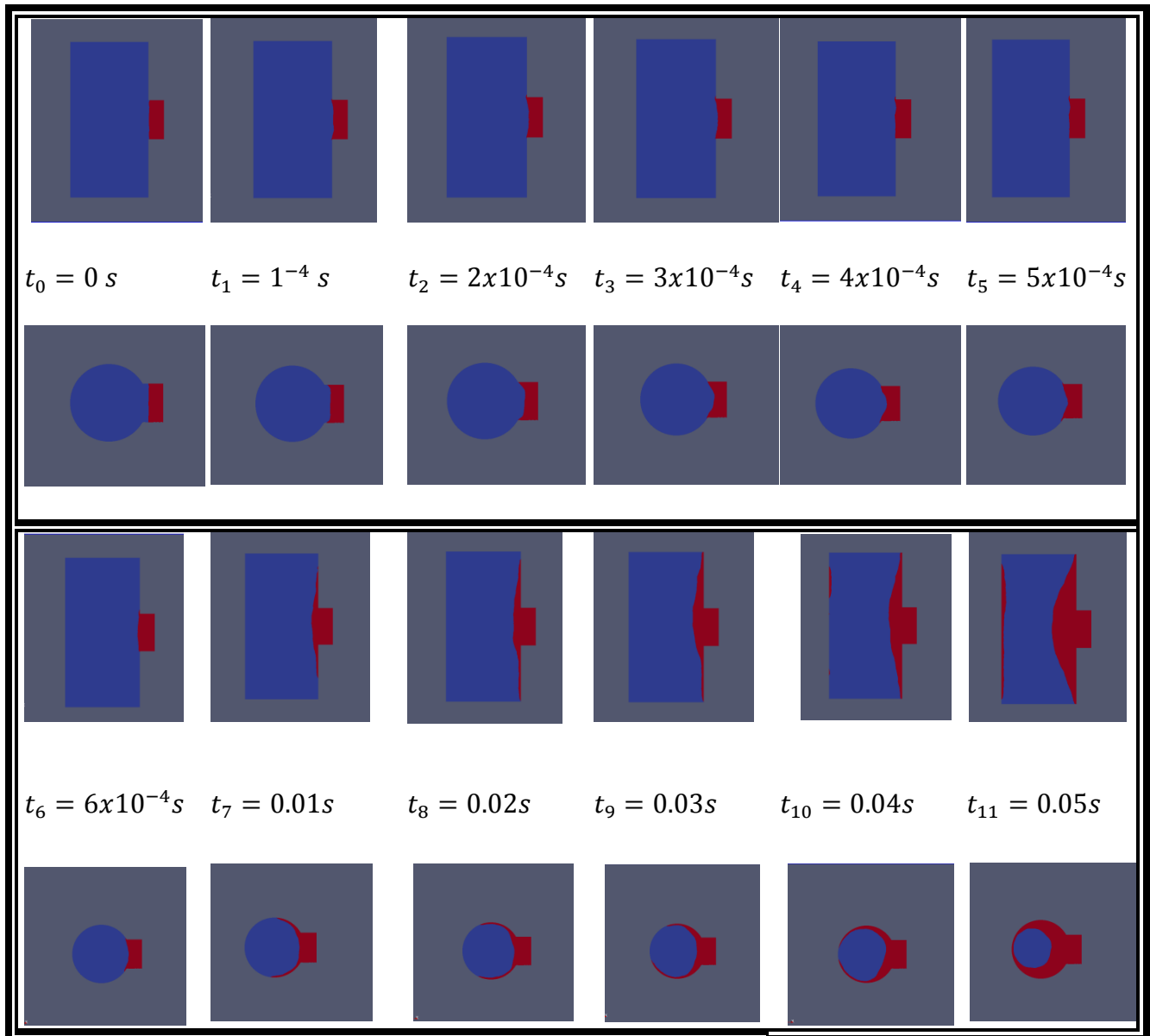


Table 6

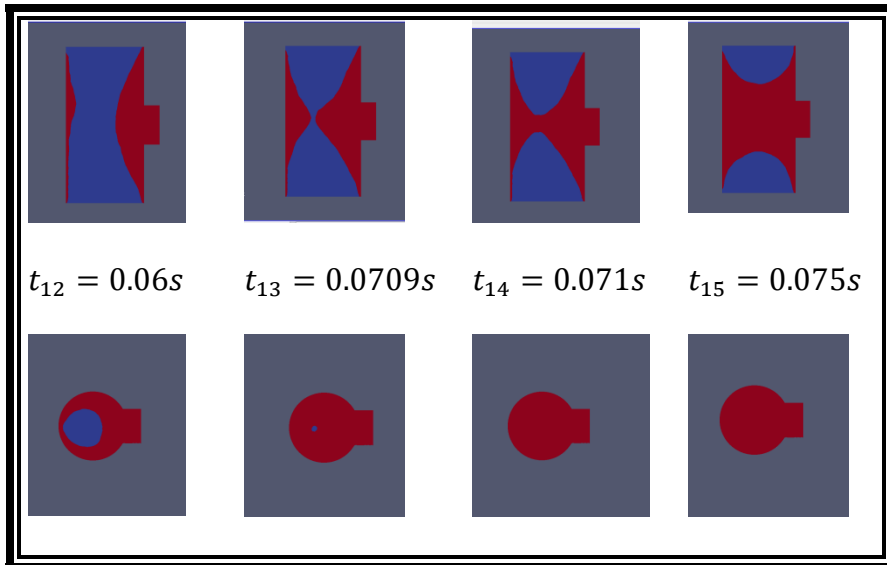
Cont.

Table 7

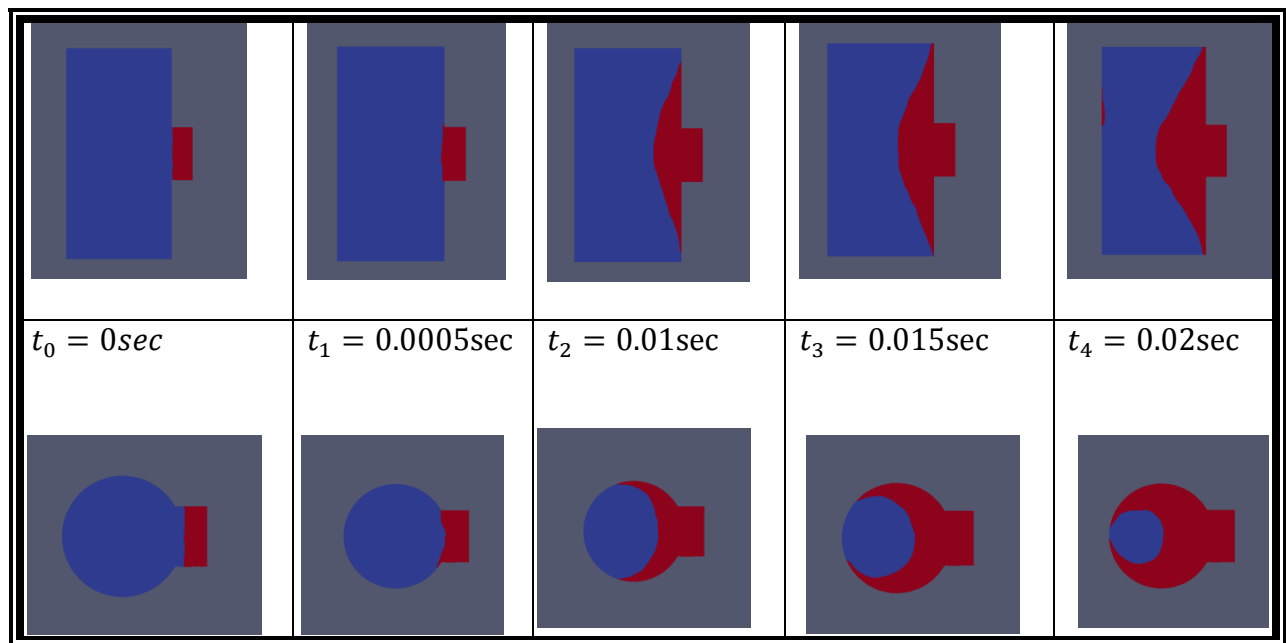
Numerical results for 30 Pa at the inlet

Table 7

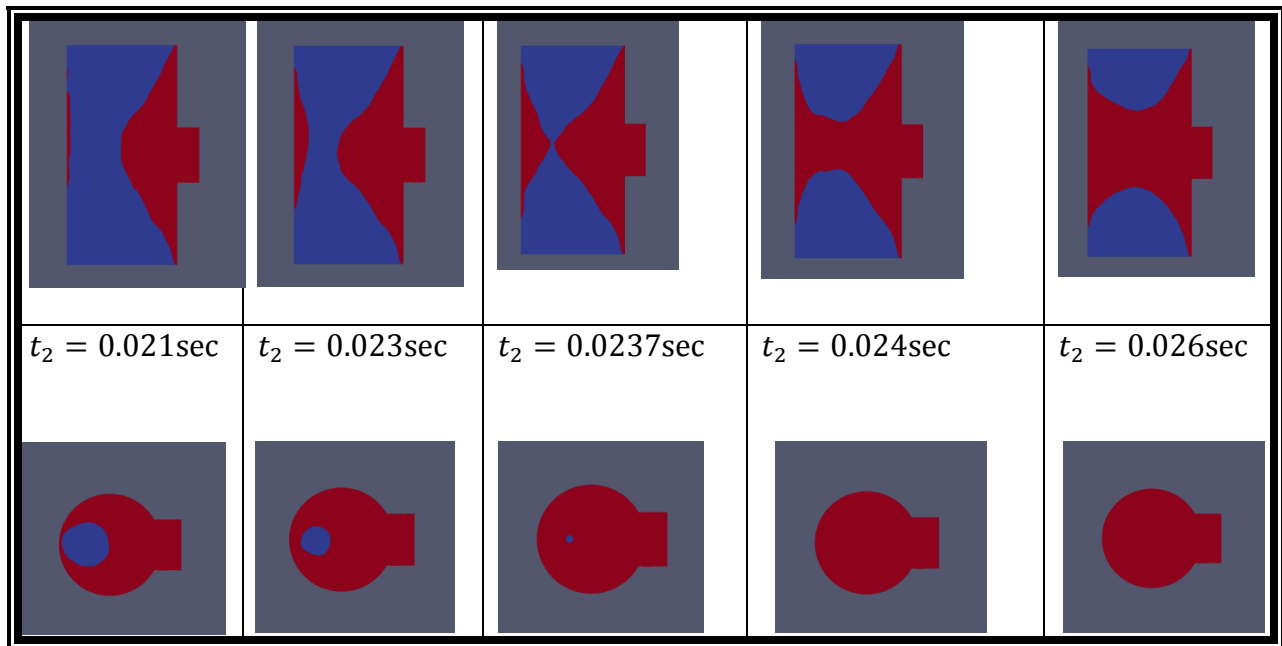
Cont.

Table 8

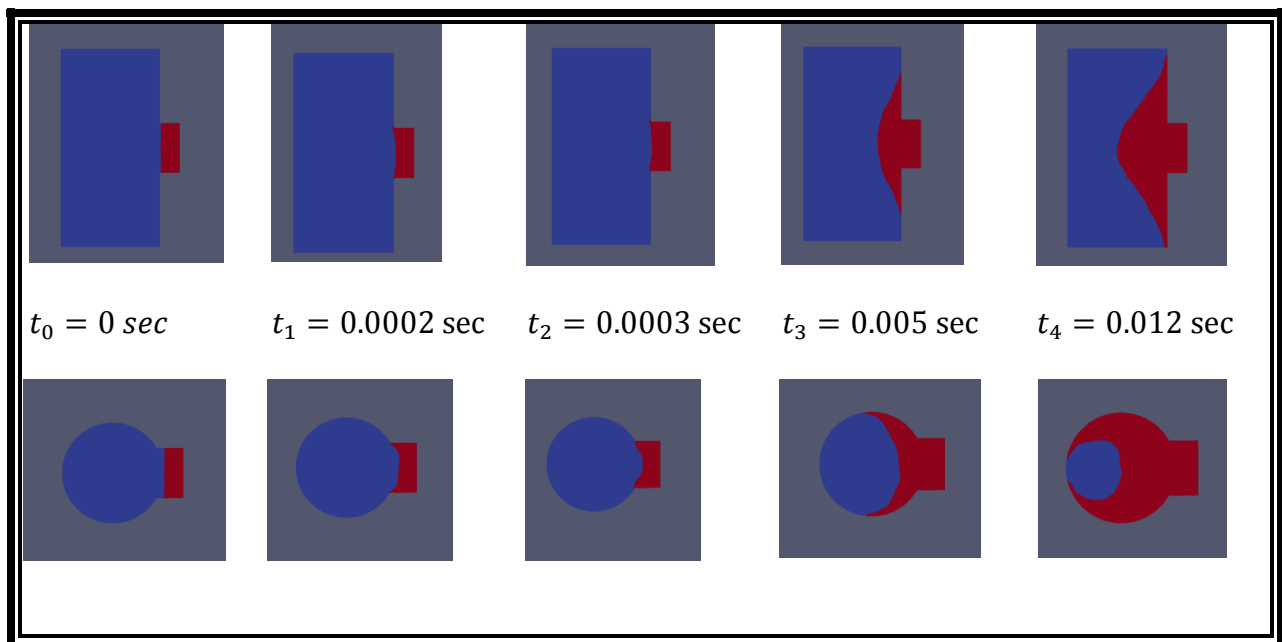
Numerical results for 60 Pa at the inlet

Table 8

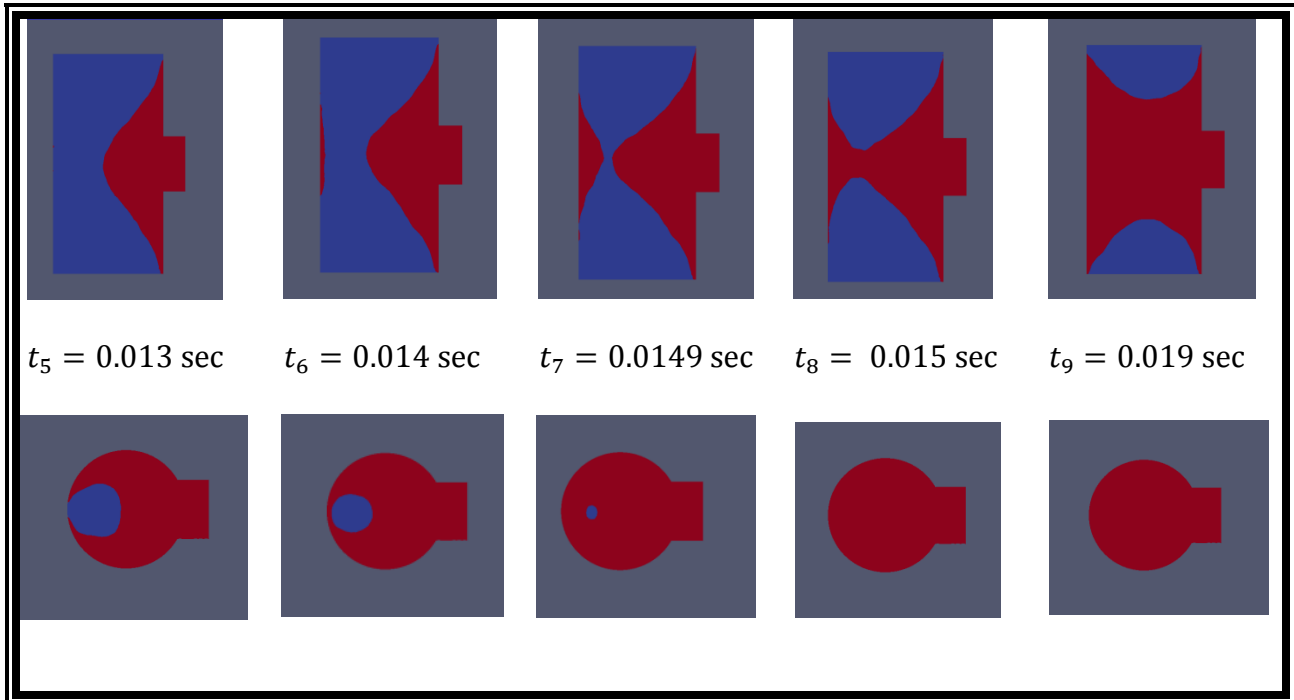
Cont.

Table 9

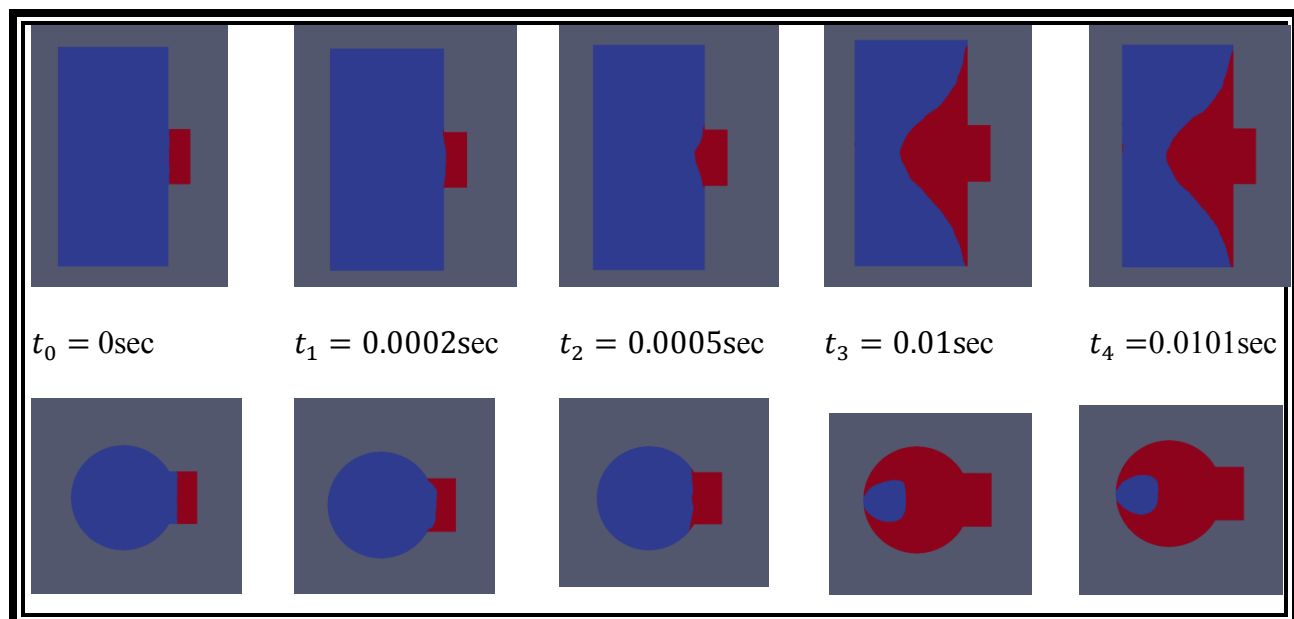
Numerical results for 90 Pa at the inlet

Table 9

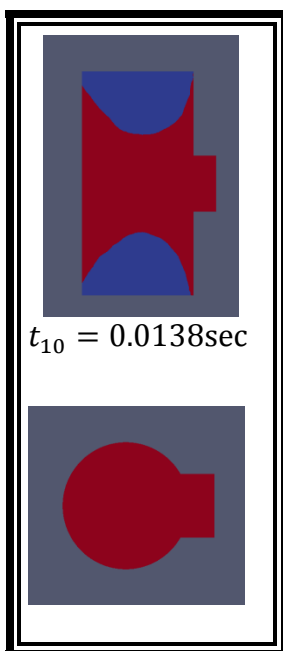
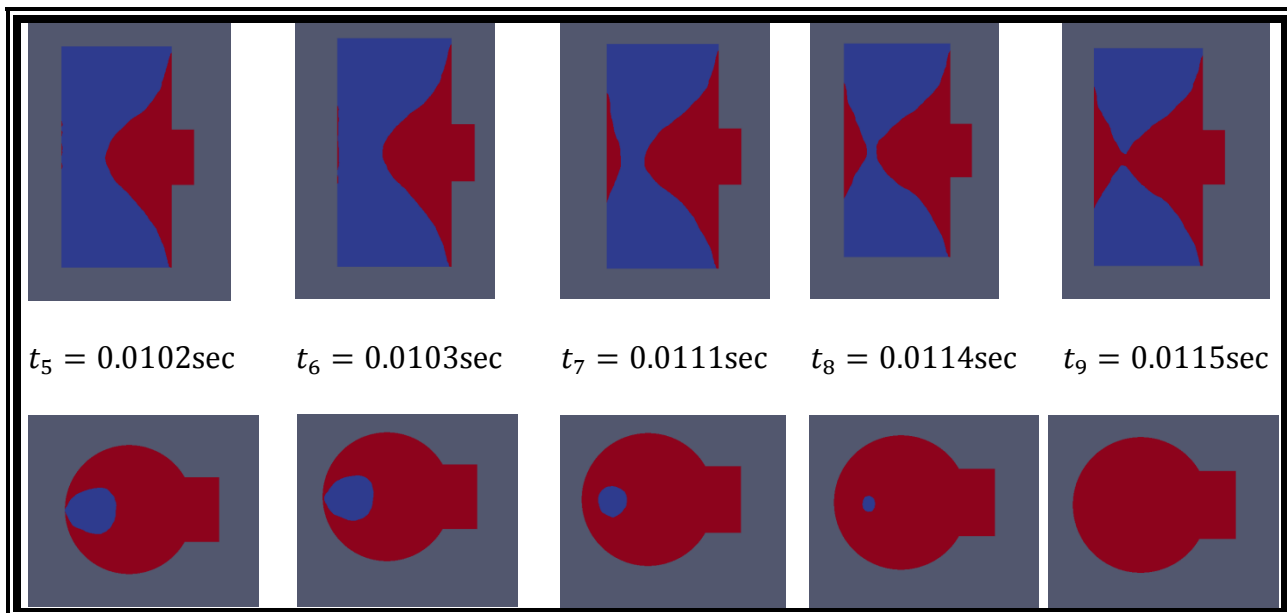
Cont.

Table 10

Numerical results for 120 Pa at the inlet

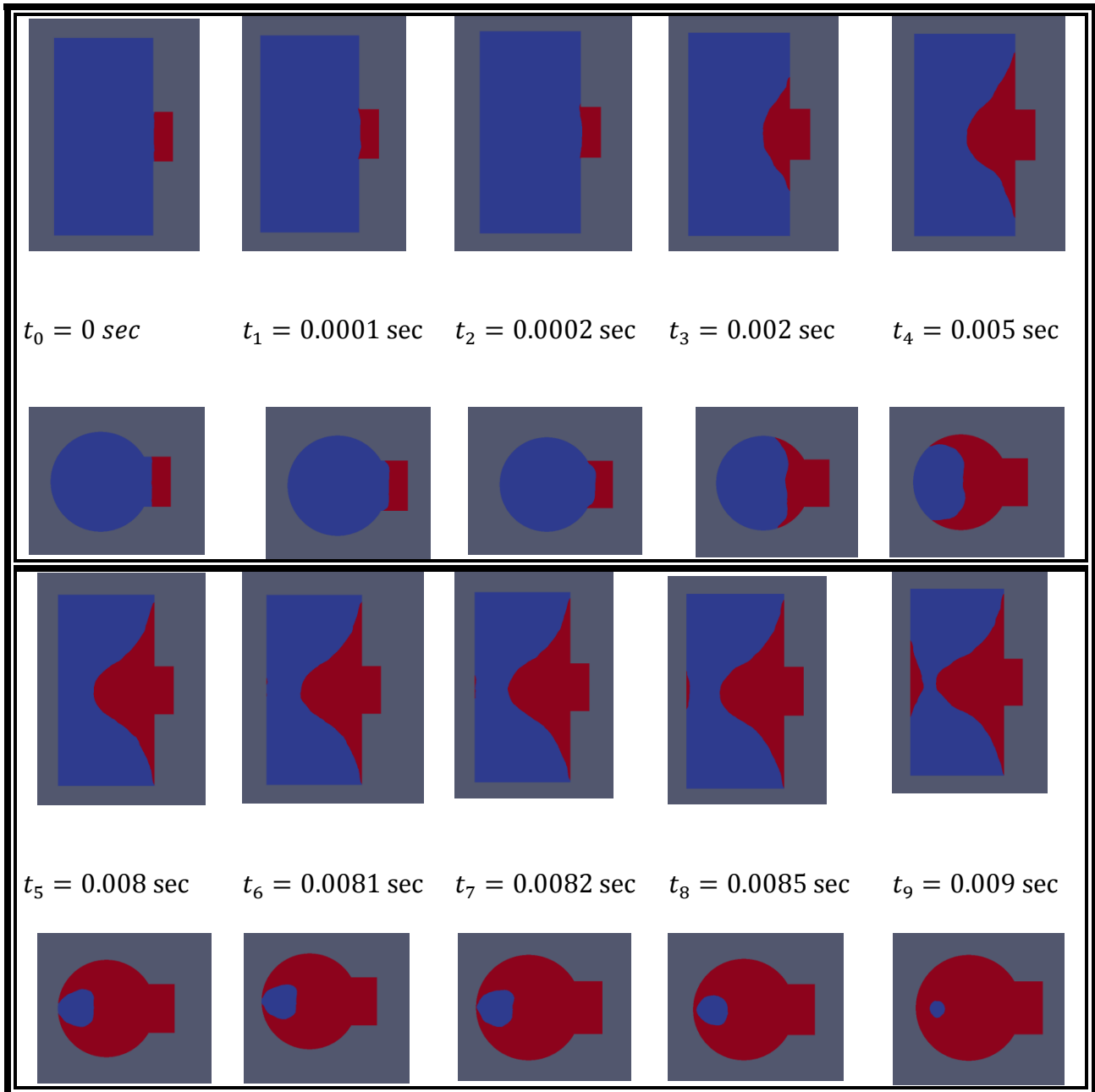
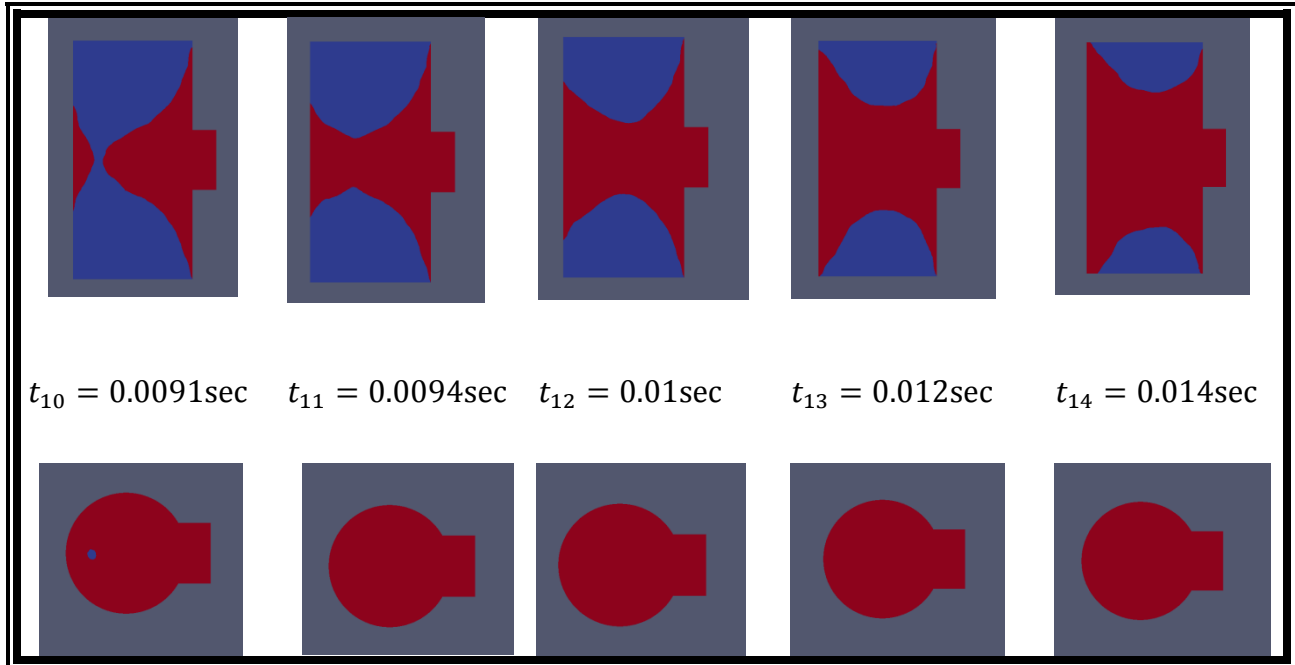


Table 10

Cont.

The simulation confirms the existence of three topologies: droplet, annulus and plug.

In the 0 pressure difference case, at 0 seconds, the interface is flat. As the simulation proceeds, the interface curves inward while the liquid continues to enter the main cylinder. The liquid fills the cylinder in both the axial and circumferential directions. The droplet exists until about 0.04 seconds, where the interface transforms into an annulus. At about 0.0709 seconds, the annulus snaps into a plug and continues to exist until the cylinder is completely filled. The scenario described for the 0 pressure difference case above applies to the other cases (30 Pa, 60 Pa, 90 Pa and 120 Pa).

4.2.1 Comparison of Numerical Results with Experimental Results

Numerical results of 0 Pa case is compared with experimental results at the point where the plug is formed. The corresponding non-dimensional times are also compared (Table 11).

Table 11

Comparison of numerical (0 Pa) and experimental results

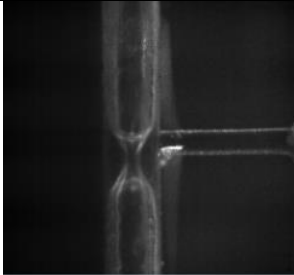

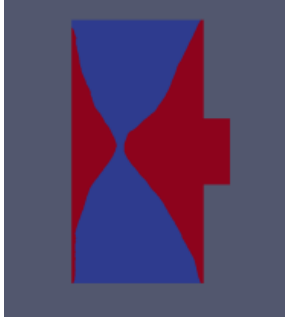

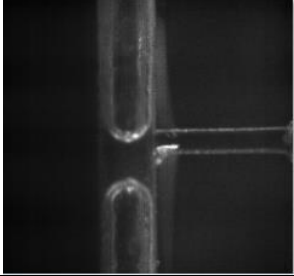

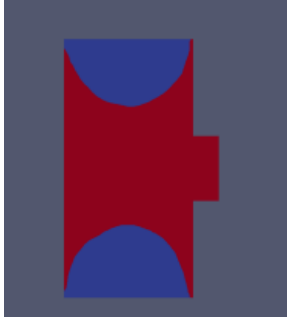

Data Type	Side	Top	Non-dimensional Time
Experiment			13.4
OpenFOAM			13.1
Experiment			13.6
OpenFOAM			13.8

Table 11 presents the interfaces (side and top views) at the points where plug formation just begins and after the plug has been fully formed. At the point just before plug formation the topology is in a transition phase from annulus to plug. The non-dimensional time at which this instability occurs is 13.4 for experiment and 13.1 for the simulation. The plug is fully formed at the non-dimensional times of 13.6 and 13.8 for experiment and simulation, respectively. This is favorable as simulation results are in close agreement to experiment. Due to this, the dynamics in this thesis will be studied using OpenFOAM.

4.2.2 Description of Transition Mechanism

Table 12 summarizes the points at which the droplet transforms into an annulus (Droplet-Annulus) and the annulus transforms into a plug (Annulus-Plug) for the cases studied in this thesis.

Table 12

Summary of topological transition points

Pressure Difference (Pa)	Droplet-Annulus		Annulus-Plug	
	Time(seconds)	Volume(mm^3)	Time(seconds)	Volume(mm^3)
0	0.0600	0.595	0.0709	0.863
30	0.0200	0.705	0.0237	0.888
60	0.0120	0.632	0.0149	0.830
90	0.0101	0.700	0.0114	0.814
120	0.0081	0.665	0.0091	0.764

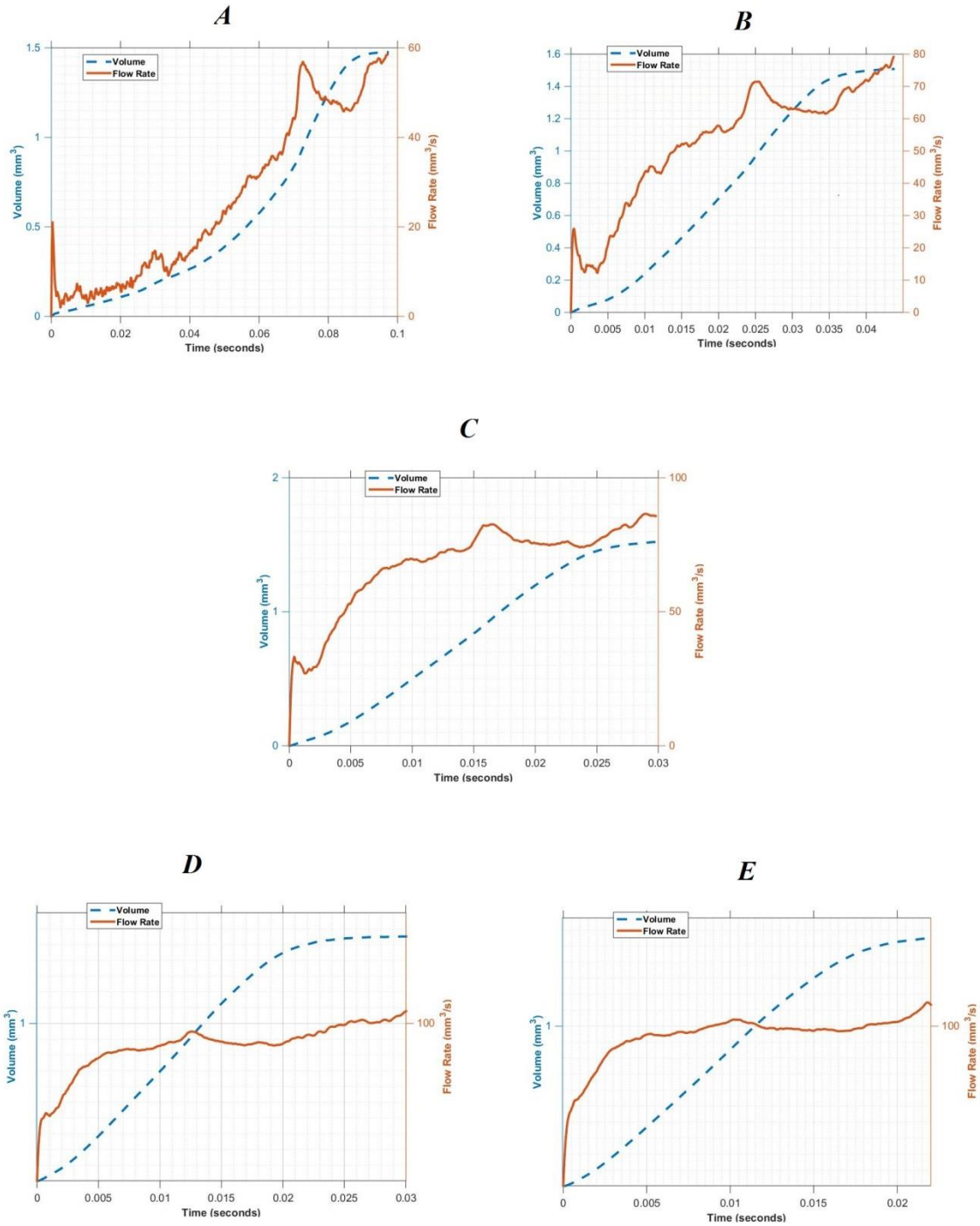


Figure 35. Plot of time-dependent flow rate and volume for different pressure differences:

A. 0 Pa; B. 30 Pa; C. 60 Pa; D. 90 Pa; and E. 120 Pa.

Figure 35 presents the plots of flow rate and volume versus time for various applied pressure differences. Plot A corresponds to the case without an applied pressure difference. The flow is capillary driven. The flow accelerates at the beginning of the process until about 0.0004 seconds when the flow rate drastically falls and then continues to rise gradually after approximately 0.0025 seconds; meanwhile the volume continues to increase gradually. The initial acceleration takes place as the interface curvature assumes a concave shape. The rapid reduction in the effective curvature radius during this process creates a jump in pressure difference that drives the flow; hence, a rise in flow rate. The flow rate reduces after an equilibrium shape has been reached that still generates sufficient pressure difference to drive the flow.

The sharp drop in flow rate between 0.0003 and 0.0026 seconds corresponds to the liquid flowing into the cylinder. The interface shape is a function of the surface tension, contact angle and the geometry of the container. As the liquid enters the container, the effective radius of curvature increases which causes a reduction in flow rate. As the volume in the container increases, the radius of curvature gradually reduces which causes the flow rate to gradually increase between 0.0025 and 0.0709 seconds. Between 0.0709 and 0.075 seconds, the annulus joins at the center and forms a plug.

The transition from annulus to plug occurs at a rapid rate indicated by the jump in flow rate. When the annulus joins at the center, the curvature radius instantaneously reduces which corresponds to an instantaneous rise in pressure difference at both ends of the liquid column. The flow rate reaches a maximum value and then reduces once an equilibrium shape has been

reached. After this point, the liquid column forming the plug continues to increase in length towards both ends of the container.

A similar scenario occurs for cases where pressure is applied at the inlet. However, for applied pressure cases, the flow rate increases exponentially, as shown in figure 36. Furthermore, the applied pressure cushions the reduction in pressure difference caused by the increased curvature radius that arises from the liquid entering the container.

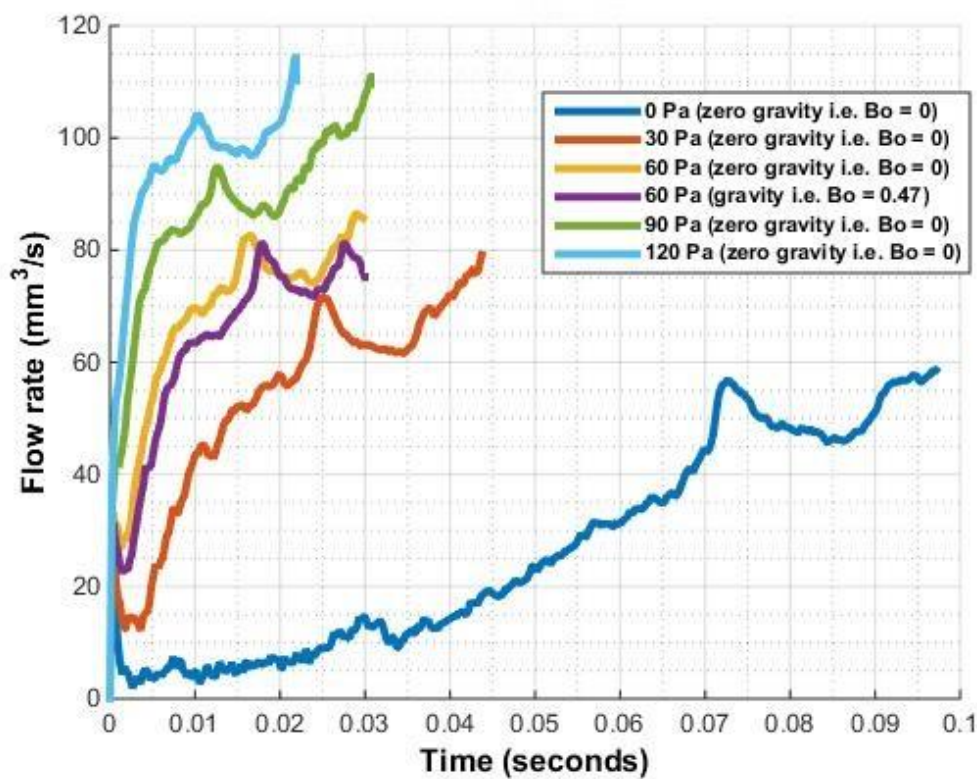


Figure 36. Comparison of flow rates for different pressure differences

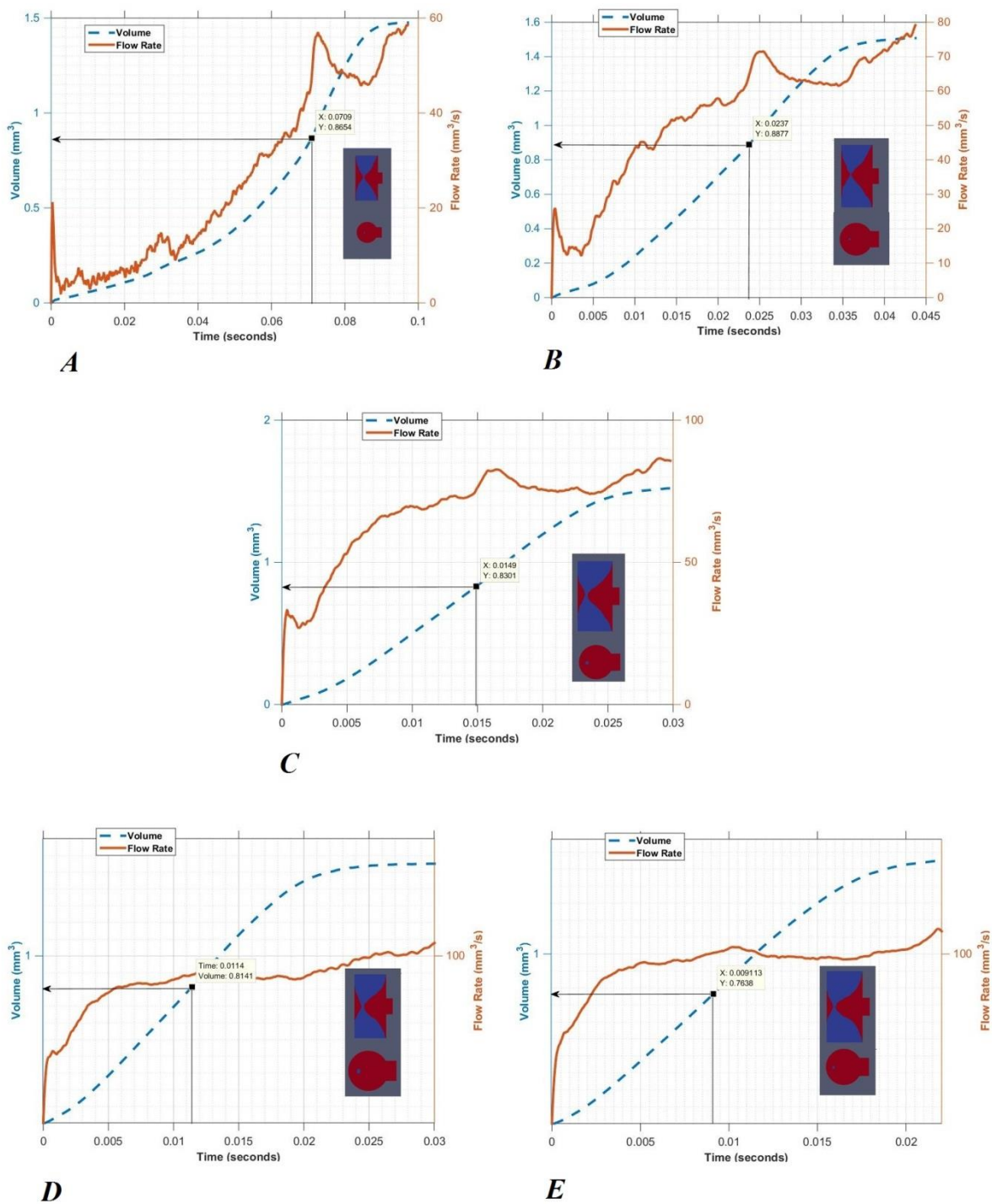


Figure 37. Plot of time-dependent flow rate and volume for different pressure differences indicating where plug is formed: A. 0 Pa; B. 30 Pa; C. 60 Pa; D. 90 Pa; and E. 120 Pa

Figure 37 shows where the plugs are formed in relation to the flow rate and volume. The formation of the annulus does not cause radical changes in flow rate, whereas the formation of the plug does. The process of plug formation is indicated by a jump in flow rate. The transition represents instability in the dynamic system and occurs so rapidly the volume in the cylinder is unaffected as suggested by the smoothness of the volume graph. Table 13 summarizes the transition process flow rate jump and duration.

Table 13

Summary of Flow rate jump and duration of annulus to plug transition

Pressure Difference (Pa)	Start		Peak		Δt (seconds)	$\Delta \dot{V}$ (mm^3/s)
	Time (seconds)	Flow rate (mm^3/s)	Time (seconds)	Flow rate (mm^3/s)		
0	0.0709	46.74	0.0727	56.98	0.0018	10.24
30	0.0237	64.4	0.02542	71.54	0.00172	7.14
60	0.0149	75.52	0.01657	82.62	0.00167	7.1
90	0.0114	88.71	0.01256	94.9	0.00116	6.19
120	0.0091	100.7	0.01019	104.1	0.00109	3.4

As table 13 shows, as the applied pressure difference increases, the duration of the transition process from annulus to plug is shorter. Furthermore, the flow rate jump reduces with increasing pressure difference. The energy used to convert annulus to plug comes from a combination of the applied pressure difference and the curvature.

When no pressure is applied at the inlet, the flow is entirely driven by and dependent on the curvature. Therefore, the change in curvature associated with the transition from annulus to plug causes a significant change in flow rate. However, an applied pressure at the inlet minimizes the contribution of the curvature to the flow rate. As the applied pressure difference increases a point is reached where the energy of the flow is predominantly derived from the applied pressure and less so from the curvature.

Hence, any interfacial topological change is less noticeable for higher applied pressure differences. Furthermore, the higher the applied pressure difference, the less pointed, more rounded and larger the effective curvature radius which implies less energy available at the interface to convert annulus to plug.

Figure 38 is the plots of the time-dependent volume for the different cases. The total volume of the circular cylinder is about 1.5mm^3 . The higher the applied pressure difference the sooner the container is completely filled. The volume increases non-linearly for the capillary driven case (i.e. 0 Pa pressure difference) while it increases more or less linearly for the cases where pressure difference is applied. This difference is an indication that the applied difference reduces the effect the curvature has on the flow as discussed under flow rate. It takes approximately 0.09 seconds for the container to be filled when no pressure is driving the flow and about 20% of that time for an applied pressure difference of 150 Pa.

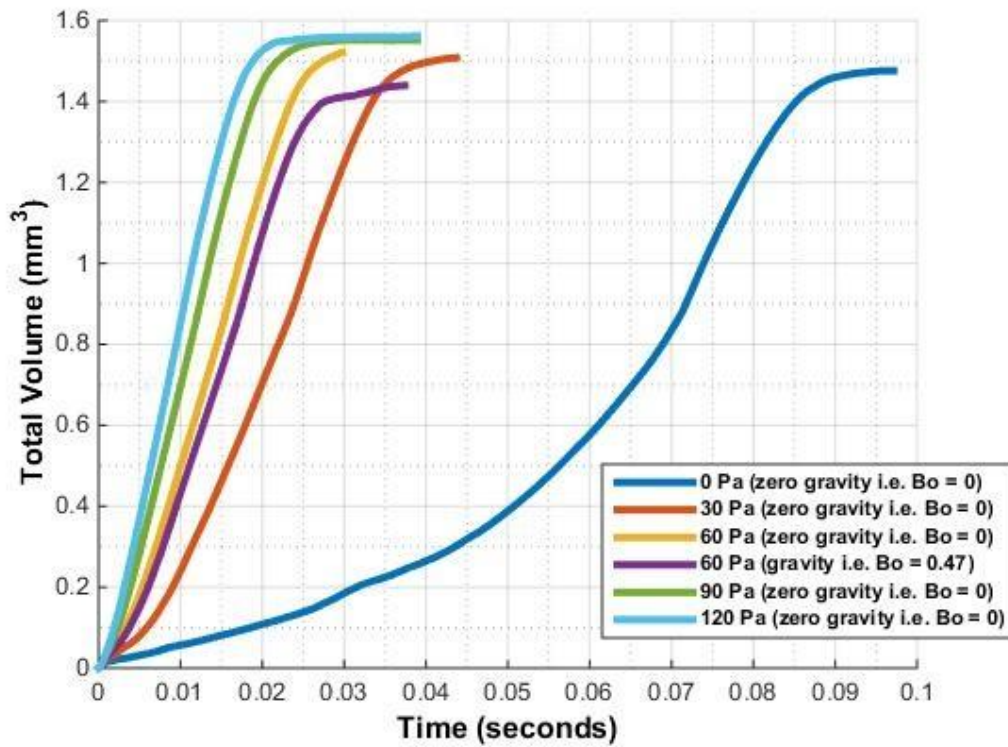


Figure 38. Comparison of time-dependent volume plot for different applied pressures.

A case with an applied pressure difference of 60 Pa for a bond number of 0.47 (similar to experiment) is presented to compare with the case with zero bond number. There is apparently a gradient difference in the plots for the 60 Pa case, however, the difference is not that significant. Figures 39 and 40, presents the volume and the flow rate plots for the same applied pressure. Under bond number 0.47, the process is slightly delayed. The presence of gravity only causes a delay in the flow rate profile.

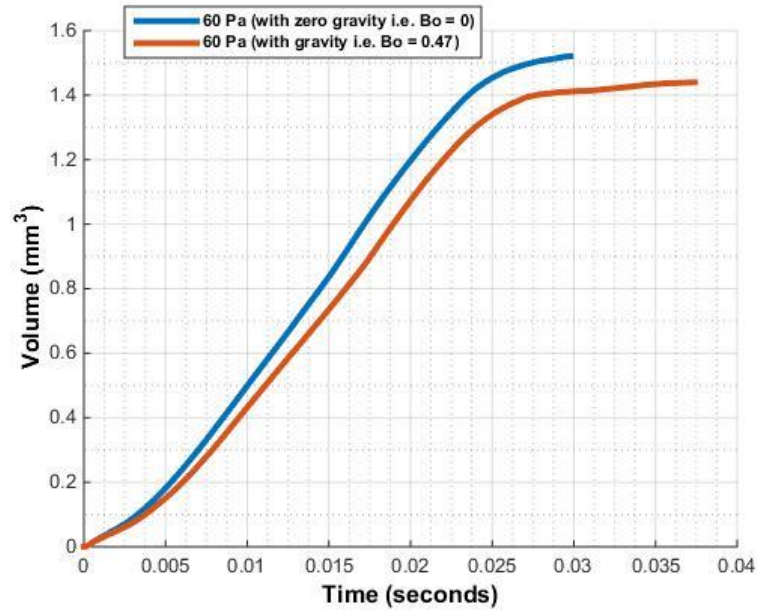


Figure 39. Volume versus Time for a pressure difference of 60 Pa for Bond number of 0.47 and 0 (i.e. $Bo = 0$ and $Bo = 0.47$)

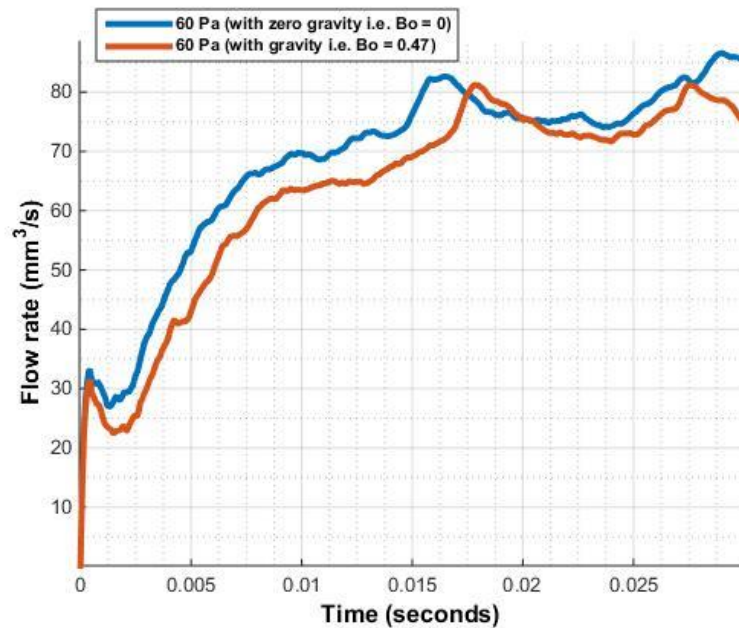


Figure 40. Flow rate versus time for a pressure difference of 60 Pa for a Bond number of 0 and 0.47. (i.e. $Bo = 0$ and $Bo = 0.47$)

. The radius of the main cylinder (0.0005 m) was used to non-dimensionalize the volume, and flow rate. The velocity used was the maximum inlet velocity at 0.001 seconds. Table 14 summarizes the velocities used.

Table 14

Maximum inlet velocities for non-dimensionalization

Pressure Difference (Pa)	Velocity (m/s)
0	0.092
30	0.262
60	0.410
90	0.497
120	0.592

The maximum flow rate occurs at approximately a dimensionless time of 13, where the plug is formed, regardless of applied pressure difference. The dimensionless time at which the plug is formed in experiment is 13.13 (figure 34). This confirms the existence of a characteristic plug time for this system.

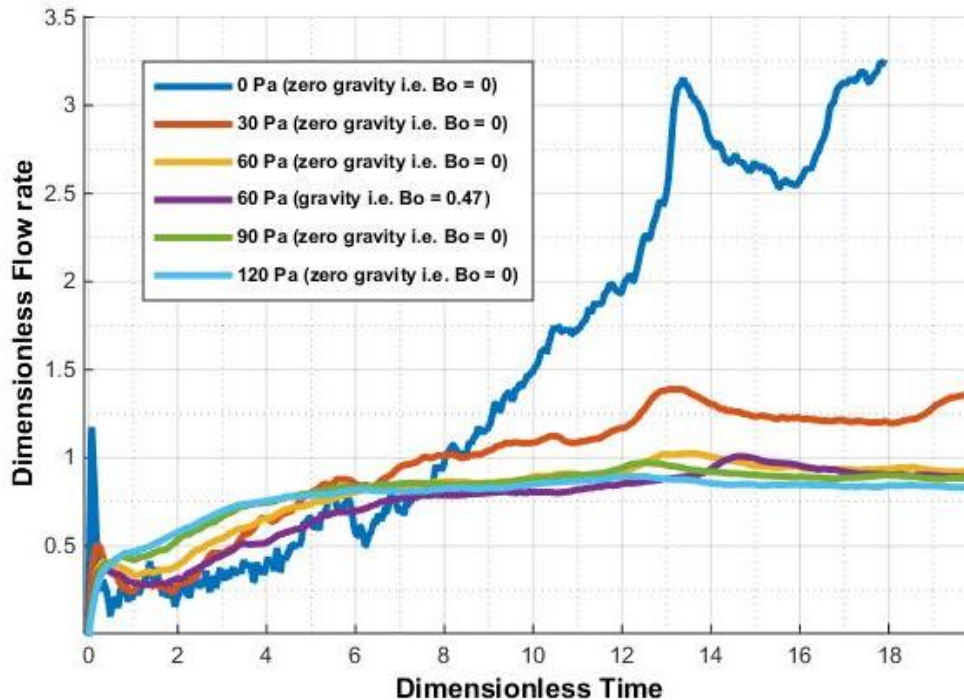


Figure 41. Dimensionless Flow Rate versus Dimensionless Time

Figure 41 also shows that the dimensionless flow rate peaks are lower for higher applied pressure differences. Above 60 Pa, the flow rate at the peak (plug formation) is equal to or less than that at the inlet at an earlier time (0.001 seconds). This suggests that the higher the applied pressure the less effect the plug formation has on the flow rate. The flow rate becomes independent of the interface curvature at higher applied pressure differences; hence, the energy required for transformation from annulus to plug is derived mostly from the applied pressure.

In figure 42, when the volume-versus-time plots for zero bond number are non-dimensionalized, they collapse on a line with a gradient of 0.78. The graph for a bond number of 0.47 has a gradient of approximately 0.59 compared to the experimental gradient of 0.58 (figure 23). This suggests that the system has a characteristic flow rate: 0.78 for Bond number = 0 (zero gravity); and 0.58 for Bond number = 0.47 (microgravity).

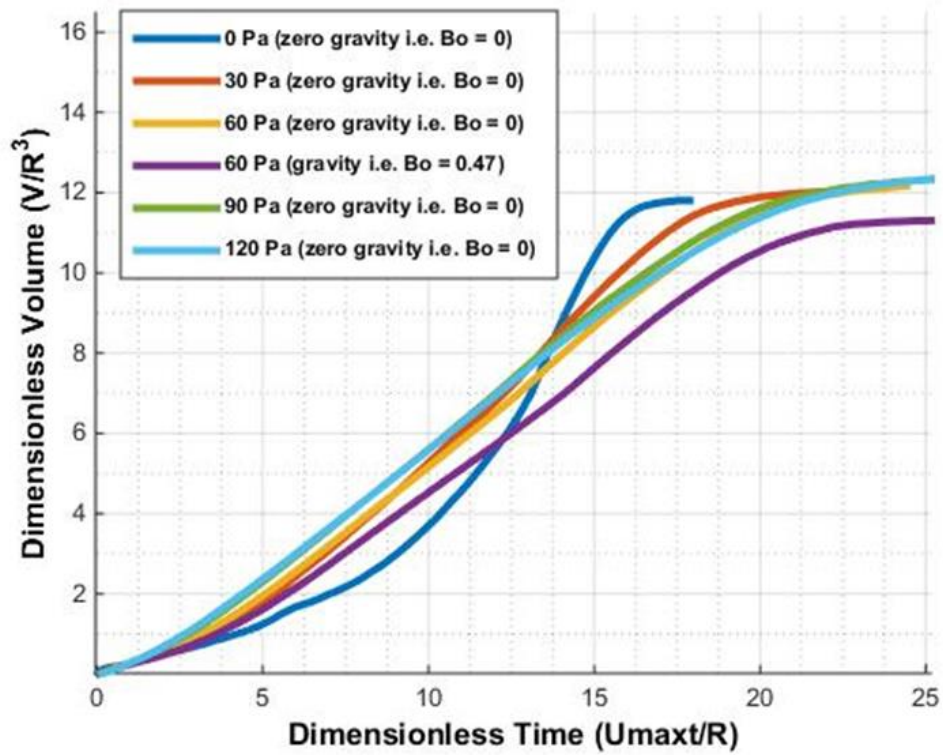


Figure 42. Non-dimensional volume versus non-dimensional time

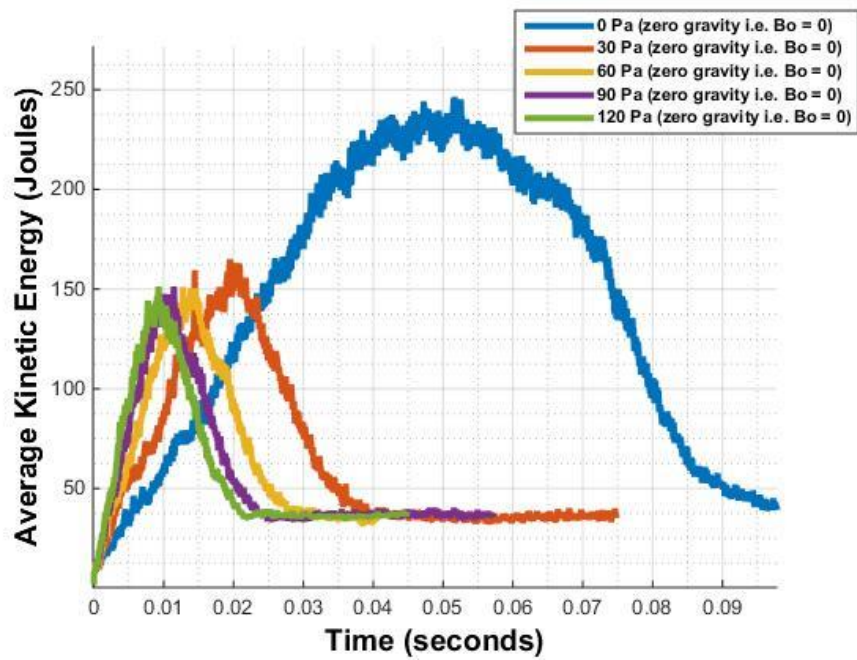


Figure 43. Plot of average system kinetic energy versus time

Figure 43 represents the average kinetic energy of the system at a given time. For all cases, the kinetic energy rises from zero until a peak is reached which coincides with the formation of the plug. The kinetic energy then drops to approximately 38 Joules for all cases. The kinetic energy rises and falls as the liquid fills the cylinder and interface shape changes. The acceleration caused from the formation of the annulus (transformation of curvature potential energy and applied pressure energy to kinetic energy) results in the peaks. However, for higher applied pressure differences the dynamics of the system becomes less dependent on the curvature properties as in the case for flow rate. This results in lower peak values for higher applied pressure differences.

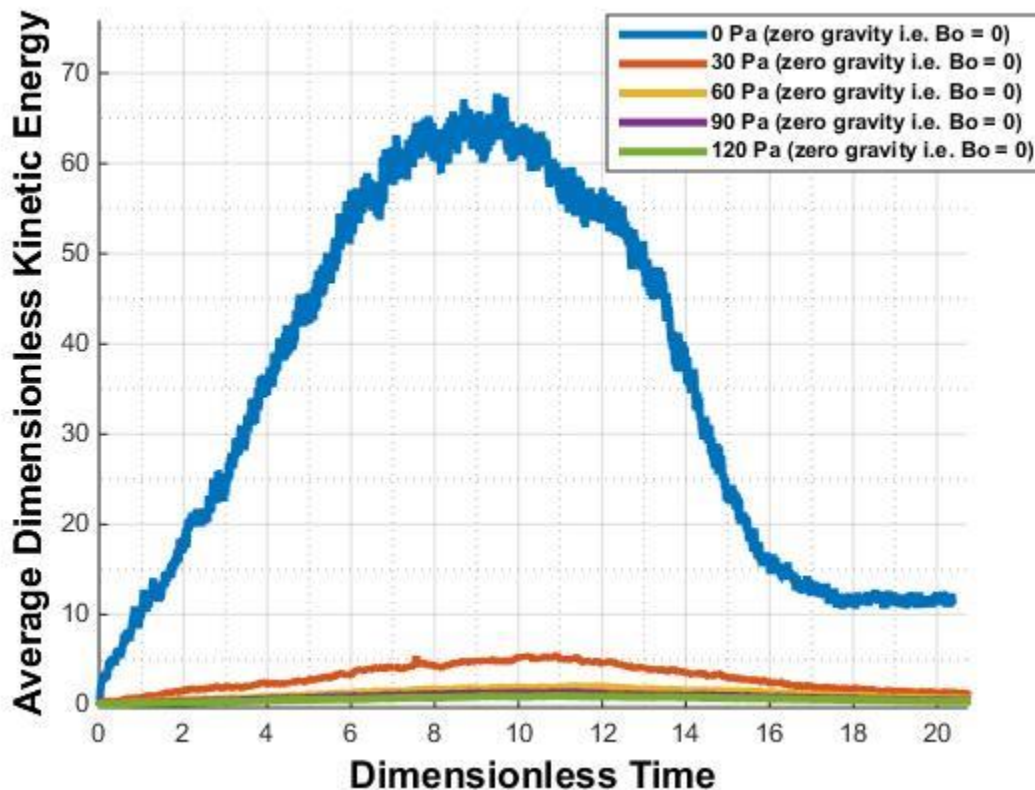


Figure 44. Plot of non-dimensional system kinetic energy versus time

Figure 44 is the result of non-dimensionalizing figure 40. Figure 41 illustrates the significance of the curvature potential and the effect of applied pressure on the overall kinetic

energy of the system. The kinetic energy for 0 Pa, is higher than all other cases. The highest kinetic energies coincide with the formation of the annulus which has a characteristic time of approximately 9 for the 0 Pa case. The higher kinetic energy levels in this case is an indication of higher interfacial surface energy levels available

Given that the stable volume solutions for the plug in a static system is only a function of volume and contact angle [1], it is interesting to note that applied pressure difference has an effect on the plug solution in the dynamic system. The plug solution exhibits a negative linear correlation with pressure difference according to the expression $V_{plug}^* = 8.3 - 0.011 \Delta P$, where V_{plug}^* is the plug volume and ΔP is the applied pressure difference (figure 42).

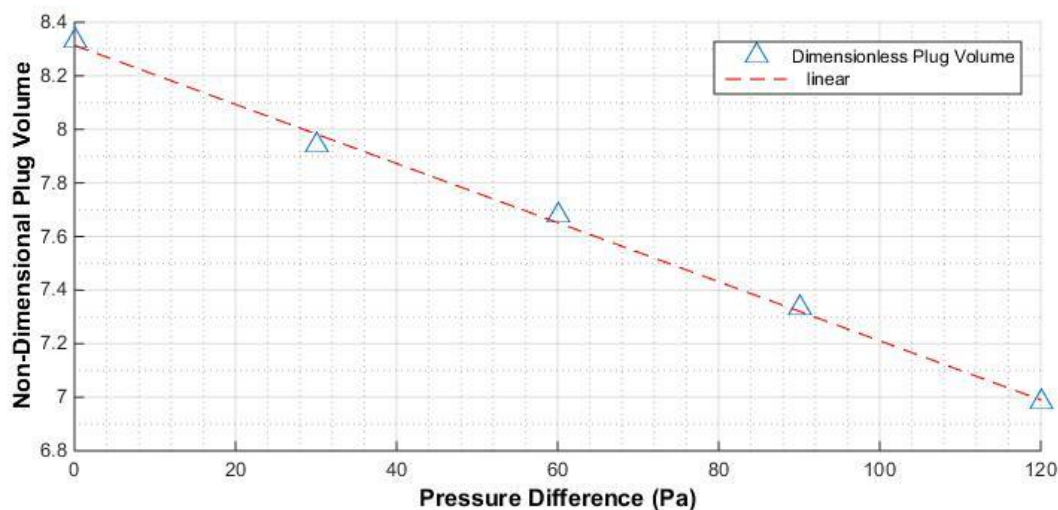


Figure 45. Relationship between Plug solution and applied Pressure Difference

Figure 45 is a plot of dimensionless time versus pressure difference. The pressures are non-dimensionlized using σ/R . Here, σ is surface tension and R is the main cylinder radius.

The plug non-dimensional time is clearly not a function of the applied pressure difference and the plot suggests a plug characteristic time of an approximate value of 13.1 exists.

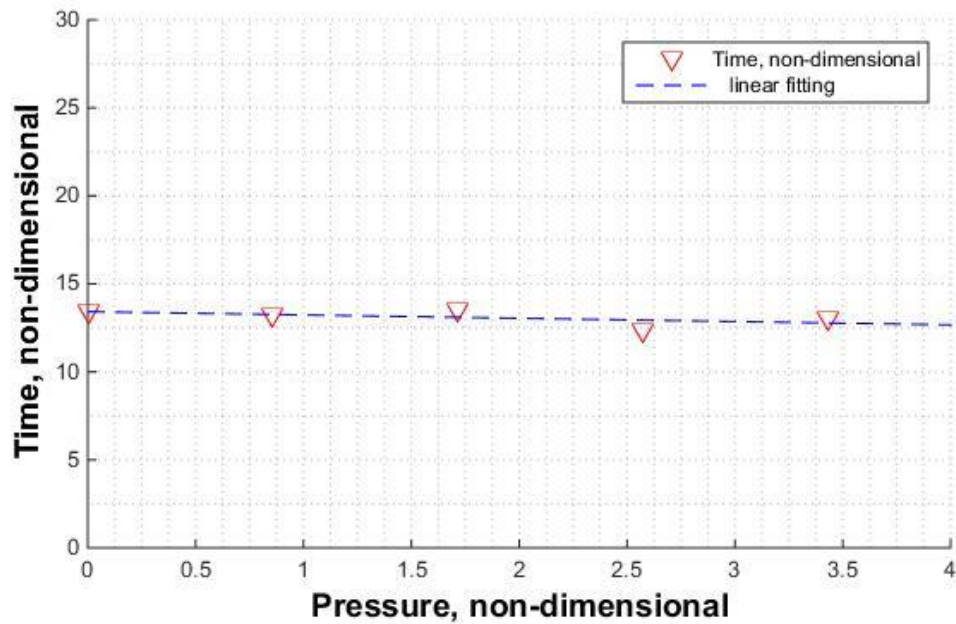


Figure 46. Plot of plug non-dimensional time versus pressure difference showing the existence of a plug characteristic time

The plug is formed after a non-dimensional time of approximately 13 for all applied pressures. Above this time, all plug solutions are stable. This non-dimensional characteristic time implies the predictability of plug formation in the dynamic system.

4.2.3 Surface Evolver Results

Figures 47 through 53 show the stable shapes for dimensionless volumes 2 through 5 for a contact angle of 10° . The resultant static equilibrium shape is only a function of volume. The static plug solution exists for dimensionless volumes of 4.7 and above.

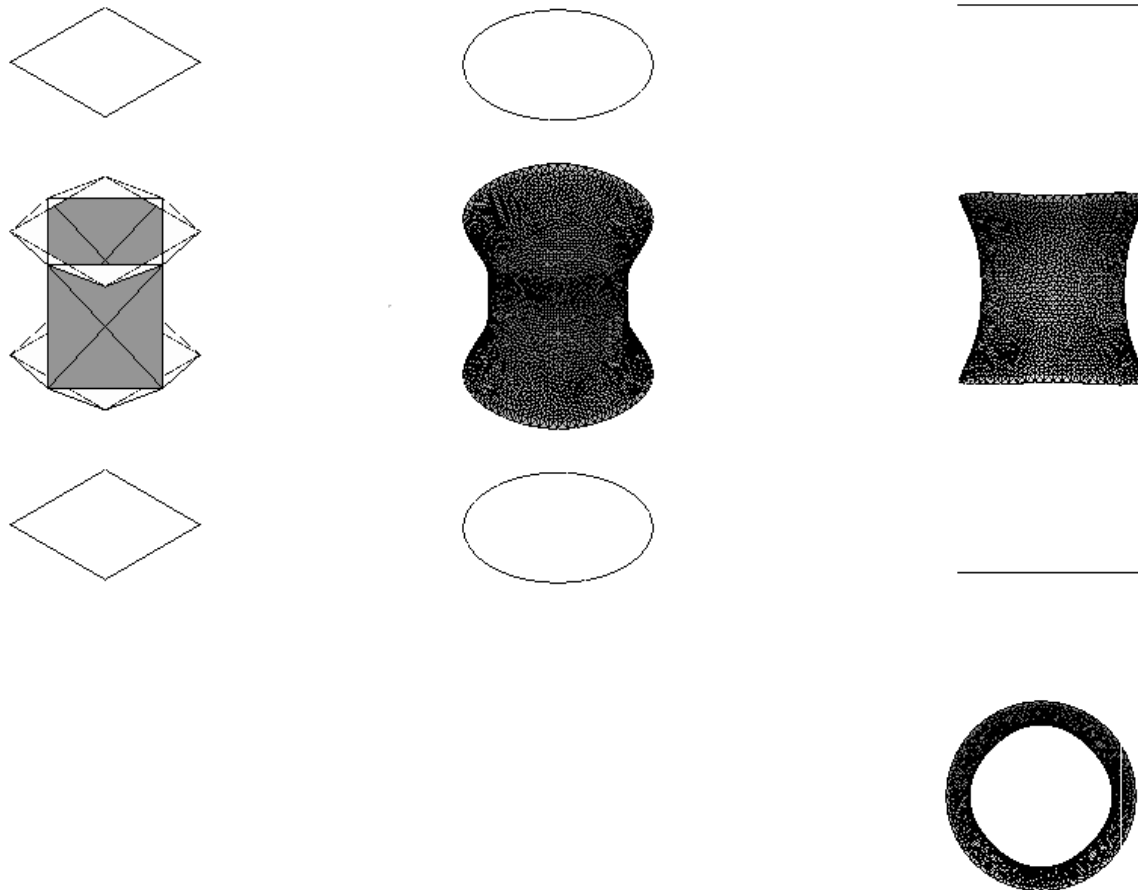


Figure 47. Annulus solution for a non-dimensional volume of 2

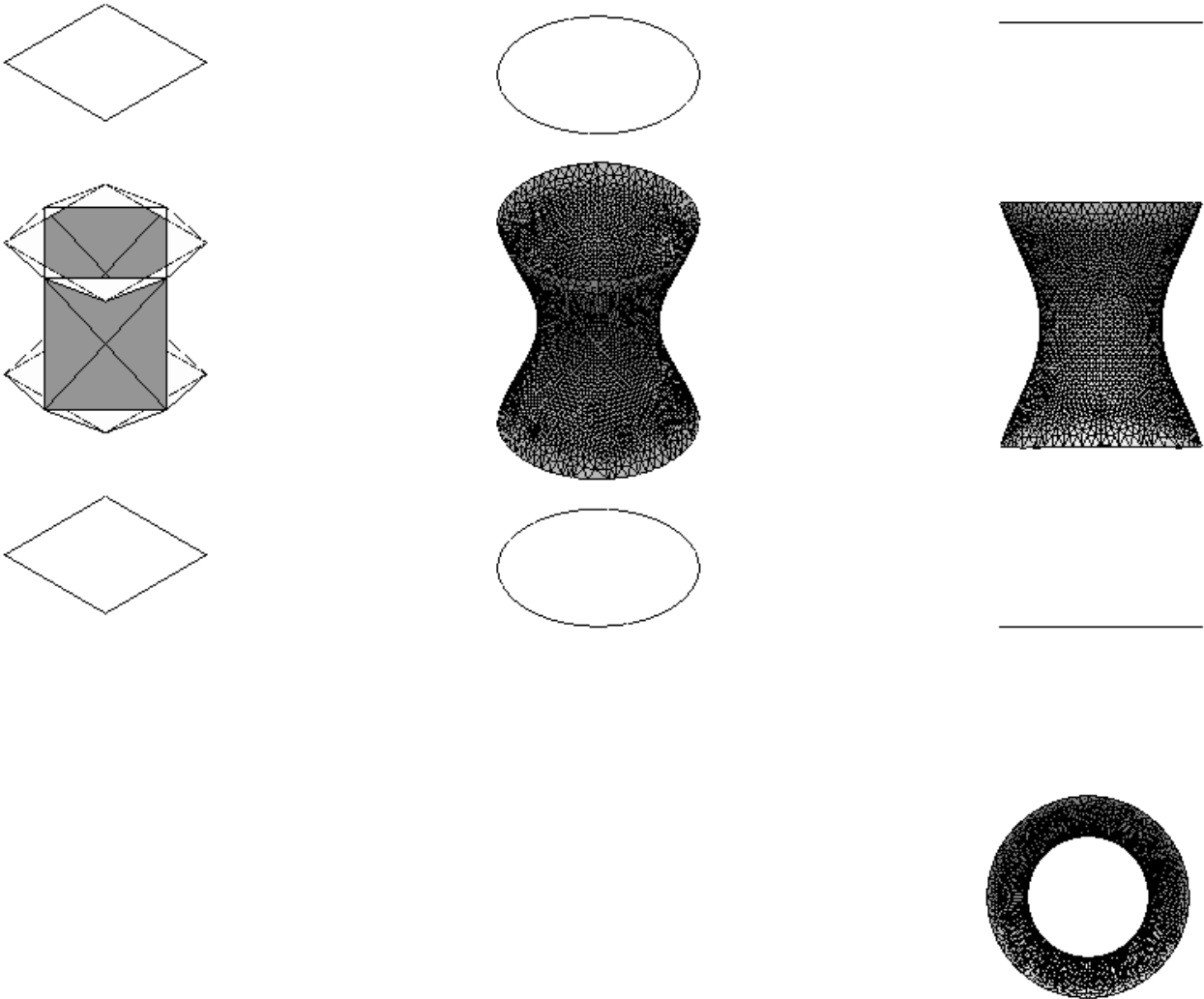


Figure 48. Annulus solution for a non-dimensional volume of 3

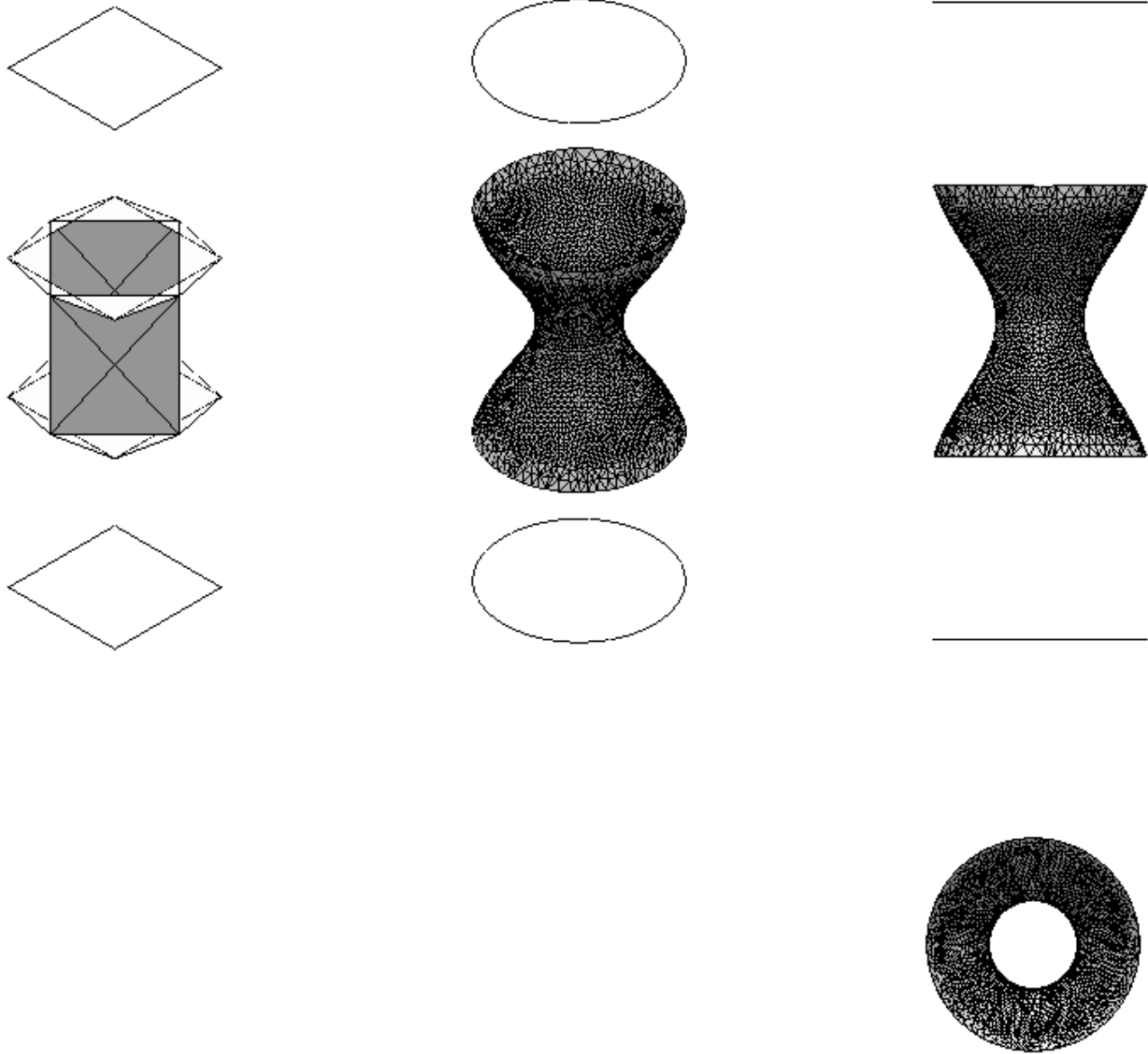


Figure 49. Annulus solution for a non-dimensional volume of 4

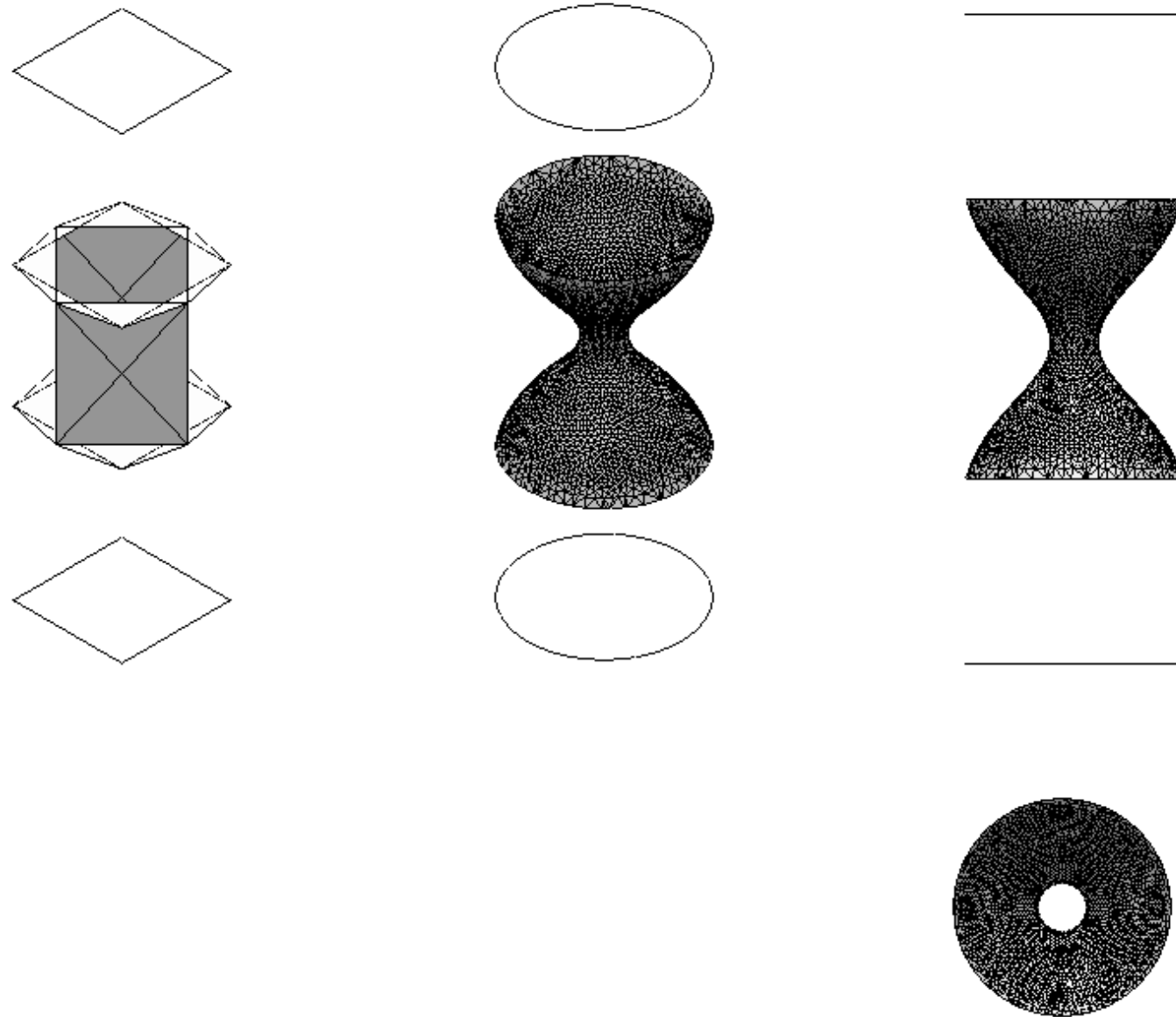


Figure 50. Minimum annular solution for non-dimensional volume of 4.5

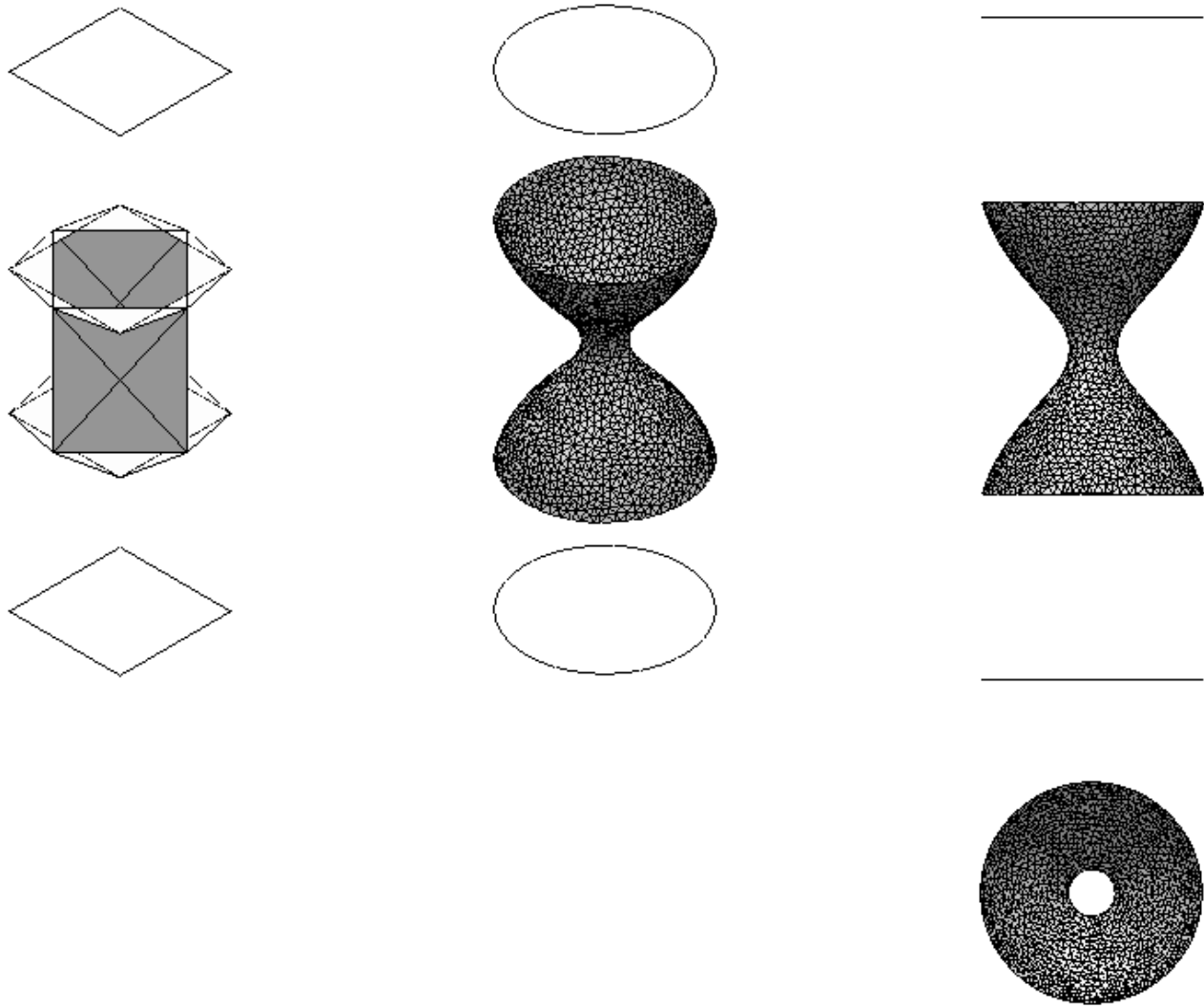


Figure 51. Minimum annular solution for non-dimensional volume of 4.6

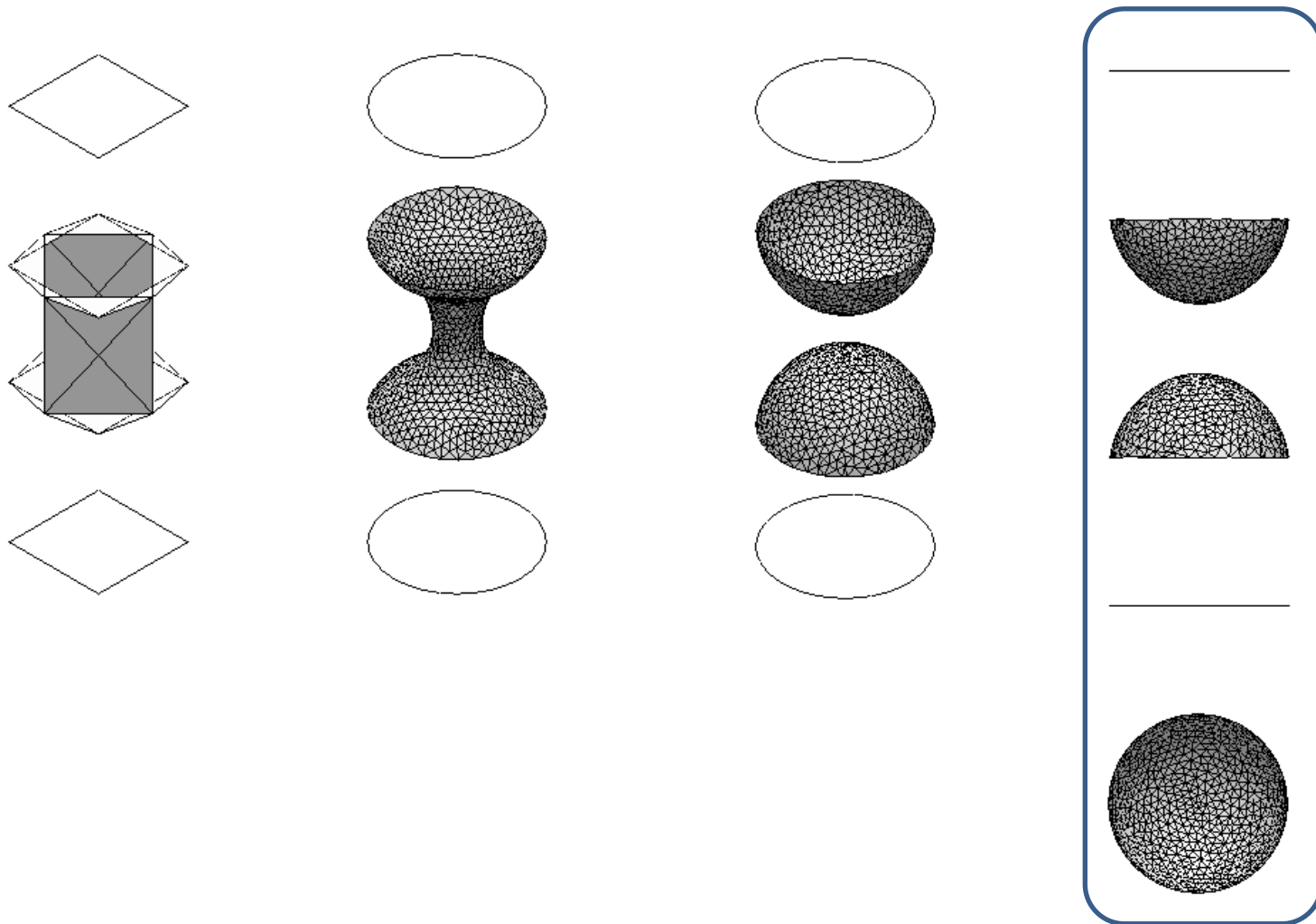


Figure 52. Minimum plug solution for a non-dimensional volume of 4.7

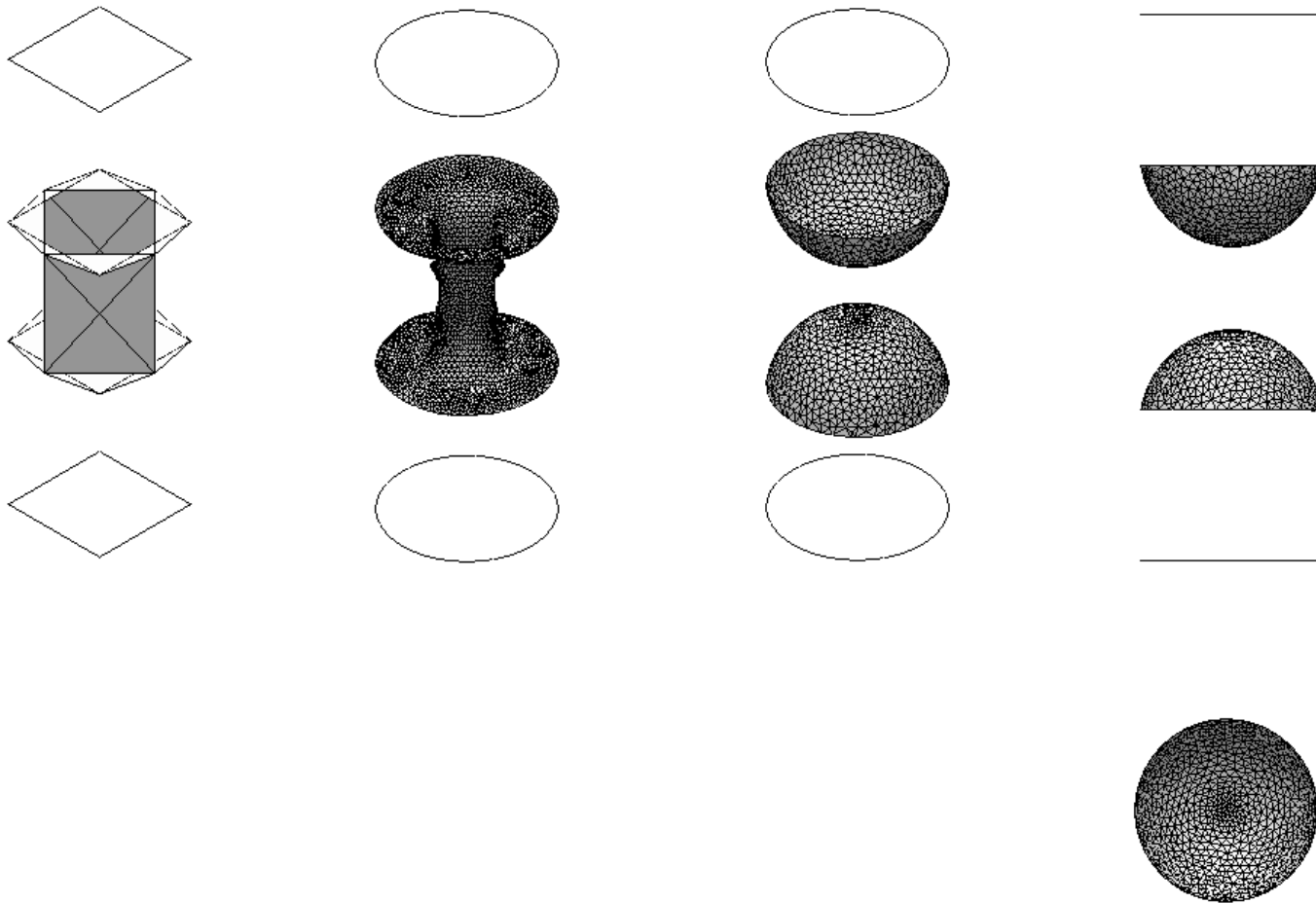


Figure 53. Minimum plug solution for a non-dimensional volume of 5

The plug is formed at a non-dimensional volume of 4.7 for a static liquid forming a contact angle of 10° with the walls of a circular cylinder of an aspect ratio of 1.0. For all volumes above 4.7, the stable solution is a plug. This result validates results by Collicott et al. [1].

4.2.4 Comparison of Static and Dynamics Solutions

Statics: According to surface evolver computations, under static conditions and for a contact angle of 10° , the plug is the stable solution for a non-dimensional volume of 4.7. Using OpenFOAM, the stable topology in a static system was computed for a non-dimensional volume of 4.7 (figure 54).

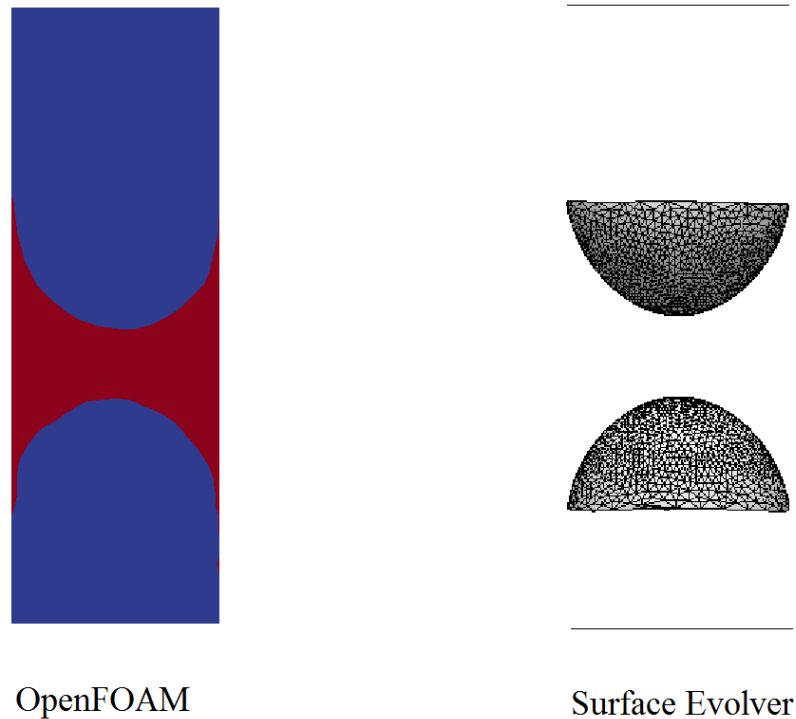


Figure 54. Comparison of OpenFOAM and Surface Evolver solutions for non-dimensional volume of 4.7. OpenFOAM result is a cross section along the axis of the cylinder. The liquid is

designated the color red and air is assigned the color blue. Surface Evolver result is a side view of interfaces of the stable plug solution.

Figure 55 is a plot of the free-surface interfacial position for OpenFOAM and Surface Evolver results for a non-dimensional volume of 4.7. The results show that OpenFOAM and Surface Evolver are in very close agreement.

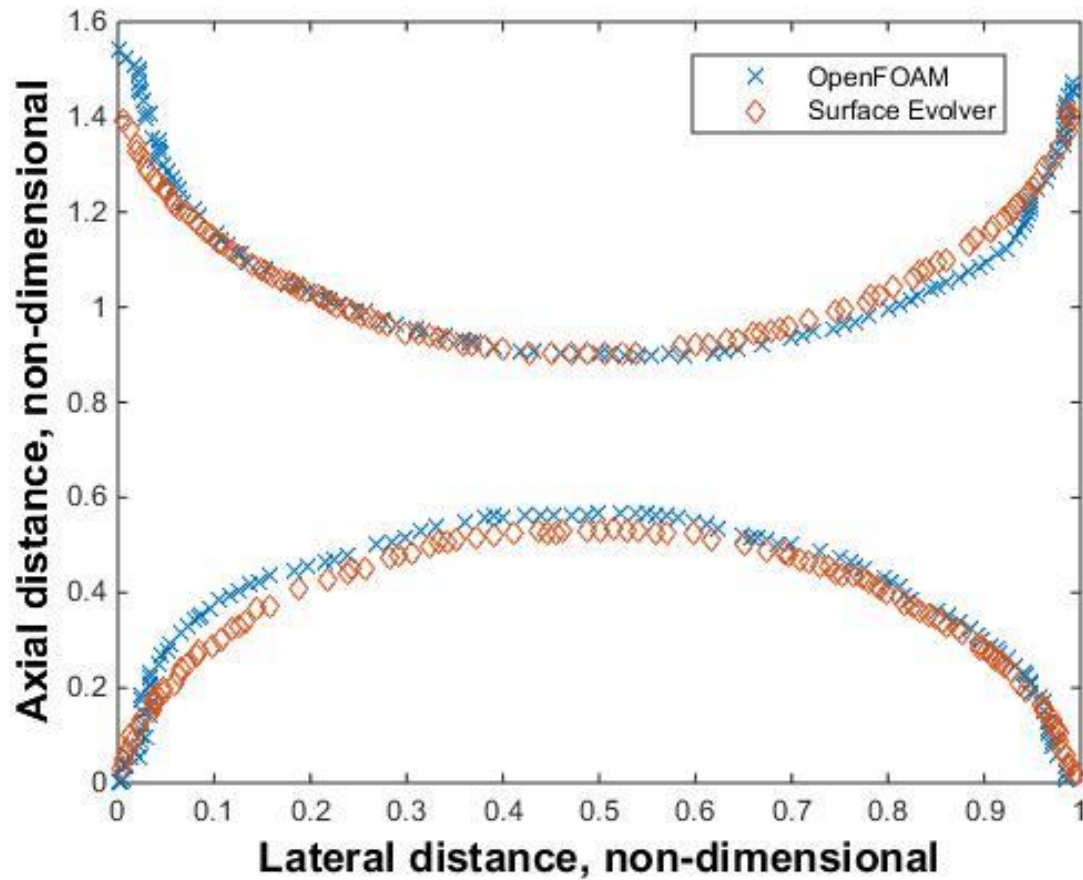


Figure 55. Plot of interfacial position using OpenFOAM and Surface Evolver for a non-dimensional volume of 4.7 and contact angle of 10° . The plot is non-dimensionalized using the cylinder diameter.

Dynamics: To understand the significance of dynamics topological solutions, stable static solutions are compared with dynamics solutions. The computed stable plug solution for a circular cylinder (not laterally compressed) is 4.7. In figure 56, the static plug solutions in a cylinder of different compression ratios (Aspect Ratio (AR)) – 1.1, 1.5, 3 and 5 - based on previous study by Jaron[10] is compared with the stable plug solution (stable plug boundary) of the dynamic system in this study.

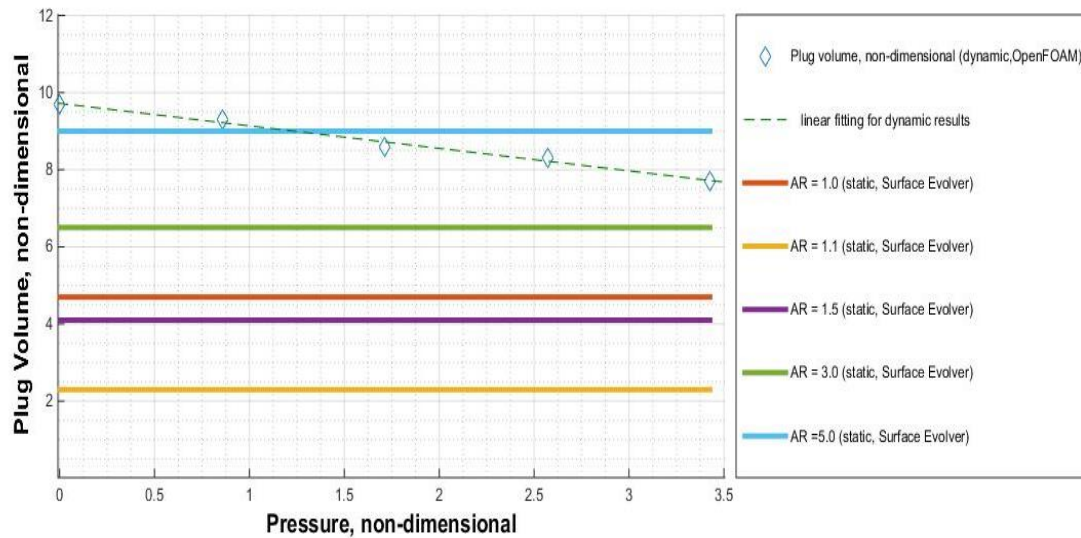


Figure 56. Comparison of stable static and dynamic solutions

Plug formation is delayed for higher aspect ratios in the static system. The stable dynamic solutions are that of a circular cylinder of aspect ratio 1.0. Compared to the static system, the dynamic system has higher plug solutions for the same aspect ratio (i.e. AR = 1.0). This implies that in the dynamic system, the plug is delayed which is a favorable outcome.

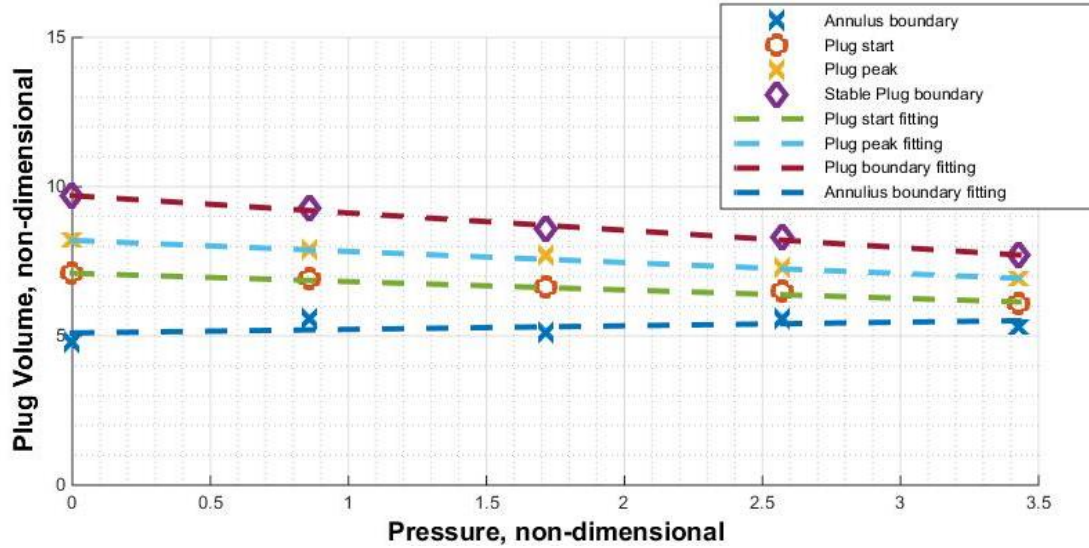


Figure 57. Comparison of dynamic solutions for annulus and plug showing transition regimes

Figure 57 compares the solutions of annulus and plug shapes. The annulus solution exists between the annulus boundary line and the plug start line. Between the plug start line and the stable plug boundary, the interface is unstable and transitioning from annulus to plug. Above the plug boundary line, the plug is stable. The transition regime bounded by the plug start line and plug boundary line gets narrower as pressure is increased. At high applied pressure differences, the plug occurs earlier than at lower pressure differences.

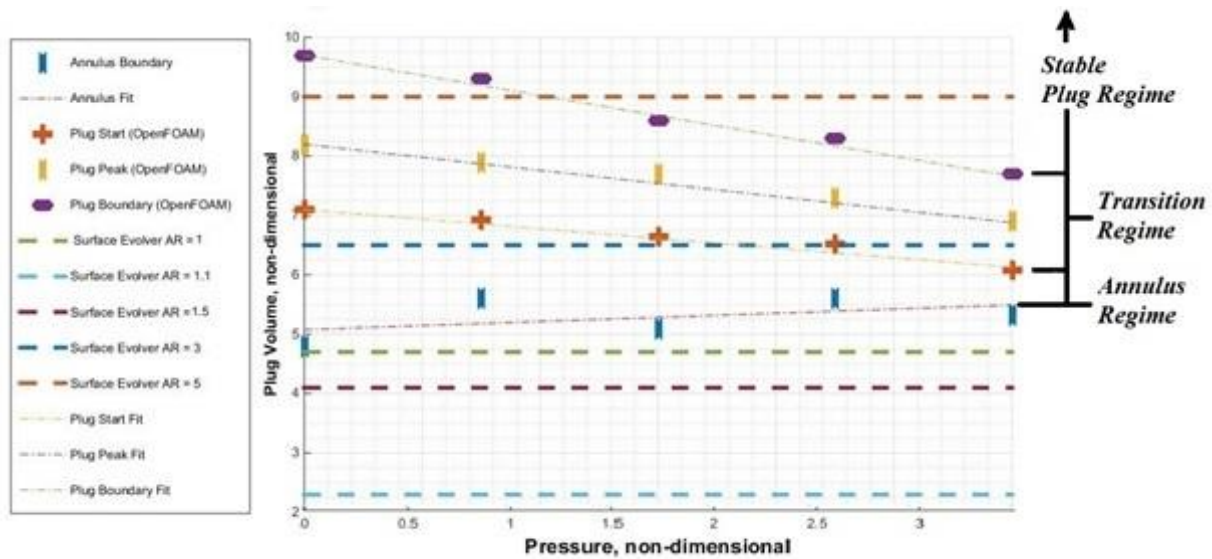


Figure 58. Comparison of OpenFOAM results with Surface Evolver plug solutions for circular cylinders with varying aspect ratios (AR) (from literature[1, 10]) for 10° contact angle.

The figure 58 compares the plug solutions of OpenFOAM with the minimum energy plug solutions in surface evolver. Regions of transition (or instability) and stability exist. Dynamic solutions are higher than static solutions for an aspect ratio of 1.0.

High applied pressure differences correspond to high injection flow rates and vice versa. At a pressure of 0, the plug is formed and stable at and above a non-dimensional volume of approximately 9.8 for the dynamic system. For 120 Pa, the plug is stable above 7.8. In the static system, the stable plug solution is 4.7. In the dynamic system, plug formation is delayed compared with the static system. Slower liquid injection rates have higher plug solutions compared with faster injection rates.

CHAPTER 5

Discussion and Future Research

Minimum energy solutions or static equilibrium solutions in zero-gravity are important in many fields. Surface Evolver has been used to compute energies, pressures, existence and stability of various topologies for a range of contact angles and volumes. Results of such studies have been presented in the form of a stability solution maps indicating regimes where the different topologies are dominant.

Static equilibrium studies were initially carried out in a circular pipe. Results of this research demonstrated the usefulness and efficiency of Surface Evolver for the analysis of three-dimensional axisymmetric and non-axisymmetric topologies. Results from this study formed the baseline for research in this field. Further studies were conducted in different tube configurations such as in a laterally compressed cylinder. Results indicated an increase in the minimum stable plug solution for highly compressed tubes which meant a delay in plug formation. The implication was that compression in tubes would reduce gas occlusions in liquid filled channels and avoid or delay plug formation in gas filled tubes.

In Surface Evolver studies only static stability of fluids was investigated. A useful improvement to the knowledge base would be a dynamic study of the two-phase fluid flow in a circular cylinder under reduced gravity conditions. In this thesis, an experiment was conducted to study the evolution of silicone oil interface in a circular tube injected via a side channel. A high speed camera was used to capture the fluid at different times. OpenFOAM, a CFD tool, was also utilized to simulate the flow for different flow rates by varying applied boundary pressure. Surface Evolver was also employed to compute the minimum energy topology for different volumes to be compared with experiment and OpenFOAM results.

Experiment and simulation results confirmed the existence of droplet, annulus and plug topologies. Surface Evolver results for plug and annulus solutions were axisymmetric; however, OpenFOAM suggests the overwhelming existence of non-symmetrical annulus and plug solutions. Furthermore, an instability regime between the annulus and plug solutions was found which depended on the applied pressure difference. Higher applied pressures resulted in narrower instability regions. Stable Plug volume solutions also depended on applied pressure difference (and in turn the inlet flow rate). Slower injection rates delayed plug formation. In addition to the instability and stability regimes, a stable annulus regime was present which gets narrower as applied pressure difference increases.

The transition regime from annulus to plug was studied in terms of kinetic energy and time-dependent inlet flow rate. The transition regions corresponded to jumps in flow rate and kinetic energy. It was found that high applied pressure differences reduces the effect of interface energy and results in smoother energy curves. The transition from droplet to annulus resulted in negligible changes to the kinetic energy and flow rate curves.

Moreover, a characteristic non-dimensional time of approximately 13 was found which corresponds to plug formation. At this time, the cylinder is completely blocked for all applied pressures and flow rates. Thus the characteristic time found was independent of applied pressure difference and flow rate. The significance of this characteristic time is that it defines the dynamic system and allows the plug to be predicted.

Furthermore, plug solutions for the dynamic system are almost two folds those of the static system. This implies delayed plug formation in dynamic systems compared with static systems.

A major advancement of this study would be analyzing the effect of different configurations such as lateral tube compression and tube bending on flow quantities such as kinetic energy and flow rate. Further investigation on characteristic non-dimensional time is also warranted. It would be very useful to understand the effect of different tube dimensions, contact angles and configurations on the characteristic time. It makes sense to generate a solution map, if possible.

References

1. Collicott, S.H., W.G. Lindsley, and D.G. Frazer, *Zero-gravity liquid-vapor interfaces in circular cylinders*. *Physics of Fluids* (1994-present), 2006. **18**(8): p. 087109.
2. Collicott, S.H. and M.M. Weislogel, *Computing existence and stability of capillary surfaces using Surface Evolver*. *AIAA journal*, 2004. **42**(2): p. 289-295.
3. Myshkis, A., et al., *Low-gravity fluid mechanics*. Translated from the Russian by Wadhwa, RS, XIX, 583 pp. 218 figs.. Springer-Verlag Berlin Heidelberg New York, 1987. **1**.
4. Finn, R., *Equilibrium capillary surfaces*. 1986: Springer.
5. Finn, R., *Capillary surface interfaces*. *Notices of the AMS*, 1999. **46**(7): p. 770-781.
6. Colosqui, C.E., et al., *Droplet and slug formation in polymer electrolyte membrane fuel cell flow channels: The role of interfacial forces*. *Journal of Power Sources*, 2011. **196**(23): p. 10057-10068.
7. Chen, Y., et al. *Introducing SE-FIT: surface evolver–fluid interface tool for studying capillary surfaces*. in *Proc. 49th AIAA Aerospace Sciences Meeting*. 2011.
8. Brakke, K., *Surface Evolver, Mathematics Department, Susquehanna University, Selinsgrove, PA*, 2003.
9. Slobozhanin, L.A., J.I.D. Alexander, and A.I. Fedoseyev, *Shape and stability of doubly connected axisymmetric free surfaces in a cylindrical container*. *Physics of Fluids* (1994-present), 1999. **11**(12): p. 3668-3677.
10. Jaron, J.M. and S.H. Collicott, *Two-phase Static Capillary Phenomena in Flattened Tubes*. 46th AIAA Aerospace Sciences Meeting and Exhibit, Reno, Nevada, Jan. 7-10, 2008. AIAA-2008-0826, 2008.

11. Heil, M., *Minimal liquid bridges in non-axisymmetrically buckled elastic tubes*. Journal of Fluid Mechanics, 1999. **380**: p. 309-337.
12. Heil, M., *Airway closure: Occluding liquid bridges in strongly buckled elastic tubes*. Journal of biomechanical engineering, 1999. **121**(5): p. 487-493.
13. Brakke, K.A., *The surface evolver*. Experimental mathematics, 1992. **1**(2): p. 141-165.
14. Gerlach, D., et al., *Comparison of volume-of-fluid methods for surface tension-dominant two-phase flows*. International Journal of Heat and Mass Transfer, 2006. **49**(3): p. 740-754.
15. Osher, S., *Level set methods*, in *Geometric Level Set Methods in Imaging, Vision, and Graphics*. 2003, Springer. p. 3-20.
16. Sussman, M. and E.G. Puckett, *A coupled level set and volume-of-fluid method for computing 3D and axisymmetric incompressible two-phase flows*. Journal of Computational Physics, 2000. **162**(2): p. 301-337.
17. Osher, S. and R.P. Fedkiw, *Level set methods: an overview and some recent results*. Journal of Computational physics, 2001. **169**(2): p. 463-502.
18. Sussman, M., et al., *An improved level set method for incompressible two-phase flows*. Computers & Fluids, 1998. **27**(5): p. 663-680.
19. Noh, W.F. and P. Woodward. *SLIC (simple line interface calculation)*. in *Proceedings of the Fifth International Conference on Numerical Methods in Fluid Dynamics June 28–July 2, 1976 Twente University, Enschede*. 1976. Springer.
20. Youngs, D.L., *Time-dependent multi-material flow with large fluid distortion*. Numerical methods for fluid dynamics, 1982. **24**: p. 273-285.

21. Puckett, E.G., et al., *A high-order projection method for tracking fluid interfaces in variable density incompressible flows*. Journal of Computational Physics, 1997. **130**(2): p. 269-282.
22. Welch, S.W. and T. Rachidi, *Numerical computation of film boiling including conjugate heat transfer*. Numerical Heat Transfer: Part B: Fundamentals, 2002. **42**(1): p. 35-53.
23. Lafaurie, B., et al., *Modelling merging and fragmentation in multiphase flows with SURFER*. Journal of Computational Physics, 1994. **113**(1): p. 134-147.
24. Renardy, Y. and M. Renardy, *PROST: a parabolic reconstruction of surface tension for the volume-of-fluid method*. Journal of Computational Physics, 2002. **183**(2): p. 400-421.
25. Son, G., *Efficient implementation of a coupled level-set and volume-of-fluid method for three-dimensional incompressible two-phase flows*. Numerical Heat Transfer: Part B: Fundamentals, 2003. **43**(6): p. 549-565.
26. Prosperetti, A., *Motion of two superposed viscous fluids*. Physics of Fluids (1958-1988), 1981. **24**(7): p. 1217-1223.
27. Van Wachem, B. and J. Schouten, *Experimental validation of 3-D lagrangian VOF model: Bubble shape and rise velocity*. AIChE journal, 2002. **48**(12): p. 2744-2753.
28. van Sint Annaland, M., N. Deen, and J. Kuipers, *Numerical simulation of gas bubbles behaviour using a three-dimensional volume of fluid method*. Chemical Engineering Science, 2005. **60**(11): p. 2999-3011.
29. Gopala, V.R. and B.G. van Wachem, *Volume of fluid methods for immiscible-fluid and free-surface flows*. Chemical Engineering Journal, 2008. **141**(1): p. 204-221.
30. Chen, L. and Y. Li, *A numerical method for two-phase flows with an interface*. Environmental modelling & software, 1998. **13**(3): p. 247-255.

31. Jeon, S.-S., S.-J. Kim, and G.-C. Park, *CFD simulation of condensing vapor bubble using VOF model*. World Acad. Sci., Eng. Technol, 2009. **60**: p. 209-215.
32. Hirt, C.W. and B.D. Nichols, *Volume of fluid (VOF) method for the dynamics of free boundaries*. Journal of computational physics, 1981. **39**(1): p. 201-225.
33. Sallam, K., C. Aalburg, and G. Faeth, *Breakup of round nonturbulent liquid jets in gaseous crossflow*. AIAA journal, 2004. **42**(12): p. 2529-2540.
34. OpenCFD, O., *The Open Source CFD Toolbox*. User Guide, OpenCFD Ltd, 2009.
35. OpenCFD, L., *OpenFOAM: The Open Source Computational Fluid Dynamics Toolbox*, 2011.
36. Jasak, H., A. Jemcov, and Z. Tukovic, *OpenFOAM: A C++ library for complex physics simulations*. 2013.
37. Weislogel, M.M. and S.H. Collicott, *Capillary rewetting of vaned containers: Spacecraft tank rewetting following thrust resettling*. AIAA journal, 2004. **42**(12): p. 2551-2561.
38. Lindsley, W.G., et al., *Asymmetric and axisymmetric constant curvature liquid-gas interfaces in pulmonary airways*. Annals of biomedical engineering, 2005. **33**(3): p. 365-375.
39. Chen, Y. and S.H. Collicott, *Study of wetting in an asymmetrical vane-wall gap in propellant tanks*. AIAA journal, 2006. **44**(4): p. 859-867.
40. Phelan, R., D. Weaire, and K. Brakke, *Computation of equilibrium foam structures using the Surface Evolver*. Experimental Mathematics, 1995. **4**(3): p. 181-192.
41. MORETTO, H., M. Schulze, and G. Wagner, *Silicones in Ullmann's Encyclopedia of Industrial Chemistry, editors Elvers, B., et al*, 1993, VCH.

42. Ashby, M.F., *Materials selection in mechanical design*. MRS BULLETIN, 2005. **30**: p. 995.
43. Abràmoff, M.D., P.J. Magalhães, and S.J. Ram, *Image processing with ImageJ*. Biophotonics international, 2004. **11**(7): p. 36-43.